



UNIVERSITY OF NAPLES FEDERICO II

Department of Materials and Production Engineering

PhD Thesis in

Innovative Technologies for Materials, Sensors and Imaging

21st cycle

**SOL-GEL SYNTHESIS OF FUNCTIONAL NANOCOMPOSITES
BASED ON INORGANIC OXIDES**

Elisa Marena

November 2008

UNIVERSITY OF NAPLES FEDERICO II

Department of Materials and Production Engineering

PhD Thesis in

Innovative Technologies for Materials, Sensors and Imaging

21st cycle

SOL-GEL SYNTHESIS OF FUNCTIONAL NANOCOMPOSITES

BASED ON INORGANIC OXIDES

Tutors: **Prof. Antonio Aronne**

PhD student: **Elisa Marennna**

Dr. Carmela Aruta

November 2008

CONTENTS

Acknowledgements 9

INTRODUCTION 11

PUBLICATIONS 22

CHAPTER 1

Sol-gel Technology 27

1 Sol-gel chemistry 29

1.1 The role of the precursors 29

1.2 Gelation: hydrolysis and polycondensation 29

1.3 Transformations of the gel 32

2 Dip coating technique 33

CHAPTER 2

The Nb₂O₅·SiO₂ binary system: Experimental 38

1 Synthesis 38

2 Chemical analysis 41

3 Thermal analysis 43

4 Structural analysis 44

4.1 X-Ray Diffraction 44

4.2 Raman spectroscopy 44

4.3 Fourier Transform Infrared spectroscopy 44

5 Textural analysis 45

5.1 N₂ adsorption 45

5.2 Ammonia Temperature Programmed Desorption and Fourier Transform Infrared spectroscopy with probe molecules	46
6 Catalytic tests	48

CHAPTER 3

The $\text{Li}_2\text{O}\cdot\text{Nb}_2\text{O}_5\cdot\text{SiO}_2$ ternary system: Experimental 50

1 Synthesis	50
1.1 Bulk and flakes	51
1.2 Thin films	53
2 Bulk and flakes characterization	56
2.1 Thermal analysis	56
2.2 X-Ray Diffraction	56
3 Thin films characterization	57
3.1 Thickness and roughness	57
3.2 Atomic Force Microscopy	57
3.3 X-Ray Diffraction	57
3.4 dc current-voltage measurements	58

CHAPTER 4

The $\text{Nb}_2\text{O}_5\cdot\text{SiO}_2$ Binary System: Results and Discussion 61

1 Synthesis	61
2 Chemical analysis	64
3 Thermal analysis	65
4 Structural characterization	67
4.1 X-Ray Diffraction	67
4.2 Raman spectroscopy	71
4.3 Fourier Transform Infrared spectroscopy	77
5 Textural and surface acidic characterization of catalysts	83
5.1 N_2 adsorption	83
5.2 Ammonia Temperature Programmed Desorption and Fourier Transform Infrared spectroscopy with probe molecules	87

6 Catalytic tests	96
6.1 Catalytic activity and reaction mechanism	96
6.2 Catalysts stability	101

CHAPTER 5

The $\text{Li}_2\text{O}\cdot\text{Nb}_2\text{O}_5\cdot\text{SiO}_2$ Ternary System: Results and Discussion 103

1 Bulk and flakes	103
2 Thin films	109
2.1 Thin films on Si-SiO ₂ substrates	110
2.1.1 X-Ray Diffraction	110
2.2 Thin films on Al ₂ O ₃ substrates	111
2.2.1 Atomic Force Microscopy	111
2.2.2 X-Ray Diffraction	114
2.2.3 dc current-voltage measurements	118

CONCLUSIONS 124

BIBLIOGRAPHY 128

List of Figures 139

List of Tables 143

List of Abbreviations 144

Acknowledgments

First of all, I would like to express my gratitude to Prof. Antonio Aronne, for providing me the opportunity to work in the research field of sol-gel technology, for his expert guidance and assistance in every aspects of this work.

I thank also Dr. Carmela Aruta for her support to my research activity and for giving me the occasion to increase my scientific competences.

I am grateful to Prof. Pasquale Pernice for his appreciated ideas about this project and for the encouragement and the confidence placed in me.

My thanks go to Dr. Esther Fanelli for the precious advices and suggestions given to me ever since I've known her.

I would also like to acknowledge Dr. Antonio Cassinese for the participation he showed in my work and for the stimulating discussions.

Special thanks go to Ing. Mario Barra for his generous help in the experimental phase and for offering constructive comments.

Finally, I wish to address my thanks to Prof. Marco Trifuoggi and Dr. Rosa Vitiello for the chemical analysis, Dr. Alessandro Vergara for the use of Raman spectrophotometer, Prof. Maria Turco and Dr. Giovanni Bagnasco for the use of TPD instrument, Prof. Gianguido Ramis for the FTIR spectra with probe molecules, Prof. Martino Di Serio and Prof. Elio Santacesaria for the N₂ adsorption measurements, Prof. Laura Depero, Prof. Elza Bontempi and Dr. Paolo Colombi for the AFM images, and Prof. Claudio De Rosa, Prof. Finizia Auriemma and Dr. Valeria Califano for the stimulating discussions. I'm grateful to them for the practical help they gave me, also in the elaboration of data.

INTRODUCTION

The synthesis and characterization of nanoparticles have attracted considerable attention in recent years. It is well known that nano-sized particles, because of their small size and high surface area display many unique properties such as electrical [1], optical [2], and magnetic [3, 4], somewhat different if compared to those of the bulk system. Nanoparticles, thanks to their special physical and chemical properties, now exhibit interesting applications also, in biology, catalysis, sensors, mechanics and electronics fields [5–7].

If nano-scaled particles are dispersed in a host matrix, a new nanocomposite material will be formed that possesses some unique properties both of the nanoparticles and the matrix.

The research activity of this PhD thesis was addressed to the sol-gel synthesis of inorganic nanocomposites based on highly dispersed and nanosized active phases that exhibit catalytic, electro-optic, ferroelectric, and non-linear optical properties. Particular attention was addressed to the thin films preparation, fundamental for the realization of electronic devices.

Compared with the conventional ceramic routes, such as coprecipitation, grafting, impregnation, the sol-gel exhibits many advantages, among them the low process temperature, the high control of purity, composition, microstructure and textural properties of the final material [8–10]. Particularly, for mixed-oxides this synthesis procedure allows to obtain materials characterized by a high dispersion

of the active phase in the matrix on both molecular and nanometer scale [11–16]. Moreover, the versatility of the sol-gel route makes possible to obtain the final material as powders, bulk and coating films.

For films fabrication, in comparison with the conventional deposition techniques, such as chemical vapor deposition, sputtering and pulsed laser deposition, the sol-gel offers a better control of the chemical composition, excellent homogeneity, low process temperature, uniformity over large area allowing to produce high-quality films up to micron thickness [8, 17].

In the first part of this work was explored the possibility to synthesize new nanocomposites catalysts in the $\text{Nb}_2\text{O}_5\cdot\text{SiO}_2$ binary system. Successively, the synthesis conditions to obtain nanocomposites in the $\text{Li}_2\text{O}\cdot\text{Nb}_2\text{O}_5\cdot\text{SiO}_2$ ternary system were explored. The aim was to prepare transparent thin films formed by lithium niobate nanocrystals uniformly dispersed in amorphous silica matrix.

A report of the most recent literature data about these materials is later on reported. This effort aims to provide a clear picture of the state of the art to clarify the actual interest and the novelty of the present work. Special emphasis is attributed to the influence of the process parameters on the control of the dispersion degree of the active phase in the silica matrix.

$\text{Nb}_2\text{O}_5\cdot\text{SiO}_2$

As concerns the catalysts, the nano-sized has a spectacular aspect on their properties: the different rate of variation of area and volume means a better use of the surface areas, and thus by decreasing particle size the catalytic activity may be promoted to a very high level, still unreachable. The greatest advantage foreseen

from using nano-sized catalysts will be the possibility to use a better tailored structure, leading to a specificity and a much increased selectivity. A promising potential area of development, concerns the possibility to obtain catalysts formed by nanoparticles dispersed in a host porous matrix, achieving materials that combine the chemical functionalities of the nanoparticles with the high surface area of the matrix [18]. Particularly, the possibility to obtain nanocomposites catalysts in situ, growing the active phase together the support matrix, instead of the traditional impregnation, has received much attention recently [9, 10]. In fact, in this case a greater stability at high temperature and a tailored porosity is achieved.

The niobium-silicon mixed-oxide composites have attracted great interest recently for their potential applications as heterogeneous catalysts [11–23, 19–21], confirming the active role played by these materials in several reactions, such as dehydration of alcohols, oxidative dehydrogenation, esterification, alkylation, epoxidation of olefins etc. [22, 23]. Among them, the epoxidation of olefins is an extremely important class of catalytic reaction in the chemical industry because of the epoxides versatility in preparing many chemical intermediates of importance to the fine and speciality chemicals. This type of reactions is generally carried out by using organic peracids and hydroperoxides as oxidants [24, 25]. Many efforts have been made to substitute these reagents with a “green oxidant” such as hydrogen peroxide H_2O_2 that can oxidize organic compounds with the generation of water as the only co-product [26–28]. The TS-1 (titanium silicalite) was the first heterogeneous and stable catalyst which demonstrated the possibility to epoxidize olefins with hydrogen peroxide [29]. From then, many semicrystalline

and amorphous mixed oxides based on silica and containing transition metal oxides such as Zr, W, Ti, Ta, Mo, Nb were proposed as catalysts for these reactions [21, 27, 30].

Mesoporous niobosilicates were found effective catalysts for cyclohexene [31, 32] and cyclooctene [33–35] epoxidation and their catalytic activity was found to be strongly influenced by niobium dispersion in the SiO₂ matrix [31, 32], and by synthesis conditions [33–35] as well. The acid properties of the materials [31, 32] and the niobium coordination [33–35] were hypothesized to play an important role in this reaction.

Nb₂O₅·SiO₂ catalysts can be synthesized by different procedures, besides the traditional impregnation [36], such as hydrothermal synthesis, eventually in the presence of cationic surfactants or expanders [31–35] or sol-gel [19, 21, 37, 38].

The choice of suitable molecular precursors plays a key role in the sol-gel synthesis of multi-components systems, such as Nb₂O₅·SiO₂. Actually, in order to obtain homogeneous sols, molecular precursors with comparable hydrolysis rates should be used [39, 40]. In this way cross-linking between clusters of different components with similar size will take place allowing gelation instead of precipitation and/or co-precipitation. In the former case gels formed by permanent covalent bonds (chemical gels) [41] are obtained, while in the latter, particulate gels, i.e. gels where temporary or reversible bonds connect the clusters, can be obtained (physical gels) [42].

In the SiO₂·Nb₂O₅ system, silicon alkoxides [11, 13, 15, 19–21, 43], among them tetraethoxysilane, Si(OC₂H₅)₄ (TEOS), or alkyl-alkoxysilane [12], were used

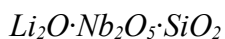
as silicon precursors, while niobium (V) ethoxide, $\text{Nb}(\text{OC}_2\text{H}_5)_5$, [11, 12, 19, 21] or niobium chloride, NbCl_5 , [13, 15, 19, 20, 43] were used as niobium precursors. Compared with $\text{Nb}(\text{OC}_2\text{H}_5)_5$, NbCl_5 is a low cost reagent and exhibits a higher reactivity that is usually controlled by dissolving it in ethanol, where it forms partially $\text{NbCl}_{5-x}(\text{OC}_2\text{H}_5)_x$ or completely substituted species. These species show higher reactivity towards water than silicon alkoxides that, consequently, have to be prehydrolyzed to some extent before the mixing to form the sol [11–13, 15, 19, 20]. In addition, niobium ions, Nb^{5+} , in aqueous environment undergo rapid hydrolysis giving rise to a precipitate of hydrated niobium pentoxide, $\text{Nb}_2\text{O}_5 \cdot n\text{H}_2\text{O}$. To prevent this phenomenon it is possible to use chelating agents, such as ethylenediaminetetracetic, citric and malic acids [44], 2,4-pentanedione [45], acetylacetone [21] or organic epoxides [43].

The complex chemical behaviour of niobium ions makes possible to obtain materials with different structural characteristics using slight differences in the synthesis procedure. Francisco and Gushikem [13] prepared three $\text{SiO}_2 \cdot \text{Nb}_2\text{O}_5$ composites containing different Nb_2O_5 amounts (2.5, 5.0 and 7.5 mol%) using a synthesis procedure characterized by a high $\text{H}_2\text{O}/\text{TEOS}$ molar ratio (about 70:1) and a high processing temperature in order to facilitate both TEOS prehydrolysis and gelation process. In these gel derived samples evidences of Si–O–Nb bonds were found by Fourier Transform Infrared spectroscopy (FTIR) [13] and X-ray Photoelectron Spectroscopy (XPS) [14] indicating a strong interaction of niobium with the siloxane matrix. The authors [13, 14] proposed a structural model consisting of amorphous domains of Nb_2O_5 uniformly dispersed into the siloxane matrix. Increasing the temperature these domains cluster to facilitate the

formation of nanocrystals of different Nb₂O₅ polymorphs depending on the metal oxide amount in the sol-gel matrices [13, 14]. On the other hand, Drake et al. [11] synthesized three SiO₂·Nb₂O₅ composites with Nb₂O₅ loadings equal to 3.0, 7.5 and 30 mol% using a different procedure, at room temperature, characterized by a lower H₂O/TEOS molar ratio (about the stoichiometric one for a full hydrolysis). These authors showed by multinuclear solid state NMR experiments that the structure of the gels at low Nb₂O₅ contents do not contain Nb–O–Nb bonds [11]. These bonds were found only in the gel with 30 mol% of Nb₂O₅ showing that the structure of this sample is phase separated on the atomic scale containing domains of Nb₂O₅ and SiO₂ [11]. On the contrary, in the gels at lower Nb₂O₅ amounts all the niobium is uniformly distributed throughout the siloxane network [11].

In the present work, Nb₂O₅·SiO₂ gels were synthesized at room temperature by a new sol-gel route. A wide compositional range was explored, with Nb₂O₅ content ranging from 2.5 to 20 mol%. With the aim to obtain a tailored catalyst, it was evaluated the influence of the synthesis procedure on the structural characteristics of the gel derived samples and on their evolution with the temperature. Special attention was addressed to how niobium is dispersed in the siloxane matrix. Firstly, the chemical analysis of each sample was performed by spettofotometry and a wide thermal and structural characterization was made by Thermogravimetry/Differential Thermal Analysis (TG/DTA), X-Ray Diffraction (XRD), Raman and FTIR spectroscopy. Successively, textural and acidic properties of the gels were characterized by N₂ adsorption, ammonia Temperature Programmed Desorption (NH₃ TPD) and FTIR of probe molecules. Finally, the

materials were tested as catalysts for the epoxidation of cyclooctene with hydrogen peroxide.



In the last years, plenty of efforts have been spent for the fabrication and modeling of new memory devices based on polymers [46–48], organic materials [49–52], oxides [53] or nanocomposites [7, 54–58], where either ferroelectric behavior or conductance switching have been exploited. Among them, nanocomposites materials appear very attractive for data storage or memory applications due to their advantages in size allowing to provide high-density memory elements. Up to now, either Au [54], CdSe [55, 56] and ZnO [57, 58] nanoparticles embedded in an organic layer or organic composites formed both by an organic semiconductor adsorbed on carbon nanotubes [7] and by a charge donor and acceptor system embedded into a polymer matrix [59] have been obtained. Recently, multifunctional materials showing both bistability and other functionalities have been reported [60].

In this context, a little work exists on inorganic nanocomposite bistable materials such as lithium niobate, $LiNbO_3$, that displays both ferroelectric and non-linear optical properties. As a matter of fact, $LiNbO_3$ is a ferroelectric and non-linear optical material widely used in integrated and waveguides optics, as well as in piezoelectric applications.

According to the $Li_2O \cdot Nb_2O_5$ phase diagram [61], $LiNbO_3$ has a wide solid solution region extending from the Nb-rich side ($Li/[Nb + Li]$ about 0.47) to the stoichiometric point ($Li/[Nb + Li] = 0.50$). The congruent composition of $LiNbO_3$

exists between 48.35 and 48.65 mol% Li_2O . Therefore, when this material is obtained from high temperature processes, such as single-crystal Czochralski growth, non-stoichiometric crystals with Li_2O deficiency are generally obtained [62, 63]. It is well known that the electro-optic and non-linear effects of the stoichiometric LiNbO_3 (SLN) are superior to those of a non-stoichiometric [64].

In view of possible applications, SLN in form of thin films is fundamental. However, SLN thin film formation is a difficult task. In this respect, low temperature wet chemical techniques, and among them the sol-gel [44, 65–68, 69–71], are by far the most valuable, because of the incongruent melting of SLN.

As for the above binary system, the stabilization of Nb^{5+} ion in aqueous environment is fundamental in this case too.

Hirano et co-workers [65, 66] starting from an alcoholic solution of lithium-niobium ethoxide, $\text{LiNb}(\text{OC}_2\text{H}_5)_6$, have utilized the high reactivity of Nb^{5+} ion in an aqueous environment to obtain a solution of mixed lithium-niobium hydroxide, $\text{LiNb}(\text{OH})_6$, from which thin crystalline films of SLN are obtained by dip-coating. The need of handling the precursors under a dry inert atmosphere and the precise control of the hydrolysis step are the main disadvantages of this procedure (that is called “double alkoxides”). An innovation in this sol-gel route, the addition of hydrogen peroxide solution to the alcoholic solution of $\text{LiNb}(\text{OC}_2\text{H}_5)_6$, has been introduced by Cheng et al. [67] obtaining a slight improvement of the precursors handling and a lower temperature processing as well.

The easy achievement of nanocrystalline LiNbO_3 is another advantage of the wet chemical techniques [69–71]. Nanocrystalline LiNbO_3 particles of about 20 nm dispersed in a silica matrix (20% by weight), with a grains structure very

similar to that of the bulk material but with enhanced transport properties, have been obtained by the “double alkoxides” route [70]. It was shown that SiO_2 play a key role to prevent the growth of nanocrystals hindering their coarsening also at high temperature [70, 71]. By the same route $\text{LiNbO}_3 \cdot \text{SiO}_2$ sol-gel films, with $\text{LiNbO}_3/\text{SiO}_2$ molar ratio equal to 1, have been synthesized by Bescher et al. [72]. Films annealed 2 h at 473 K appeared transparent and exhibited a ferroelectric-like behavior even if were amorphous to XRD. This behavior was related to the presence in the silica matrix of nanoclusters with size of 3–5 nm (named “ferrons”) as revealed by high-resolution transmission electron microscopy (HRTEM) pictures, that the authors considered nanocrystallites-like [72]. Recently, $\text{LiNbO}_3 \cdot \text{SiO}_2$ glass-ceramics with a LiNbO_3 content changing from 4 to 6 mol% have been synthesized by Graça et al. [73–75] in flakes shape using a sol-gel route that can be considered a slight modification of that proposed by Cheng et al. [67]. It was found that in the samples subjected to electric gradient of 1000 kV/m the crystallization of LiNbO_3 started to occur at 923 K while in absence of electrical field it occurred at 973 K [73]. Moreover, in the 873–1073 K range besides LiNbO_3 also crystobalite, $\text{Li}_2\text{Si}_2\text{O}_5$ and Li_3NbO_4 were found to crystallize [75].

In this work, gels in the $\text{Li}_2\text{O} \cdot \text{Nb}_2\text{O}_5 \cdot \text{SiO}_2$ ternary system were prepared, by a suitable modification of the sol-gel route tuned to synthesize gels in the $\text{Nb}_2\text{O}_5 \cdot \text{SiO}_2$ binary system. In the current case, it was investigate the possibility to using inorganic niobium and lithium low-cost precursors, and only one alkoxide.

A wide compositional range was explored, ranging from 5 to 15 mol% of Li_2O and Nb_2O_5 . To find the suitable process parameters for the $\text{LiNbO}_3 \cdot \text{SiO}_2$ thin

film preparation, at the first stage, bulk gels were synthesized then, as intermediate step to approach the film preparation, a synthesis procedure was set to obtain transparent flakes with thickness lower than 0.5 mm. Finally, the suitable sol-gel route was set to obtain transparent thin films by dip coating.

The films were annealed at different temperature and widely characterized by Atomic Force Microscopy (AFM), Glancing Incidence XRD (GIXRD) and dc current-voltage (I-V) measurements.

PUBLICATIONS

Publications included in this PhD thesis

Papers

1. Elisa Marenga, Antonio Aronne, Esther Fanelli, Pasquale Pernice, “*Sol gel synthesis of nanocomposite materials based on Lithium Niobate nanocrystals dispersed in a silica glass matrix*”, submitted to Journal of Solid State Chemistry.
2. Elisa Marenga, Carmela Aruta, Elza Bontempi, Antonio Cassinese, Paolo Colombi, Laura E. Depero, Pasquale Pernice, Antonio Aronne, “*Novel sol-gel synthesis of transparent and electrically bistable $\text{LiNbO}_3\text{-SiO}_2$ nanocomposites thin films*”, Journal of Sol-Gel Science and Technology DOI 10.1007/s10971-008-1834-9.
3. Antonio Aronne, Maria Turco, Giovanni Bagnasco, Gianguido Ramis, Elio Santacesaria, Martino Di Serio, Elisa Marenga, Maria Bevilacqua, Claudia Cammarano, Esther Fanelli, “*Gel derived niobium-silicon mixed oxides: characterization and catalytic activity for cyclooctene epoxidation*”, Applied Catalysis A: General, 347 (2008) 179-185.

4. Antonio Aronne, Elisa Marennna, Valeria Califano, Marco Trifuoggi, Alessandro Vergara, Esther Fanelli, Pasquale Pernice, “*Sol-gel synthesis and structural characterization of niobium-silicon mixed-oxide nanocomposites*”, Journal of Sol-Gel Science and Technology, 43 (2007) 193-204.

Abstracts Book

5. Elisa Marennna, Antonio Aronne, Pasquale Pernice, Maria Turco, Giovanni Bagnasco, Gianguido Ramis, Elio Santacesaria, Martino Di Serio, Maria Bevilacqua, Esther Fanelli, Serena Esposito “*Sintesi via sol-gel di ossidi misti Nb₂O₅-SiO₂: caratterizzazione e attività catalitica nell’epossidazione del cicloottene*”, Abstracts Book of VI Convegno Nazionale AICIng, Associazione Italiana Chimica per l’ingegneria , Ischia, 25-27 Settembre 2008.

6. Elisa Marennna, Maria Turco, Giovanni Bagnasco, Gianguido Ramis, Elio Santacesaria, Martino Di Serio, Pasquale Pernice, Antonio Aronne, Maria Bevilacqua, Claudia Cammarano, Esther Fanelli *Gel derived niobium-silicon mixed-oxides catalysts for cyclooctene epoxidation*. Abstracts Book of VI Workshop Italiano Sol-Gel, Lecce, 19-20 Giugno 2008.

7. Elisa Marennna, Elio Santacesaria, Pasquale Pernice, Martino Di Serio, Antonio Aronne “*Sintesi via sol-gel di catalizzatori a base di Nb₂O₅-SiO₂ per reazioni di epossidazione*”, Abstracts Book of II Workshop Nazionale AICIng 2007, Messina, 12-14 Settembre 2007.

8. A. Aronne, E. Marenga, P. Pernice, G. Ramis, M. Bevilacqua, M Trifuoggi, M. Di Serio, E. Santacesaria, A. Vergara, R. Vitiello, “*Niobium-silicon mixed-oxides catalysts by sol-gel*”, Abstracts Book of XIVth International Sol-Gel Conference, Montpellier – France, September 2-7 2007.

9. E. Marenga, A. Aronne, V. Califano, M. Trifuoggi, R. Vitiello, A. Vergara, E. Fanelli, P. Pernice, “*Sol-gel synthesis and structural characterization of niobium-silicon mixed-oxide nanocomposites*” Abstracts Book of Composite materials: from molecular Sciences to Nanotechnology-Physical Chemistry Division, 3-8 Settembre 2006, Villa Gualino (Torino).

10. Antonio Aronne, Pasquale Pernice, Serena Esposito, N.J. Clayden, Maria Turco, Giovanni Bagnasco, Martino Di Serio, Elisa Marenga, Esther Fanelli, “*Mixed oxide nanocomposites by sol-gel synthesis for acidic catalysis*” Abstracts Book of V Workshop Italiano Sol-gel, 22-23 Giugno 2006, Milano.

Publication not included in this PhD thesis

Papers

11. Antonio Aronne, Maria Turco, Giovanni Bagnasco, Pasquale Pernice, Martino Di Serio, Elisa Marenga, Esther Fanelli, “*Synthesis of high surface area phosphosilicate glasses by a modified sol-gel method*”, Chemistry of Materials, 17 (2005) 2081-2090.

Abstracts Book

12. E. Fanelli, A. Aronne, S. Esposito, P. Pernice, A. Fragneto, E. Marennna, “*Thermal and structural characterization of potassium-sodium niobosilicate glasses*”, Abstracts Book of 8th Mediterranean Conference on Calorimetry and Thermal Analysis, 25-29 Settembre 2007, Palermo.

13. N. J. Clayden, S. Esposito, P. Pernice, M. Turco, G. Bagnasco, E. Marennna, E. Fanelli, A. Aronne, “*Chemical environment of phosphorus in phosphosilicate gel-derived materials*”, Abstracts Book of XIVth International Sol-Gel Conference, Montpellier – France, September 2-7 2007.

CHAPTER 1

The Sol-Gel Technology

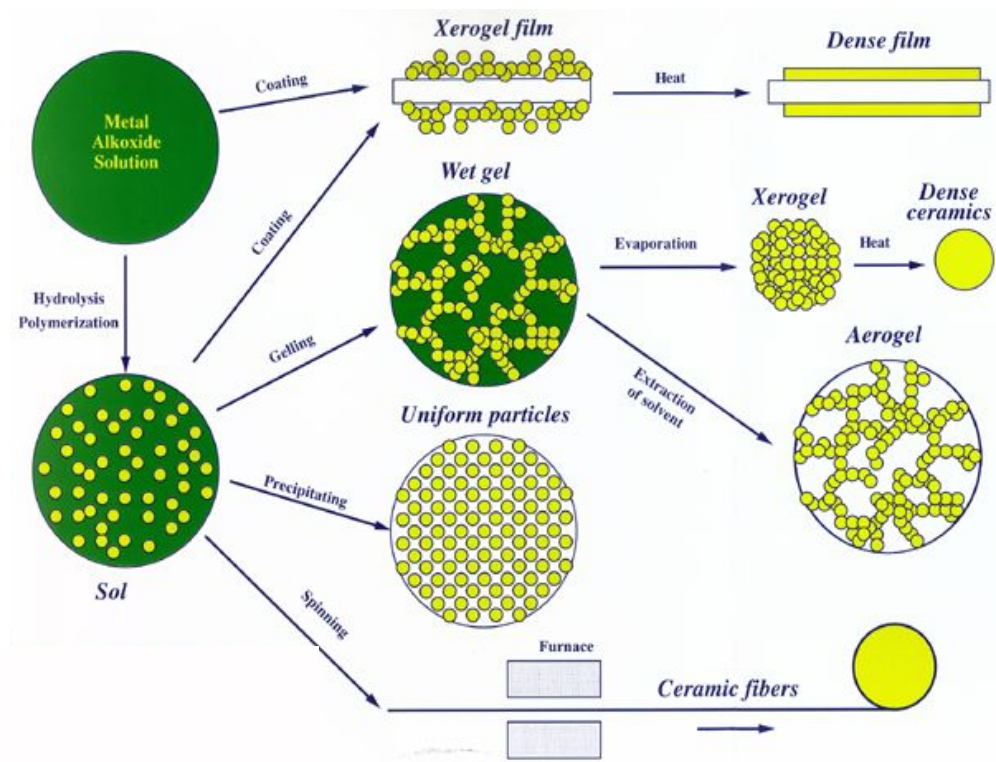


Fig. 1.1 Sol-gel process.

The sol-gel process is a versatile wet chemical process to make ceramic and glass materials. This synthesis technique involves the transition of a system from a colloidal liquid, named sol, into a solid gel phase [8, 76, 77]. The sol-gel technology allows to prepare ceramic or glass materials in a wide variety of

forms: ultra-fine or spherical shaped powders, thin film coatings, ceramic fibres, microporous inorganic membranes, monolithics, or extremely porous aerogels. An overview of the sol-gel process is illustrated in Figure 1.1.

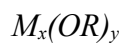
This technique offers many advantages among them the low process temperature, the ability to control the composition on molecular scale and the porosity to obtain high surface area materials, the homogeneity of the final product up to atomic scale. Moreover, it is possible to synthesize complex composition materials, to form higher purity products through the use of high purity reagents, and to provide coatings over complex geometries [8, 76, 77]. The sol-gel process allows to obtain high quality films up to micron thickness, difficult to obtain using the physical deposition techniques. Moreover, it is possible to synthesize complex composition materials and to provide coatings over complex geometries [8, 76, 77].

The starting materials used in the preparation of the sol are usually inorganic metal salts or metal organic compounds, that by hydrolysis and polycondensation reactions form the sol [8, 76, 77]. Further processing of the sol enables one to make ceramic materials in different forms. Thin films can be produced by spin-coating or dip-coating. When the sol is cast into a mould, a wet gel will form. By drying and heat-treatment, the gel is converted into dense ceramic or glass materials. If the liquid in a wet gel is removed under a supercritical condition, a highly porous and extremely low density aerogel material is obtained. As the viscosity of a sol is adjusted into a suitable viscosity range, ceramic fibres can be drawn from the sol. Ultra-fine and uniform ceramic powders are formed by precipitation, spray pyrolysis, or emulsion techniques.

1 Sol-gel chemistry

1.1 The role of the precursors

Commonly, the most preferred starting reagents are alkoxides with general formula :



where $M = \text{element with valence } y$

$R = \text{alkoxide group}$

These alkoxides must exhibit useful properties to control the chemical synthesis of oxides:

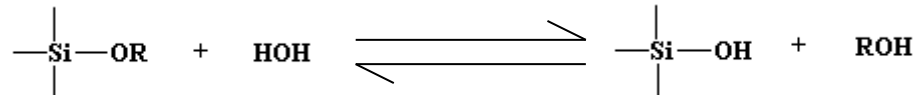
1. *easy to purify*, a lot of alkoxides can be distilled in order to obtain highly pure products;
2. *wide variety*, it is possible to choose R among a large number of alkylic groups in order to obtain the required reactivity;
3. *possible control*, of the alkoxides hydrolysis and the polycondensation of hydrolysed species;
4. *mixed alkoxides*, as a further control means of the stoichiometry and homogeneity of the final products.

1.2 Gelation: hydrolysis and polycondensation

The transition from sol to gel involves two key steps, such as hydrolysis and polycondensation reactions. The hydrolysis takes place also by small amounts

of water. Because water and alkoxides are immiscible, a mutual solvent such as alcohol, is normally used as a homogenizing agent.

In the hydrolysis reaction, the alkoxide groups (OR) are replaced stepwise by hydroxyl groups (OH):



The hydrolysis rate depends on many factors. Indeed, the reaction can favourably be promoted by an increase in the charge density on the metal, the number of metal ions bridged by a hydroxo- or oxo-ligand, and the size of the alkyl groups [78, 79]. Conversely, inhibition occurs as the number of hydroxo-ligand coordinating M increases or when the pH, temperature, or water and solvent amount tend to favour the reverse reaction (esterification).

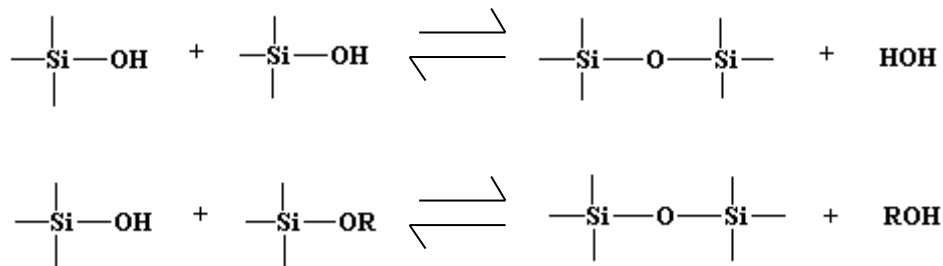
As concerns the metal oxides, due to high oxygen electronegativity compared to the metal, the M-O-M bonds are generally highly polarized and the hydrolysis rates are high. On the contrary, the hydrolysis rates of non-metal alkoxides (M = Si, P, Ge..) are slower.

This aspect is very important for multi-component systems (mixed oxides) where the different hydrolysis rates of the precursors give to different gelation times, by means of homo-condensation instead of hetero-condensation, with formation of M-O-M and M'-O-M' instead of M-O-M' linkages. In this case a non-homogeneous gel is formed.

Many solutions can be adopted to solve the above problem:

1. modification of the hydrolysis rate of the more reactive precursor using reaction inhibitors (for example chelants);
2. use of double alkoxides, with precise stoichiometry;
3. modification of the hydrolysis rate of the slower precursor by a catalyzed pre-hydrolysis (acid or basic).

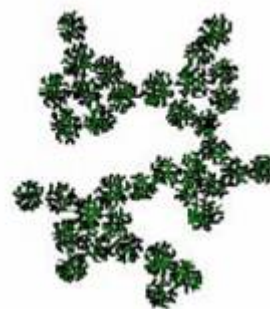
Simultaneously to the hydrolysis, the polycondensation reactions occur:



The polycondensation reactions involve hydroxyl groups and result in M-O-M' linkages which, in turn, yield a three dimensional network, the gel, upon a polymeric weight and cross-linking degree increase. The gel state is then best described as a viscoelastic material composed of interpenetrating solid and liquid phases [80]. Its structure is strongly dependent on the water content in the system and on the catalysis nature. In acidic solution or for low water concentration, weakly crosslinked linear chains are produced (see Figure 1.2a), resulting in a soft gel which can be readily redispersed in solution. On the other hand, in based-catalyzed solutions, branched clusters are preferentially formed (see Figure 1.2b) and their tendency to coalesce is responsible of the solution gelation [4, 5].



(a)



(b)

Fig. 1.2 Gel structure: **a** crosslinked linear chains; **b** branched clusters.

1.3 Transformations of the gel

The wet gel, obtained by the alkoxide hydrolysis and polycondensation reactions, itself is not an end product. In fact, it is necessary a drying stage and a suitable thermal treatment in order to obtain the material, glass or ceramic, with the required characteristics.

In the drying process, the wet gel is heated at about 373 K for a time that allows the desorption of water and residual alcohol physically linked to the polymeric network.

Many difficulties arise during the drying stage, mainly caused by the removal of large amounts of solvent trapped in the polymeric network. The transformation of the wet gel in dried gel leads to a volume decrease, and it is often associated with the formation of cracks. To minimize these effects, gels are dried by slow heating rate and for coatings, the thickness usually must not exceed 10 μm .

Usually, the dried gel is annealed in the temperature range 573–773 K to remove the residual organic groups. During these heat-treatments, condensation reactions

among residual alkoxides groups, both on surface and inside the gel, can take place.

Successively, suitable heat-treatments allow to obtain the desired final material.

2 Dip-coating technique

One of most interesting aspects of the sol-gel technique is related to the possibility to employ the homogeneous solution obtained before the gelation in order to prepare thin films by means of the deposition techniques of spin and dip-coating. In this research project the dip coating technique was used.

The dip-coating technique can be described as a film deposition process where the substrate to coated is immersed in a liquid and then withdrawn with a well-defined speed under controlled temperature and atmospheric conditions. The coating thickness is mainly defined by the withdrawal speed, the solid content and the viscosity of the liquid. If the withdrawal speed is chosen such that the shear rates keep the system in the Newtonian regime, the coating thickness can be calculated by the Landau-Levich equation [81]:

$$h = 0.94(\eta U)^{2/3} / \gamma_{LV}^{1/6} / (\rho g)^{1/2}$$

where

h = coating thickness

η = viscosity

U = substrate speed

γ_{LV} = liquid-vapour surface tension

ρ = density

g = gravity

As shown by James and Strawbridge [82] for an acid catalyzed silicate sol, the thickness obtained experimentally fit very well the calculated one. Choosing an appropriate viscosity the coating thickness can be varied with high precision from 20 nm up to 50 μm while maintaining high optical quality. The schematics of a dip coating process are shown in Figure 1.3.

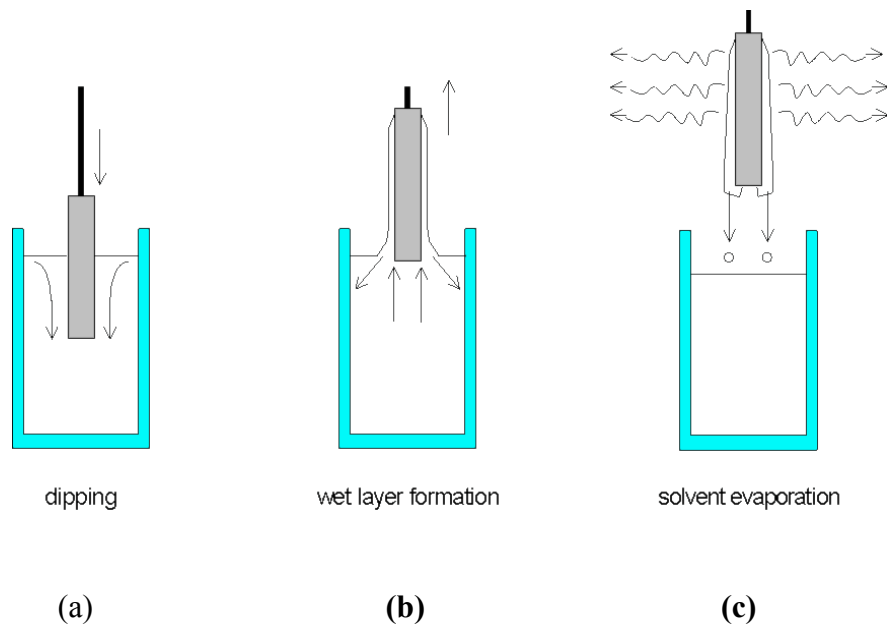


Fig. 1.3 Stages of the dip coating process: **a** dipping of the substrate into the coating solution; **b** wet layer formation by withdrawing the substrate; **c** gelation of the layer by solvent evaporation.

If reactive systems are chosen for coatings, as it is the case in sol-gel type of coatings using alkoxides or pre-hydrolyzed systems, the control of the atmosphere is indispensable. The atmosphere controls the evaporation of the solvent and the

subsequent destabilization of the sols by solvent evaporation, leads to a gelation process and the formation of a transparent film due to the small particle size in the sols (nm range) [83]. This is schematically shown in Figure 1.4.

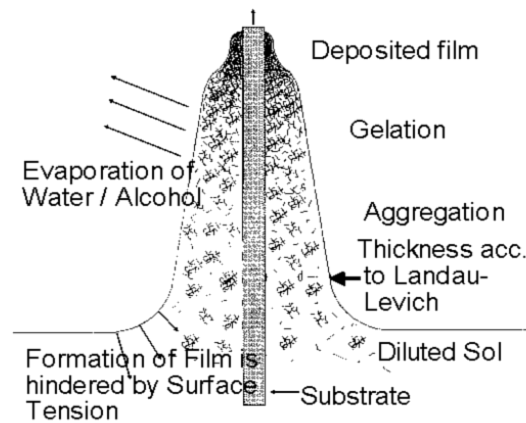


Fig. 1.4 Gelation process during dip-coating process, obtained by evaporation of the solvent and subsequent destabilization of the sol.

Generally, sol particles are stabilized by surface charges, and the stabilization condition follows the Stern's potential consideration [84]. According to Stern's theory the gelation process can be explained by the approaching of the charged particle to distances below the repulsion potential. Then the repulsion is changed to an attraction leading to a very fast gelation. This takes place at the gelation point as indicated in Figure 1.4. The resulting gel then has to be densified by thermal treatment, and the densification temperature is depending on the composition. But due to small size of the gel particles, the system shows a large excess energy and in most cases a remarkably reduced densification temperature compared to bulk-systems is observed.

Dip-coating processes are used for plate glass by Schott, based on developments of Schröder [85] and Dislich [86] for solar energy control systems (Calorex) and anti-reflective coatings (Amiran) on windows. The dip coating technique is also applied for optical coatings, e.g. on bulbs, for optical filters or dielectric mirrors by various companies, fabricating multilayer systems formed by 30 or 40 coatings with very high precision.

CHAPTER 2

The Nb₂O₅·SiO₂ Binary System:

Experimental

1 Synthesis

Niobium-silicon mixed-oxide nanocomposites, whose nominal composition can be expressed by the formula (Nb₂O₅)_x·(SiO₂)_{100-x} with $x = 2.5$ (*2.5Nb*), 5 (*5Nb*), 10 (*10Nb*) and 20 (*20Nb*), were prepared by sol-gel according to the procedure showed in the flow-chart (see Figure 2.1). Niobium chloride, NbCl₅ (99%, Gelest), and tetraethoxysilane, Si(OC₂H₅)₄ (TEOS) (99%, Gelest), were used as starting materials. A solution of NbCl₅ in anhydrous ethanol (EtOH) having a molar ratio NbCl₅ : EtOH = 1 : 6 was prepared in a dry box at room temperature. This solution was fluxed with dry-air for 20 min to allow the HCl removal and the formation of partially substituted Nb(OEt)_{5-x}(Cl)_x species. An alcoholic solution of TEOS with molar ratio TEOS : EtOH = 1 : 4 was stirred for 5 min and then mixed with the first one. The resulting clear solution was hydrolyzed, under stirring, at room temperature using a HCl hydro-alcoholic solution so to obtain the final molar ratio TEOS : H₂O : HCl = 1 : 4 : 0.01. From this final solution transparent wet gels were obtained for all compositions at room

temperature. The gelation occurs no later than two days for each studied composition.

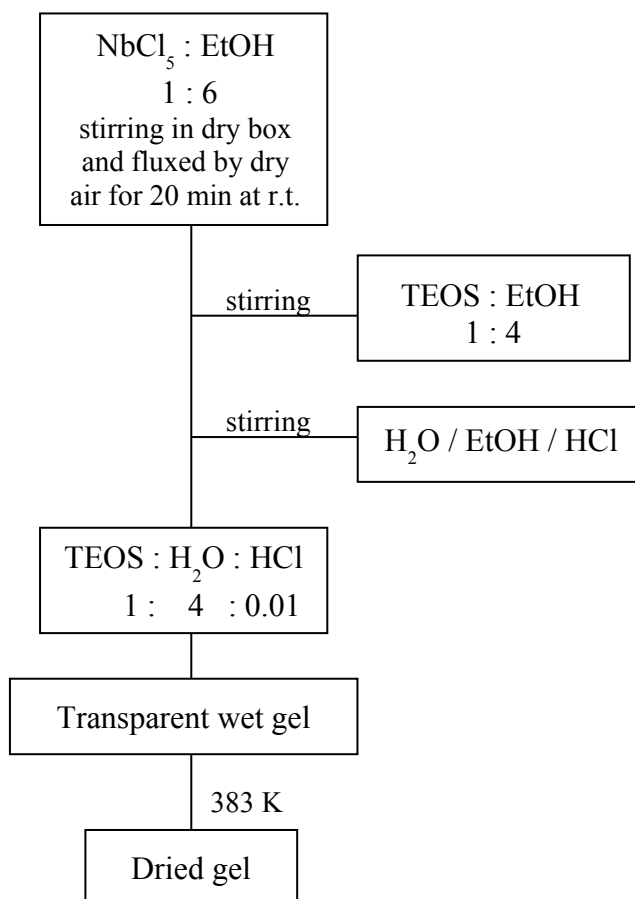


Fig. 2.1 Flow-chart of the gels synthesis procedure showing the molar ratios employed.

The gelled systems were kept for 2 days at room temperature before drying, to allow the completion of polycondensation reactions. Then, the gels were fully dried in air at 383 K in an electric oven for 3 days. After these treatments, yellow transparent and amorphous hardened dry gels were obtained for all compositions. Wet and dried gels of the sample 20Nb are displayed in Figure 2.2.

The catalysts were obtained by finely grounding the hardened dry gels and then calcining at 673 K for 3 h. For comparative purpose, SiO_2 gels were prepared

under the same conditions (see Figure 2.3) while Nb_2O_5 was commercial powder (Gelest, 99.9%).



(a)



(b)

Fig. 2.2 Sample $(\text{Nb}_2\text{O}_5)_{20} \cdot (\text{SiO}_2)_{80}$ (*20Nb*): **a** wet gel; **b** dried gels.



Fig. 2.3 Dried SiO_2 gel.

2 Chemical analysis

The actual niobium and silicon contents in the final product were determined by spectrophotometry.

To execute the chemical analysis the hardened dry gels were finely ground in an agate mortar and heated at a heating rate of 5 K min^{-1} up to 873 K and kept at this temperature for 1 h, in an electric oven. The resulting heat-treated powders were dissolved in a fluoridric acid solution (HF, 37%, Fluka), according to standard procedures [87-90].

The niobium was determined by the hydrogen peroxide method [87]. The niobium oxidation in a sulphuric acid solution (H_2SO_4 , 95-97% J.T. Baker) with hydrogen peroxide (H_2O_2 , 30% Fluka) gives to the formation of the yellow perniobic acid with a maximum absorbance at $\lambda=342 \text{ nm}$.

Since both H_2SO_4 and H_2O_2 can influence the maximum absorbance value, many experimental tests were carried out to find the conditions that maximize the absorbance signal [87-89]. It was found that the maximum absorbance signal occurs for the solutions of H_2SO_4 70% weight and H_2O_2 0.02% volume.

Standard solutions, at fixed niobium contents (from 5 to 100 ppm), were prepared starting from a niobium atomic absorption standard solution (Nb 1000 $\mu\text{g/ml}$, Aldrich). A calibration line absorbance versus niobium concentration was built evaluating the absorbance at $\lambda=342 \text{ nm}$ of the above standard solutions (see Figure 2.4) that allows to determine the actual niobium contents.

The error in the niobium determination was 3%.

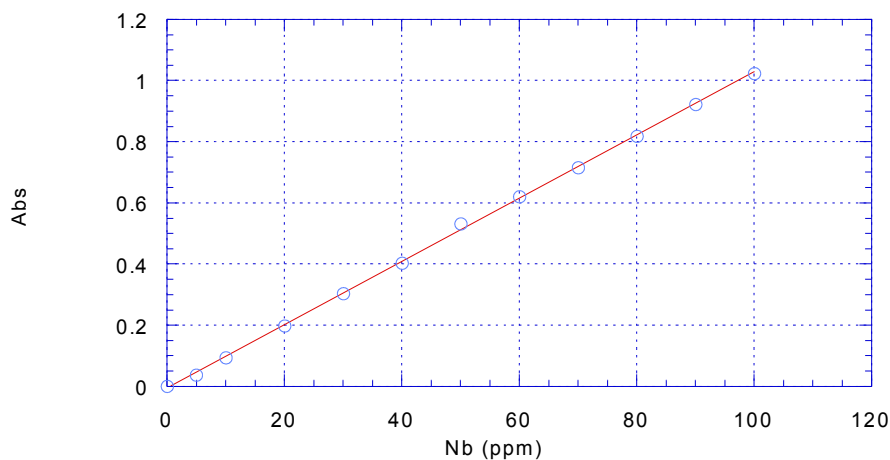


Fig. 2.4 Calibration line absorbance versus niobium concentration.

The silicon was determined as amount of soluble silica.

The silicic ion reacts with the ammonium molybdate giving to the formation of a yellow complex, the intensity is proportional to the silica concentration in the analyzed sample [90].

For the silica determination, an aqueous hydrochloric acid solution (HCl : H₂O = 1 : 1, volume ratio), ammonium molybdate and oxalic acid were used. The ammonium molybdate at pH ~ 1.2 reacts both with the silica and with phosphate ions, if there are. The possible interferences due to the presence of phosphate ions are removed by adding the oxalic acid that decomposes the molybdophosphoric acid but not the molybdosilicic one.

Standard solutions, at fixed silicon contents (from 3 to 20 ppm), were prepared starting from a silicon atomic absorption standard solution (Si 1.000 g/L, Fluka).

A calibration line absorbance versus silica concentration was built evaluating the

absorbance at $\lambda=410$ nm of the above standard solutions (see Figure 2.5) that allows to determine the actual silica contents.

The error in the silicon determination was 4%.

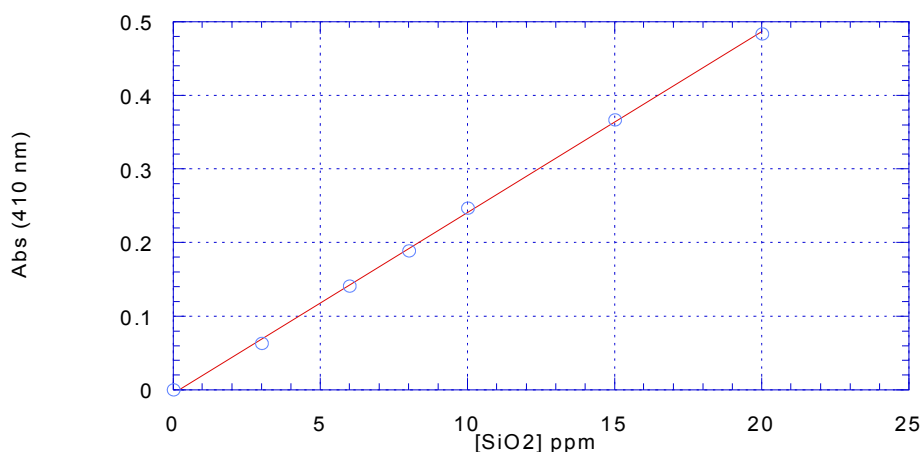


Fig. 2.5 Calibration line absorbance versus soluble silica concentration.

3 Thermal analysis

The nature and temperatures of the various reactions occurring during the heating were evaluated by DTA. Simultaneously, it was registered the TG curve to evaluate the weight loss of the gel by heating.

The DTA was carried out by using a high temperature DTA unit (Netzsch, DSC 404 model) with Al_2O_3 as reference material. The DTA curves, recorded in air from room temperature up to 1273 K at a heating rate of 10 K min^{-1} , were carried out on about 30 mg of dried gel specimens. The TG analysis was performed on a thermobalance (Netzsch, TG 209 model) in $100 \text{ mL min}^{-1} \text{ N}_2$ flow with 10 K min^{-1} heating rate.

4 Structural analysis

4.1 X-Ray Diffraction

The amorphous nature of the dried gels as well as the nature of the crystallizing phases were ascertained by XRD. The spectra of dried gels, finely ground and heated at a heating rate of 5 K min⁻¹ up to 673 K and kept at this temperature for 3 h and 873, 1073, 1273 and 1473 and kept at these temperatures for 1 h, were registered. The spectra were collected by a Philips diffractometer model PW1710 (Cu K α , $\lambda=1.5418$ Å) with a scan rate of 1° min⁻¹.

4.2 Raman spectroscopy

The Raman spectra of dried gels, finely ground and heated at a heating rate of 5 K min⁻¹ up to 673 K and kept at this temperature for 3 h and 873, 1073, 1273 and 1473 K and kept at these temperatures for 1 h, were registered. A confocal Raman microscope (Jasco, NRS-3100) was used to obtain Raman spectra for the powdered samples. The 488 nm line of an aircooled Ar⁺ laser (Melles Griot, 35 LAP 431–220), 125 mW, was injected into an integrated Olympus microscope and focused to a spot size of approximately 2 μ m by a 100 \times or 20 \times objective. A holographic notch filter was used to reject the excitation laser line. Raman scattering was collected by a peltier-cooled 1024 \times 128 pixel CCD photon detector (Andor DU401BVI). For most systems, it takes 100 s to collect a complete data set.

4.3 Fourier Transform Infrared spectroscopy

FTIR spectroscopy was used to have a detailed analysis of material structure and to point out the possible modifications that it can undergo with the heating. The dried gels were heated at a heating rate of 5 K min^{-1} up to 673 K and kept at this temperature for 3 h and 873, 1073, 1273 and 1473 K and kept at these temperatures for 1 h. The FTIR spectra of dried and heat-treated gel samples were carried out at room temperature by a Nicolet system, Nexus model, equipped with a DTGS KBr (deuterated triglycine sulfate with potassium bromide windows) detector. The absorption spectra were recorded in the $4000\text{--}400 \text{ cm}^{-1}$ range with a spectral resolution of 2 cm^{-1} on samples diluted in KBr. In fact, mixture 2% weight of each sample in KBr was prepared and, 200 mg of this mixture were successively pressed in form of tablets with diameter of 13 mm. The spectrum of each sample represents an average of 64 scans, which was corrected for the spectrum of the KBr blank. To allow the comparison of the absorbance values, all FTIR spectra were normalized with respect to the maximum absorbance value recorded for each spectrum.

5 Textural analysis

5.1 N_2 adsorption

The surface areas were determined by N_2 adsorption-desorption isotherms at -77 K using a Carlo Erba-Fisher apparatus model 1990, displayed in Figure 2.6. The sample was previously treated in the sample cell at 443 K under vacuum up to complete degassing. Then, constant amounts of N_2 (8 cm^3 at STP) were automatically introduced up to saturation. The N_2 desorption was carried out stepwise by constant volume drawings (4 cm^3 at 287 K and at each equilibrium

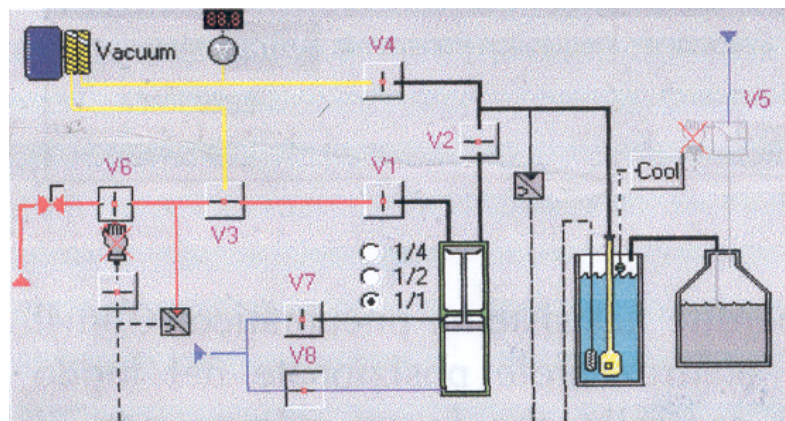


Fig. 2.6 Carlo Erba-Fisher apparatus model for surface area determination.

pressure). From the measured pressure values, the amounts of N_2 retained by the sample at each adsorption or desorption step were calculated.

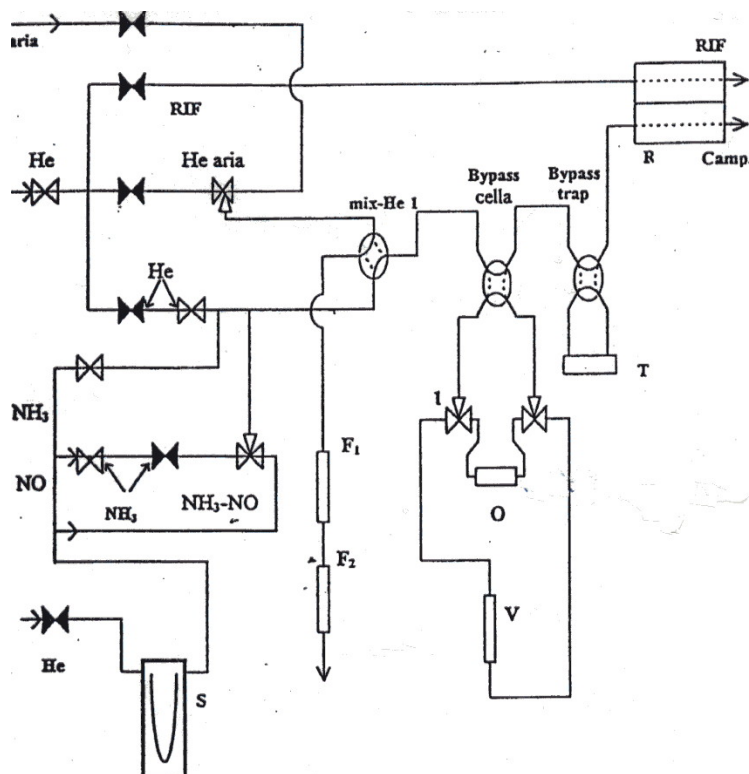
The N_2 adsorption-desorption isotherms were elaborated by the BET method for the calculation of the surface areas [91]. The α -plot method was also employed for the calculation of the surface areas and micropore volumes [91]. Pore volumes were determined from the amounts of adsorbed N_2 at $P/P^\circ = 0.98$ (desorption curve), assuming the presence of liquid N_2 (density = 0.807 g cm^{-3}) in the pores under these conditions. The pore size distribution was determined by application of the BJH method [91].

5.2 Ammonia Temperature Programmed Desorption and Fourier Transform Infrared spectroscopy with probe molecules

NH_3 TPD and FTIR spectra with probe molecules were used to characterize the surface acidity.

NH_3 TPD measurements were carried out in a flow apparatus equipped

with pure NH_3 and He lines regulated by electronic devices and a TCD detector (see Figure 2.7).



O: horizontal cell; V: vertical cell; S: saturator; T: trap; F1, F2: flow meters.

Fig. 2.7 TPD flow apparatus model.

The sample, previously heated at 673 K in He flow for 1 h, was saturated with NH_3 by flowing a 1% NH_3/He mixture at room temperature. After the sample was purged in a He flow to eliminate loosely bonded NH_3 , it was heated at a constant rate of 10 K min^{-1} up to 873 K in He flow ($30 \text{ cm}^3 \text{ min}^{-1}$). The NH_3 concentration evolved from the sample during heating was continuously measured by the TCD. A PC was employed for acquiring and elaborating the TCD signal. Water

eventually released by the sample was removed by a KOH trap to avoid interference with the NH₃ measurement.

The FTIR spectra were recorded with a Nicolet Magna 750 instrument with a resolution of 4 cm⁻¹ using pressed disks of pure powders (about 20 mg × 1 cm²), activated by outgassing under high vacuum (10⁻⁴ Torr) at 773 K for 1 h in the IR cell. A conventional gas manipulation/outgassing ramp connected to the IR cell was used. The adsorption procedure involves a short contact (2 min) of the activated sample disk with acetonitrile vapours at room temperature and following outgassing in steps of 10 min at room temperature and increasing temperatures. Acetonitrile was purchased from Aldrich.

6 Catalytic tests

The epoxidation catalytic tests were carried out in a batch reactor: 600 mg of the catalyst, 30 cm³ of methanol as solvent and 40 mmol of cyclooctene were loaded and the mixture was heated up to 343 K under vigorous stirring. At that temperature, 40 mmol of hydrogen peroxide (35 wt.% aqueous solution, Fluka) were added in one pot. Samples were withdrawn at different reaction times and cooled at room temperature by quenching them in cold water. Then, the organic phase of the reaction mixtures was rapidly analysed by gas chromatography (HP 5890) using a capillary column (Chrompack CP Wax; 100% polyethyleneglycol; 30 m × 0.25 mm i.d.; film thickness: 0.25 μm) and a FID detector. Residual H₂O₂ was determined by iodometric titration.

CHAPTER 3

The $\text{Li}_2\text{O}\cdot\text{Nb}_2\text{O}_5\cdot\text{SiO}_2$ Ternary System:

Experimental

1 Synthesis

Lithium-niobium-silicon mixed-oxides nanocomposites, whose nominal molar composition can be expressed by the formula $(\text{Li}_2\text{O})_x\cdot(\text{Nb}_2\text{O}_5)_x\cdot(\text{SiO}_2)_{100-2x}$ with $x = 5$ (*5LN*), 10 (*10LN*), 15 (*15LN*), 30 (*30LN*) were obtained by a suitable modification of the sol-gel route previously described to synthesize gels in the $\text{Nb}_2\text{O}_5\cdot\text{SiO}_2$ binary system.

Lithium nitrate, LiNO_3 (99%, Gelest), niobium chloride, NbCl_5 (99%, Gelest) and tetraethoxysilane, $\text{Si}(\text{OC}_2\text{H}_5)_4$ (TEOS) (99%, Gelest), were used as starting materials. As the ultimate aim was to obtain LiNbO_3 nanocrystals in the silica matrix, the Li/Nb ratio was kept equal to one in all gel compositions according to the stoichiometric Li/Nb ratio in LiNbO_3 .

The materials were synthesized in form of bulk, flakes and thin films: their molar compositions are summarized in Table 3.1.

Table 3.1 Gels composition mol%.

Sample	Li ₂ O	Nb ₂ O ₅	SiO ₂
Bulk <i>B-5LN</i>	5	5	90
Bulk <i>B-10LN</i>	10	10	80
Flakes <i>F-10LN</i>	10	10	80
Flakes <i>F-15LN</i>	15	15	70
Thin Film <i>TF-10LN</i>	10	10	80

1.1 Bulk and flakes

Bulk gels with composition 5Li₂O·5Nb₂O₅·90SiO₂ (*B-5LN*) and 10Li₂O·10Nb₂O₅·80SiO₂ (*B-10LN*) were prepared according to the procedure showed in the flow-chart (see Figure 3.1).

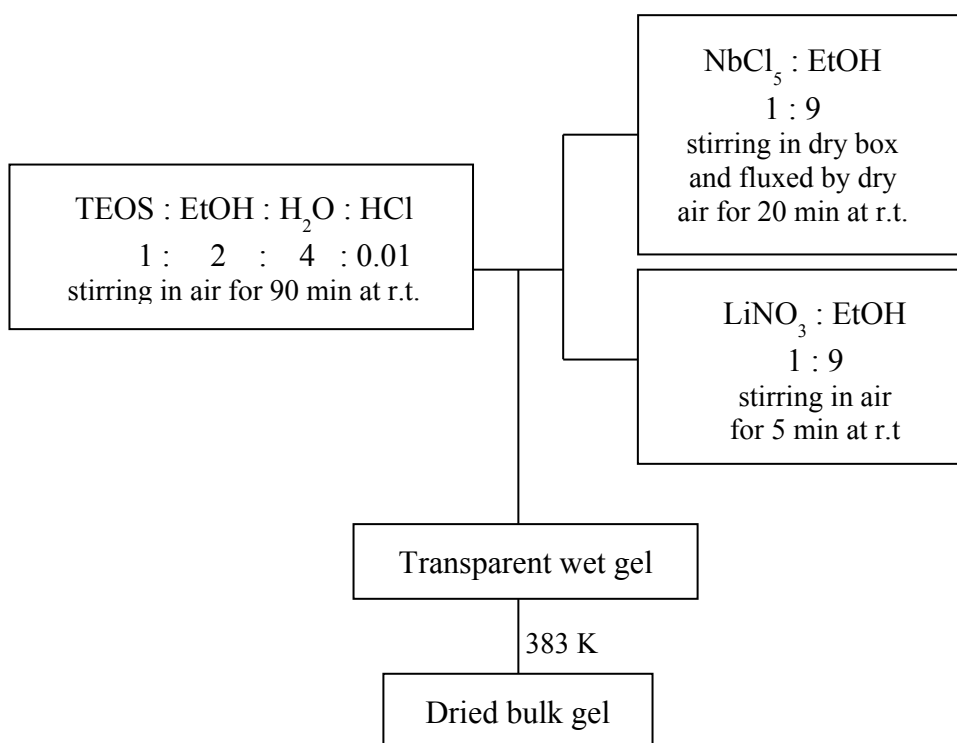


Fig. 3.1 Flow-chart of the bulk gels synthesis procedure showing the molar ratios employed.

A solution of NbCl_5 in anhydrous ethanol, EtOH, having a molar ratio $\text{NbCl}_5 : \text{EtOH} = 1 : 9$, was prepared in a dry box at room temperature. This solution was fluxed by dry-air for 20 min to allow the HCl removal. Simultaneously, a solution of LiNO_3 in EtOH ($\text{LiNO}_3 : \text{EtOH} = 1 : 9$) was prepared and after complete dissolution of LiNO_3 , was mixed to the first one. The resulting solution was mixed with a solution of TEOS, EtOH, H_2O and HCl (TEOS: EtOH : H_2O : HCl = 1 : 2 : 4 : 0.01) previously stirred for 1 h at room temperature using hydrochloric acid as catalyst. From this final solution transparent and homogeneous gels were obtained after a few hours. The gels were kept for 2 days at room temperature and then dried in air at 383 K in an electric oven for 3 days, yielding yellow and transparent bulk samples for each composition. These samples were finely ground before the subsequent heat-treatments in air.

As intermediate step, to approach the films preparation a synthesis procedure was set to obtain transparent flakes with thickness less than 0.5 mm. At this stage flakes with composition $10\text{Li}_2\text{O}\cdot 10\text{Nb}_2\text{O}_5\cdot 80\text{SiO}_2$ (*F-10LN*) and $15\text{Li}_2\text{O}\cdot 15\text{Nb}_2\text{O}_5\cdot 70\text{SiO}_2$ (*F-15LN*) were prepared according to the procedure showed in the flow-chart (see Figure 3.2). The synthesis route was the same as for the bulk gel except for the EtOH amount, that was doubled in each step, to slow down the gelation process. The final solutions were stirred at room temperature for 2 days and then poured into a Petri dish. After 2 days, transparent flakes were obtained that were left at room temperature for 2 days more and then dried at 383 K for 1 day in an electric oven.

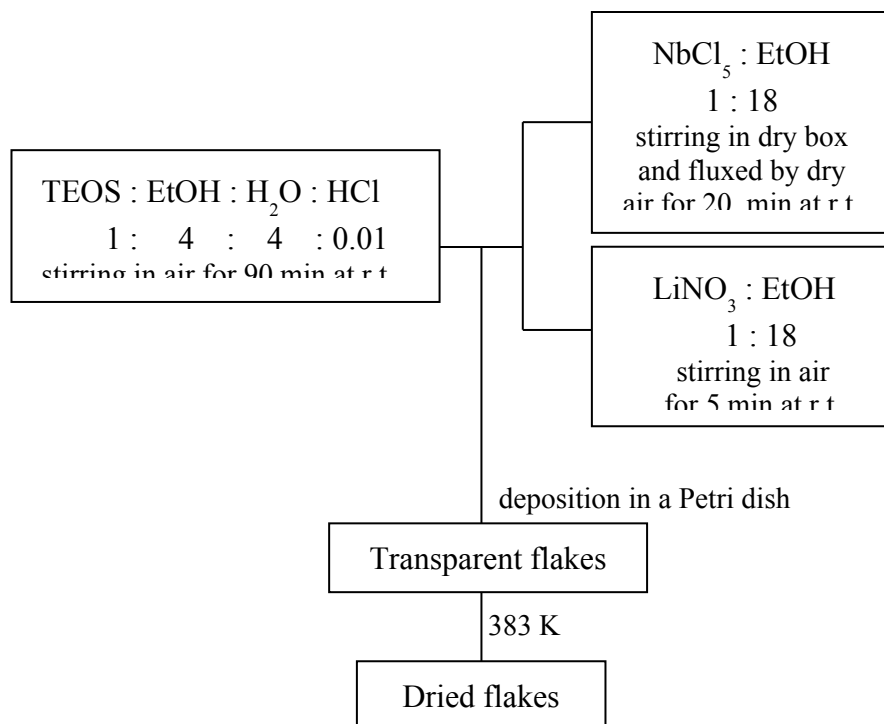


Fig. 3.2 Flow-chart of the flakes synthesis procedure showing the molar ratios employed.

1.2 Thin Films

Thin films with composition $10\text{Li}_2\text{O}\cdot 10\text{Nb}_2\text{O}_5\cdot 80\text{SiO}_2$ (*TF-10LN*) were prepared according to the procedure showed in the flow-chart (see Figure 3.3).

The preparation procedure of films started from more diluted precursor solutions compared with the flakes one.

A solution of NbCl_5 in anhydrous ethanol having a molar ratio $\text{NbCl}_5 : \text{EtOH} = 1 : 20$ was prepared in a dry box at room temperature. This solution was fluxed by dry-air for 20 min to allow the HCl removal. Simultaneously, a solution of LiNO_3 in anhydrous ethanol (EtOH) having a molar ratio $\text{LiNO}_3 : \text{EtOH} = 1 : 20$ was prepared and after complete dissolution of LiNO_3 , was mixed to the first one. The resulting homogeneous solution was mixed with a solution of anhydrous EtOH,

TEOS and H₂O previously stirred for 1 h at room temperature using hydrochloric acid as catalyst and whose molar ratio was TEOS : EtOH : H₂O : HCl = 1 : 4 : 4 : 0.01.

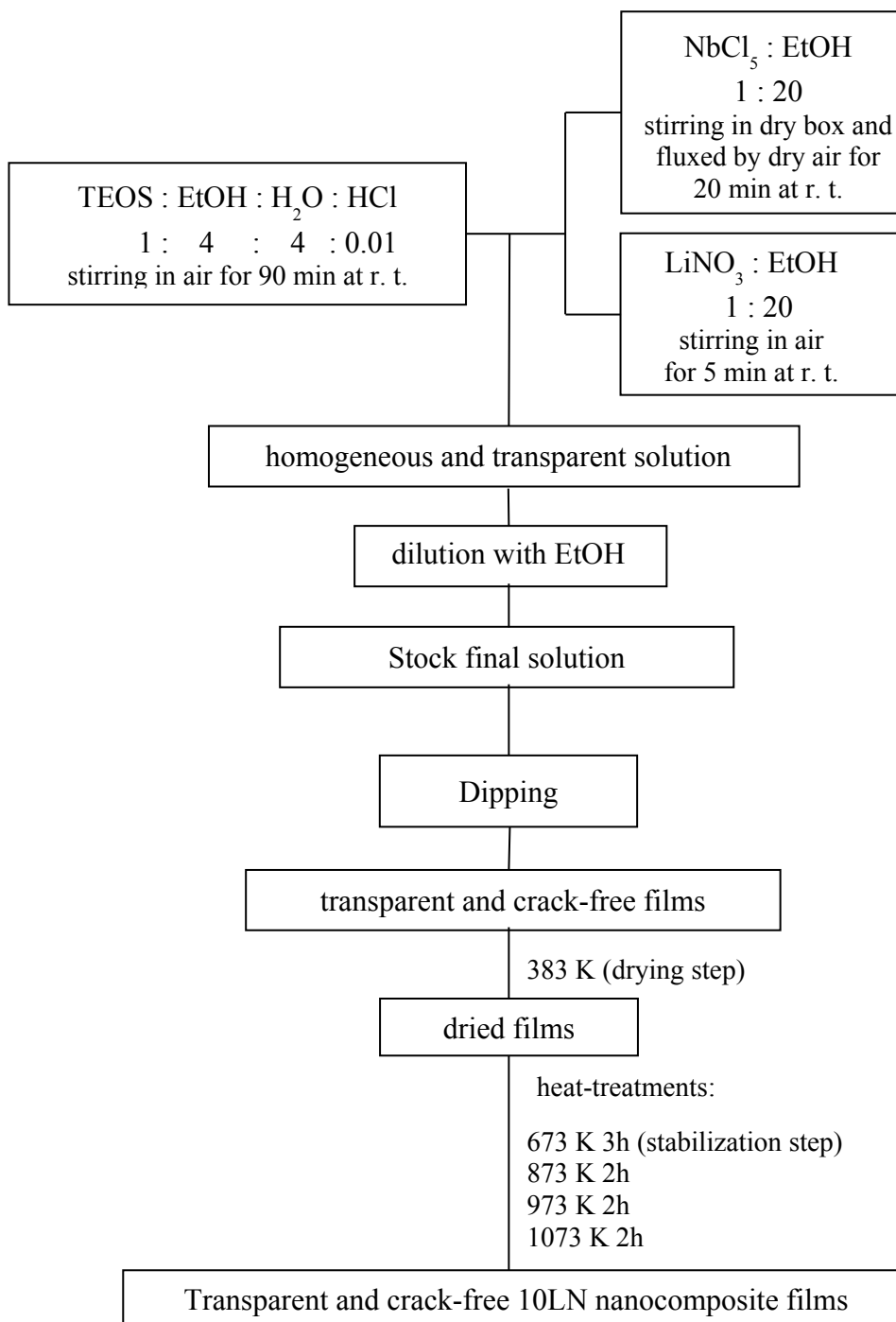


Fig. 3.3 Flow-chart of the films synthesis procedure showing the molar ratios employed.

The resulting clear solution was further diluted by adding EtOH to have a 50% increase of the volume, and stirred for 1 day at room temperature. Such amount of ethanol is required to form the stock solution for films preparation whose viscosity was roughly monitored by viscosimetric test blade.

From this final solution thin films were obtained by dip-coating at room temperature using the dip-coater KSV model illustrated in Figure 3.4.

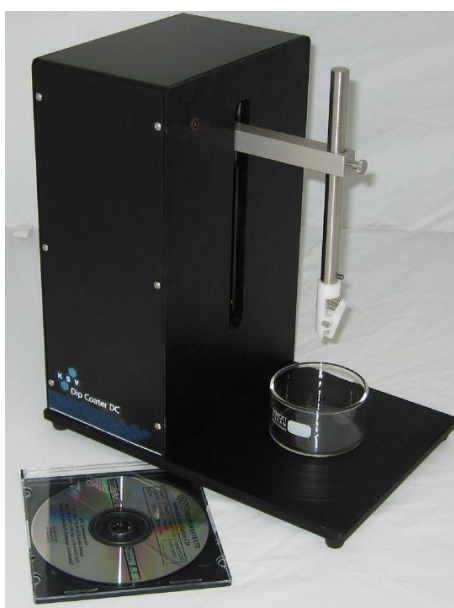


Fig. 3.4 Dip-coater for films deposition.

The deposition was carried out on two types of substrates:

- 10 x 10 mm² Si-SiO₂
- 10 x 10 mm² Al₂O₃ R-plane (CrysTec GmbH)

To find the optimal deposition parameters, different withdrawal speeds of the substrates and deposition times were tested. As regard the films deposited on Si-SiO₂ substrates the withdrawal speed was fixed at 25 cm min⁻¹ and the deposition time at 20 s. Instead, for the films deposited on Al₂O₃ substrates the withdrawal

speed was fixed at 85 cm min^{-1} and the deposition time at 60 s. Transparent and crack-free films were obtained that were transferred into an electric oven and heated in air, first at 383 K for 1 h (drying step), and then at 673 K for 3 h to allow the evacuation of solvent and residual organic molecules (stabilization step). The stabilized films deposited on Si-SiO₂ substrates were annealed in air for 2 h at 1073 K. Instead, the stabilized films deposited on Al₂O₃ substrates were annealed in air for 2 hours at 873, 973 and 1073 K. Transparent, homogeneous and crack-free films were obtained both on the Si-SiO₂ and Al₂O₃ substrates after these heat-treatments.

2 Bulk and flakes characterization

2.1 Thermal analysis

The weight loss of the bulk samples as well as the nature and temperatures of the various reactions occurring during the heating were evaluated by a Netzsch simultaneous thermoanalyser STA 409 PC with Al₂O₃ as reference material and equipped with Al₂O₃ sample holders. The TG/DTA curves, recorded in air from room temperature up to 1273 K at heating rate of 10 K min^{-1} , were carried out on 50 mg of the dried bulk gels.

Regard to the flakes the thermal analysis was carried out by DTA using a high temperature DTA unit (Netzsch, DSC 404 model) with Al₂O₃ as reference material. The DTA curves, recorded in air from room temperature up to 1273 K at a heating rate of 10 K min^{-1} , were carried out on about 30 mg of dried flake gels.

2.2 X-Ray Diffraction

The amorphous nature of the dried gels as well as the nature of the crystallizing phases formed at higher temperature, were ascertained by XRD. Samples, finely ground and heated at different temperature in the range 823–1073 K were measured. The spectra were collected by a Philips diffractometer model PW1710 (Cu K α , $\lambda=1.5418$ Å), at a scan rate of 1° min⁻¹.

3 Thin films characterization

3.1 Thickness and roughness

The thickness and roughness of the heat-treated films were measured by a TENCOR profilometer; the obtained results represent an average value of three measurements. The roughness of the films deposited on Al₂O₃ substrates was also measured by AFM (JEOL JSPM 4210).

3.2 Atomic Force Microscopy

The morphological features of the heat-treated films were studied by AFM. AFM images were acquired in non contact mode by means of the JEOL JSPM 4210 system and elaborated by means of the WSxM software [92].

3.3 X-Ray Diffraction

The amorphous nature of the thin films as well as the nature of the crystallizing phases were ascertained by XRD. Measurements were performed on the heat-treated thin films deposited on Si-SiO₂ substrates by a Rigaku D-Max B diffractometer using the Bragg-Brentano configuration (Cu K α , $\lambda=1.5418$ Å), at a scan rate of 1° min⁻¹.

To obtain higher sensitivity to the film structure, for thin films deposited on Al_2O_3 substrates measurements were also performed by a Bruker D8 Advance diffractometer ($\text{Cu K}\alpha$) using the glancing incidence configuration. GIXRD measurements were collected at an incidence angle of 1.0° .

3.4 dc current-voltage measurements

The electrical properties of thin films were studied by a standard two probe technique. On each sample, six couples of electrical contacts have been obtained by sputtering in plane silver contacts on the surface of the heat-treated films, obtaining conducting channels with length $L=100 \mu\text{m}$ and width $w=5 \text{ mm}$, as illustrated in Figure 3.5.

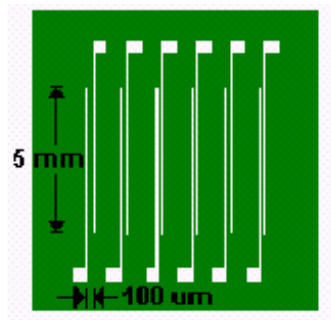


Fig. 3.5 Electrical silver contacts.

The advantage of planar arrangement of electrodes is to avoid the effects of the diffusion of the material of the electrodes into the sample. Indeed, in the case of cross contacts such a diffusion can create a percolative path of the current between the top and bottom contacts with different electrical properties with respect to the intrinsic behaviour of the composite under study.

The homogeneity of electrical properties has been verified by testing different pairs of electrodes.

The dc I-V characteristics were measured by a picoAmmeter (Keithley 487) illustrated in Figure 3.6, with the bottom electrode connected to the ground, and recorded by scanning the applied voltage in a loop (from 0 to $+V_{max}$, from $+V_{max}$ to $-V_{max}$, and from $-V_{max}$ to 0, in sequence).



Fig. 3.6 Probe station.

An applied voltage of 500 Volts correspond to an electrical field of $5 \times 10^4 \text{ Vcm}^{-1}$ which is similar to electrical field already reported in sandwiched structures. Consistently, instead of the measured current I , the current density J is plotted.

It should be noted that for each stage of the heat-treatments both the AFM and the GIXRD characterization have been performed on the films previously subjected to the electrical measurements.

CHAPTER 4

The Nb₂O₅·SiO₂ Binary System:

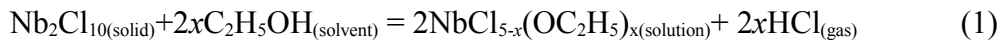
Results and Discussion

New nanocomposite catalysts based on niobium-silicon mixed-oxides were obtained at room temperature by a new sol-gel route. A wide compositional range was explored in order to prepare a tailored catalyst with a high niobium dispersion in the silica matrix. To relate the catalytic performances with the structural properties of the gel derived samples their evolution with the temperature was evaluated. Successively, the textural and the surface acidic properties were determined and the catalytic activity in the cyclooctene epoxidation with H₂O₂ was tested, as well.

1 Synthesis

The synthesis procedure adopted in this work was addressed to obtain chemical gels with a high dispersion of niobium into the siloxane network. In view of this, some innovations were introduced in the procedure with respect to the ones reported in literature [11–15, 19], the foremost of which are the lack of the TEOS prehydrolysis and the sequence of the precursors mixing. Usually, the TEOS prehydrolysis is required to compensate its lower reactivity toward water

with respect to the one of the metallic alkoxide [93]. In this case NbCl₅ was used as niobium precursor. This solid is formed by Nb₂Cl₁₀ dimeric molecules in which the niobium is surrounded by a distorted octahedron of chlorine atoms, two of which are bridging [94]. Its moisture-sensitivity was controlled by dissolving it in absolute ethanol according to following equation:



The degree of conversion of the above reaction can be controlled by the HCl stripping with dry air bubbling. Consequently, partially, NbCl_{5-x}(OC₂H₅)_x, or completely, Nb(OC₂H₅)₅, substituted species are formed. A stripping time of 20 min was used both to avoid the complete substitution and to preserve to some extent unreacted molecules of Nb₂Cl₁₀ in solution. These molecules play a key role in the stabilization of the niobium ions in aqueous solution toward the precipitation of Nb₂O₅·*n*H₂O. Actually, NbOCl₅²⁻ and NbCl₆⁻ complexes were found in aqueous saturated HCl solution of niobium pentachloride [95], while Nb(OH)₂Cl₄⁻ and Nb(OH)₂Cl₃ were detected in more diluted solutions (11–13.4 M HCl and ~3 M HCl, respectively) [96]. Therefore, when this solution was firstly combined with TEOS alcoholic and then with HCl hydroalcoholic solutions, the precipitation of Nb₂O₅·*n*H₂O did not occur as consequence of the formation of niobium complexes as well as of a suitable water content. Into the final solution there are several species that can be hydrolyzed: oxo-hydroxo-chloro complexes, NbCl_{5-x}(OC₂H₅)_x, Nb(OC₂H₅)₅, and TEOS. Among them, TEOS should result the less reactive species, as the silicon exhibits the lower positive partial charge [93].

Consequently, the hydrolysis of niobium chloro-ethoxide species starts forming niobium hydroxo and oxo soluble oligomers. Then, the TEOS hydrolysis begins to occur at a valuable rate producing both self- and cross-condensation hindering the further self-condensation of niobium oxo-oligomers. This is enabled by the double role played both by the alkoxide-niobium species [12] and by the water. In fact, the former species act both as cross-linking reagents and as catalyst for the condensation reactions of siloxane oligomers, while the water molecules act both as reagent and as product in the hydrolysis and condensation equilibria, respectively. Therefore, in this case, the lack of TEOS prehydrolysis makes the formation of homogeneous sols easier as the presence of siloxane oligomers originated during the prehydrolysis could hinder the redistribution of hydrolyzed species favouring self-condensation reactions. The above hypothesis regarding the gelation mechanism is supported by a recent ^{17}O NMR study [97] on the hydrolysis and condensation kinetics occurring in hydroalcoholic solutions of diethoxydimethylsilane and niobium ethoxide. It was found that resonances related both to niobium oxo-oligomers and to niobium-silicon cross-condensed species begin to appear from the start of the hydrolysis. Increasing the hydrolysis time, the relative intensity of these resonances changes increasing the ones related to the Nb–O–Nb bonds to the detriment of Nb–O–Si species. Simultaneously, the intensity of the resonance related to siloxane rings diminishes in favour of the resonance related to siloxane chain, indicating that increasing the hydrolysis time a redistribution of the above species in the sol occurs, favouring the formation both of niobium oxo-oligomers and of the siloxane chains [97]. It is noteworthy that these authors [12, 97] have obtained gelation by means of slow solvents

evaporation under intermittent vacuuming at 308 K while Francisco and Gushikem [13] at 333 K as well. On the other, Somma et al. [21] have prepared niobium-based aerogels in different type of matrices (SiO_2 , Al_2O_3 , ZrO_2) under acidic and basic conditions. Although the synthesis procedure used by these authors exhibits some similarities with the one adopted in this work (the lack of the TEOS prehydrolysis and the same sequence of the precursors mixing) in the Si-containing samples prepared under acidic conditions no gelation was observed [21]. On the contrary, in this work yellow and transparent chemical gels have been obtained at room temperature for each studied composition (as previously displayed in Figure 2.2b).

2 Chemical analysis

The chemical analysis for the determination of the actual niobium and silicon contents was performed on the samples annealed at 873 K for 1 h.

A characteristic absorbance spectrum collected in the range 250–500 nm was reported in Figure 4.1: the niobium maximum absorbance signal is located at $\lambda=342$ nm.

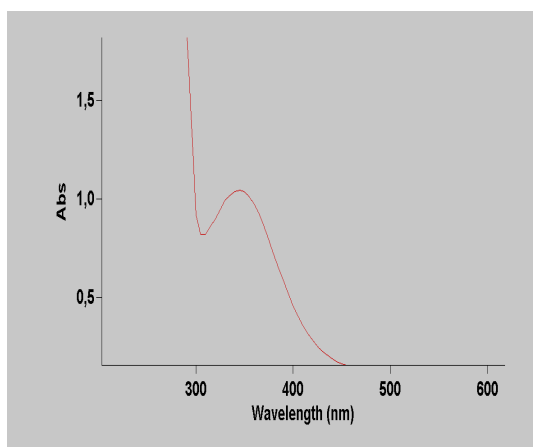


Fig. 4.1 Niobium absorbance spectrum.

The results of the chemical analysis were reported in Table 4.1.

Table 4.1 Chemical analysis of niobium and silicon.

Sample	Nominal composition (mol %)		Actual composition (mol %)	
	Nb ₂ O ₅	SiO ₂	Nb ₂ O ₅	SiO ₂
<i>2.5Nb</i>	2.5	97.5	2.45 ± 0,1	97.5 ± 0,5
<i>5Nb</i>	5	95	5.08 ± 0,15	94.9 ± 0,4
<i>10Nb</i>	10	90	8.70 ± 0,3	91.3 ± 0,3
<i>20Nb</i>	20	80	20.40 ± 0,5	79.5 ± 0,5

For each sample the actual composition was very close to the nominal one.

Thus, the adopted synthesis procedure has allowed to obtain gel materials without niobium loss.

3 Thermal analysis

The DTA curves of the dried gels recorded in air at 10 K min⁻¹ are shown in Figure 4.2. To facilitate the interpretation of the DTA peaks the corresponding TGA curves, recorded in N₂ at the same heating rate, are also reported in the same Figure. Although the different atmospheres should induce small shifts in the temperature at which the same thermal event occurs, the comparison on the whole temperature range explored keeps its validity. The same total weight loss (about 13 wt %) is given by the TGA curves for all dried gels even if it occurs in a different way depending on the niobium content. For the *2.5Nb*, *5Nb* and *10Nb* the majority of weight loss takes place in two different steps from room temperature to about 470 K and from 500 K to about 640 K. In these ranges poorly separated

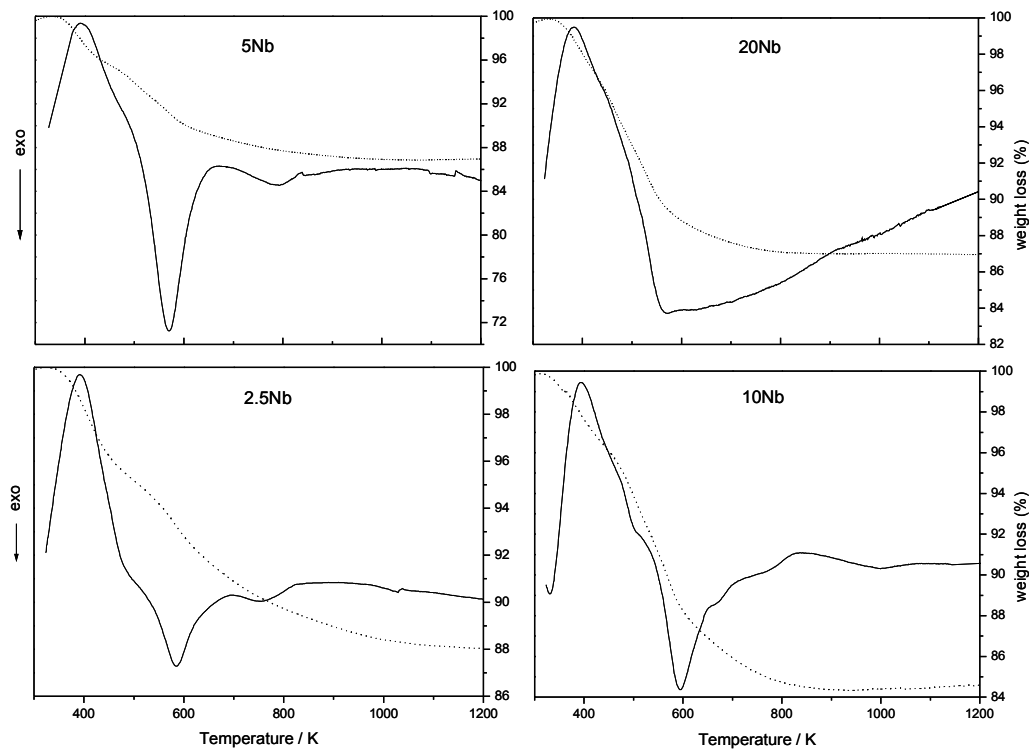


Fig. 4.2 DTA (solid line)-TG (dotted line) curves of the dried gels recorded at 10 K min^{-1} .

thermal effects are seen in the DTA curves: an endothermic peak followed by two exothermic ones. For each sample, the first exothermic peak is stronger than the second one and occurs at different temperatures, 585 K (*2.5Nb*), 570 K (*5Nb*), and 595 K (*10Nb*), while the second exothermic peak is broad and takes place in the same temperature range, at about 770 K (see Figure 4.2). The endothermic peaks can be related to the evaporation, from open pores, of water and alcohol physically trapped in the gels, while the exothermic ones are likely caused by the burning of the pyrolysis products of residual organic groups in the gels [16]. This phenomenon involves molecules that are more or less trapped in the pores of the siloxane matrix and, consequently, it can occur at different stages. In contrast to the other gels, the majority of the weight loss for the 20Nb sample seems to occur

in a single step from room temperature to about 600 K and, in the corresponding DTA curve, a single broad endothermic peak at 383 K is seen. Therefore, for this sample the evaporation of the solvents is followed by evacuation of the pyrolysis products. At temperatures higher than 873 K, no additional peaks are observed in any DTA curves and, concurrently, no weight loss is given by the TGA curves except for the samples at low niobium content for which a very slight drift of the weight loss is seen, indicating that the elimination of organic residues as well as of any volatile species is almost completed at 873 K.

4 Structural characterization

The structural evolution of dried gels upon heat-treatments was studied by powder XRD as well as Raman and FTIR spectroscopy within a range of temperatures being used, starting from the dried gel and including gels heated to 873, 1273, and 1473 K. These temperatures were chosen on the basis of the above thermal analysis data. The lower temperature stands for the minimum value at which it is possible to obtain stable gel-derived samples for all studied compositions. The higher temperature values were selected to force the crystallization of the samples. Each sample was prepared by slow heating at 2 K min^{-1} to the required temperature and then held at this temperature for 1 h followed by quenching. The heat-treated samples hereafter will be referred to as their already specified labels followed by the temperature of the heat-treatment stage (*SiO₂-383*, *2.5Nb-383*, etc).

4.1 X-Ray Diffraction

The XRD patterns of the dried gels and of the heat-treated samples are shown in Figure 4.3.

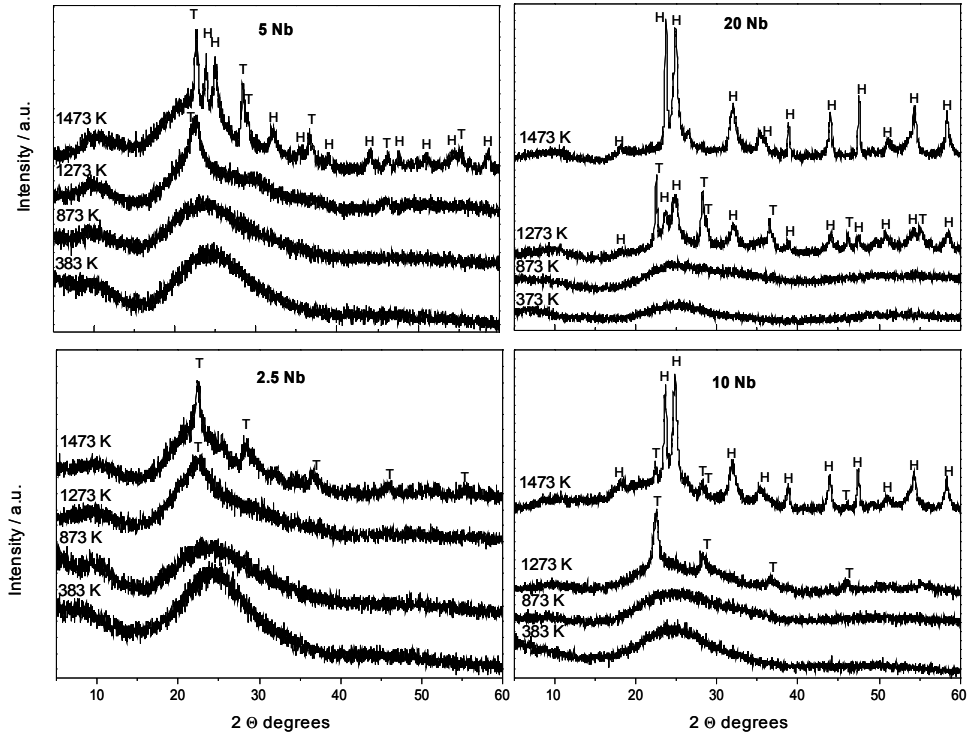


Fig. 4.3 XRD patterns of the heat-treated gel samples. T and H stand for T- Nb_2O_5 and H- Nb_2O_5 phases, respectively.

It should be emphasized that regardless of the niobium content all samples keep their amorphous nature up to 873 K. In fact, the XRD patterns of these samples exhibit a diffuse maximum at about $2\theta = 24^\circ$ typical of the amorphous silica (Figure 4.3) [98, 99]. On the contrary, in the subsequent heating step (1273 K) crystallization phenomena are seen, the extent of which depends on the niobium amount (Figure 4.3). For the *2.5Nb-1273* and *5Nb-1273* coherent scattering regions arising from the amorphous background start to appear giving a single broad maximum centred at $2\theta = 22.4^\circ$ that corresponds to the highest peak of the

T-Nb₂O₅ phase (JCPDS card 27–1312). The shape of these diffraction peaks points out the precipitation in the amorphous matrix of extremely small crystallites [100]. The crystallites size was roughly estimated using the Scherrer formula. For a crystal with dimension “ D_{hkl} ” perpendicular to the diffractive planes, the Scherrer equation is satisfied for the angular width of the diffraction peak:

$$\Delta(2\theta) = \frac{0.94\lambda}{D_{hkl} \cos \theta}$$

where

$\Delta(2\theta)$ = Full Width at Half Maximum (FWHM) in radiant

λ = wavelength of the X-ray (Cu K α = 1.542Å)

θ = angular position of the diffraction peak.

For both samples the mean size resulted less than 5 nm. At this stage, in the 10Nb-1273 XRD pattern a few broad and low intensity peaks are seen, which are assigned to the T-Nb₂O₅ phase while peaks of both T- and H-Nb₂O₅ (JCPDS card 32–711) phases are observed for the 20Nb-1273. At the highest heat-treatment temperature (1473 K) the dependence of the crystallization ability on the niobium pentoxide content results enhanced. Only well shaped peaks of the H-Nb₂O₅ phase are seen in the 20Nb-1473 XRD pattern whereas broad and low intensity peaks are shown in the 2.5Nb-1473 XRD pattern that are related to the sole T-Nb₂O₅ phase. On the contrary, both T- and H-Nb₂O₅ phases are detected for the 10Nb-1473 and 5Nb-1473. In the former H-Nb₂O₅ is the main phase, in the latter just the opposite occurs (Figure 4.3).

The above results strongly support the hypothesis that the niobium pentoxide is dispersed in the siloxane framework on the atomic scale. Actually, it is known that the amorphous niobium pentoxide exhibits a complex crystallization behaviour upon heating both in the pure state [101] and deposited on a support [13, 102]. In the latter case the crystallization behaviour is strongly affected by the support physico-chemical properties [13, 102]. Particularly, it was shown that the reduced crystallization ability of the niobium pentoxide is due to the nature of the interaction with the support as well as to its strength [13, 102]. Francisco and Gushkem [13] obtained similar XRD results for gel-derived samples synthesized by a different procedure even if remarkable differences are noted. Thus, the heat-treatment for 1 h at 1473 K produces only the growth of T-Nb₂O₅ nanocrystals in the *2.5Nb-1473*, contrary to what shown by Francisco and Gushkem [13] for the corresponding heat-treated sample for which both T- and H-Nb₂O₅ phases are seen. Moreover, T-Nb₂O₅ is the main crystallising phase in the *5Nb-1473* while H-Nb₂O₅ was found by Francisco and Gushkem [13]. The *2.5Nb-1273* and *5Nb-1273* exhibit a lower crystallinity with respect to that previously shown for the corresponding heat-treated samples [13]. Therefore it is possible to infer that the sol-gel procedure tuned in this work allows to obtain a higher dispersion of the niobium pentoxide into the siloxane framework with respect to the one previously reported [13]. This is also supported by the crystallization behavior of the samples at higher niobium content. Actually, the growth of the H-Nb₂O₅ phase starts to occur only after the heat-treatment at 1473 K for the *10Nb*, while in the *20Nb* it occurs at lower temperature. The monoclinic H-phase has a complex structure originating from the existence of superstructures comprising 3×5 and 3×4 ReO₃

type blocks [101], whereas the orthorhombic T-phase is formed by corner- and edge-sharing distorted octahedra and pentagonal bipyramids [101]. Consequently, the formation of a nucleation site of the monoclinic polymorph requires in the local gel network a higher concentration of ordered NbO₆ octahedra than what required by the orthorhombic one. In this case, such a condition is satisfied either at a higher temperature or at higher niobium concentration, indicating that niobium atoms must diffuse further to reach the required local order: this could be due to a more homogeneous dispersion of the niobium pentoxide in the pores of the siloxane network. This view is supported by Raman spectra later on discussed.

4.2 Raman spectroscopy

Raman spectra in the 200–1200 cm⁻¹ energy region of the studied samples at different heat-treatment stages are shown in Figure 4.4. For the stages at 383 and 873 K the spectrum of pure SiO₂ is reported as well. Spectra are reported starting from the richest in Nb (curve a) and finishing with the poorest in Nb samples (curve d) or with pure silica (curve e).

For the stage at 383 K, the spectrum of SiO₂ (curve e) shows bands at 420, 490, 610, 807, 970 and 1095 cm⁻¹. All these bands except the latter are characteristic of the siloxane network [103–109]. The broad band at 420 cm⁻¹ is attributed to symmetric motion of the bridged oxygen atoms in the plane bisecting the Si–O–Si bonds, with little associated silicon displacement [104–109]. This band occurs at lower wavenumbers with respect to what expected for a densified silica framework (430 cm⁻¹), indicating that the xerogel network is formed by SiO₄ groups with larger inter-tetrahedral angles [109].

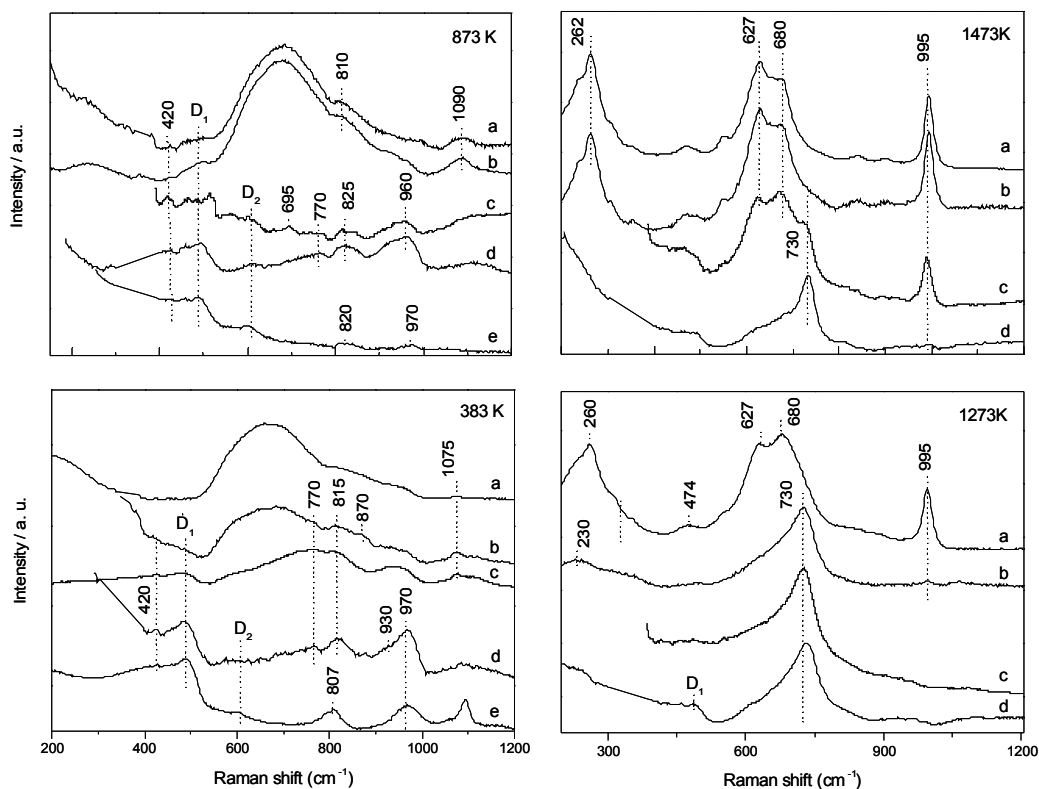


Fig 4.4 Raman spectra of the studied gels heated at different temperature. (a): $(\text{Nb}_2\text{O}_5)_{20}(\text{SiO}_2)_{80}$ (*20Nb*); (b): $(\text{Nb}_2\text{O}_5)_{10}(\text{SiO}_2)_{90}$ (*10Nb*); (c): $(\text{Nb}_2\text{O}_5)_5(\text{SiO}_2)_{95}$ (*5Nb*); (d): $(\text{Nb}_2\text{O}_5)_{2.5}(\text{SiO}_2)_{97.5}$ (*2.5Nb*); (e): SiO_2 .

The bands at 490 and 610 cm^{-1} are called the D_1 and D_2 defect bands and assigned to symmetric stretching modes of Si–O–Si bridges in regular fourfold and planar threefold rings of SiO_4 tetrahedra respectively [103–105]. The former is the highest of the spectrum, as it usually occurs for the SiO_2 dried gel samples stabilized at low temperature [12, 105–107]. The band at 807 cm^{-1} is related to symmetric vibration of two silicon atoms about their bridged oxygen [104, 108]. The band at 970 cm^{-1} , assigned to Si–OH stretching vibrations, [106, 107, 109], denotes the presence of silanol groups in the porous network of SiO_2 dried gel. Finally, the sharp band at 1095 cm^{-1} (Figure 4.4) is related to organic residuals that are still present at this stage of the heat-treatment [107]. In the Nb-containing

dried gels spectra, together with the silica network bands, new bands start to appear and develop, which are associated to Nb–O vibrational modes. These bands tend to mask the siloxane network's ones, because the polarizability of the Nb–O bond is higher than that of the Si–O bond [110] and, consequently, the Raman bands associated to the Nb–O vibrations are expected to be more than one order of magnitude higher [111]. Nevertheless, the Raman bands associated with the Si–O vibrations remain visible in all spectra because the quantity of Si is at least four times that of Nb. In the *2.5Nb-383* spectrum (curve d) a new band appears at 770 cm^{-1} , the band at 807 cm^{-1} is shifted to 815 cm^{-1} and the band at 970 cm^{-1} grows and becomes asymmetric towards the lower wavenumbers, with a feature at about 930 cm^{-1} . In the *5Nb-383* spectrum (curve c), the band at 770 cm^{-1} continues to grow becoming stronger than the one at 815 cm^{-1} and the band at 970 cm^{-1} broadens and shifts towards lower wavenumbers (about 950 cm^{-1}). The change of the shape of this band is due to the overlapped stretching modes of Nb=O terminal double bonds of NbO₄ tetrahedra and NbO₆ distorted octahedral [112, 113] with the Si–OH ones. Moreover, a new band appears at 1075 cm^{-1} (curve c), due to transverse optical Si–O stretching of SiO₄ tetrahedra with all bridging oxygens [104, 107–108]. In the *10Nb-383* spectrum (curve b) two new bands appear, a very strong one centred at 680 cm^{-1} and a weaker one at 870 cm^{-1} . The former band is attributed to the stretching vibration of Nb–O bonds in interconnected NbO₆ octahedra [111–113]. In the *20Nb-383* (curve a) spectrum, the band at 680 cm^{-1} grows further, while the 770 cm^{-1} band disappears. For gel-derived SiO₂·Nb₂O₅ samples with compositions close to the *2.5Nb* and *5Nb* (3 and 7.5 mol% of Nb₂O₅) no evidences of Nb–O–Nb bonds were found by Drake et al.

[11] using ^{17}O solid state NMR. These authors have suggested that niobium is dispersed within the siloxane network on the atomic scale being mainly present as NbO_4 tetrahedra. Considering also that tetrahedrally coordinated niobium oxide reference compounds possess their major Raman bands in the $790\text{--}830\text{ cm}^{-1}$ region [112], the feature at 770 cm^{-1} can be related to the $\text{Nb}\text{--O}(\text{--Si})$ stretching vibrations of NbO_4 tetrahedra highly dispersed in the siloxane framework. On the other hand, the feature at 915 cm^{-1} can be related to vibrations of the corresponding $\text{Nb}=\text{O}$ bonds [112, 113].

The bands at 815 cm^{-1} and 870 cm^{-1} can be related to the $\text{Nb}\text{--O}$ stretching modes of distorted NbO_6 octahedra sharing a corner with a SiO_4 tetrahedra [73, 111, 112]. Particularly, they can be related to the $\text{Nb}\text{--O}(\text{--Nb})$ and $\text{Nb}\text{--O}(\text{--Si})$, respectively.

In summary, the above results show that the structure of dried gels is strongly influenced by the niobium loading. Actually, the niobium is dispersed within the siloxane network mainly as NbO_4 tetrahedra (band at 770 cm^{-1}) in the *2.5Nb-383* and *5Nb-383*. The presence of NbO_6 octahedra cannot be ruled out for these samples considering that in the $800\text{--}870\text{ cm}^{-1}$ range the vibration modes of $\text{Si}\text{--O}\text{--Si}$ bonds are overlapped with the $\text{Nb}\text{--O}(\text{--Si})$ ones of distorted NbO_6 octahedra [73, 111, 112]. As the Nb content increases, NbO_6 octahedra start to appear (bands at 815 , 870 and 950 cm^{-1}) and cluster (band at 680 cm^{-1}), while the tetrahedra disappear.

It is worth noting that the Raman spectrum of *20Nb-383* (curve a) differs from that reported by Julia'n et al. [12] for the same nominal composition that was mainly characterized by Raman bands due to siloxane network as well as to

residual organics. These differences can be related both to the lower temperature used to stabilize the dried gels (308 K) and to the different synthesis procedure [12]. The structural differences of the dried gels with the niobium loading result enhanced in the subsequent stage of heat-treatment.

For the stage at 873 K, in the Raman spectrum of SiO₂ (curve e) a drastic lowering of the relative intensity of the band at 970 cm⁻¹ with respect to the SiO₂-383 is noted. This result, together with the opposite trend seen for the D₂ peak, shows that the structural evolution with the temperature of the siloxane network takes places according to the characteristic densification mechanism of silica xerogels: polycondensation of silanol groups with predominant formation of three-membered SiO₄ rings [103, 105, 109]. This process involves, for the 2.5Nb-873 (curve d) and 5Nb-873 (curve c), a rearrangement of the distribution of NbO₄ tetrahedra in the siloxane framework favouring a change in the niobium coordination with the initial formation of isolated and/or highly distorted NbO₆ octahedra. In the 5Nb-873 the extent of this conversion appears more heightened as the features in the 600–700 cm⁻¹ range attest. On the contrary, for 10Nb-873 (curve b) and 20Nb-873 (curve a) the NbO₆ clustering results enhanced with the formation of niobia phase separated nanodomains in the silica matrix. In fact both spectra are still characterized by the large and high intensity Raman band in the 500–800 cm⁻¹ range that at this stage exhibits only one evident shoulder at 810 cm⁻¹ with low intensity feature in the 910–990 cm⁻¹ range. Finally, a well-shaped peak at 1090 cm⁻¹ is seen. This peak lies outside the region where the Nb–O vibrations of NbO₆ octahedra are Raman active, independently from the extent of the octahedra distortion [73, 111, 114]. On the other hand, in this region for the

full polymerized SiO_4 tetrahedra weak Raman bands at 1060 and 1200 cm^{-1} should be seen [104, 108]. Therefore, the band at 1090 cm^{-1} can be related to the stretch of Si–O bonds of SiO_4 tetrahedra coordinated with Nb^{5+} ions [108, 115].

The Raman spectra of the samples heated for 1 h at 1273 K show that the niobia crystallization starts to occur to some extent at this stage according to the niobium loading, coherently with the above XRD data. The spectra of *2.5Nb-1273* (curve d) and *5Nb-1273* (curve c) appear still similar at this stage showing a strong Raman band at about 730 cm^{-1} besides the D_1 peak. The position of the former band as well as its shape attest that an early nanocrystallization of the T- Nb_2O_5 phase takes place in the siloxane matrix of these samples [13]. The crystallization extent of the T- Nb_2O_5 phase appears more advanced in the spectrum of *10Nb-1273* (curve b) where a Raman band at 230 cm^{-1} , besides the strong band at 730 cm^{-1} , is seen. Moreover a weak Raman feature at 995 cm^{-1} is detected in this spectrum that can be related to the symmetric stretching modes of the Nb=O terminal bonds of NbO_6 octahedra belonging to the H- Nb_2O_5 structure [112, 114]. The lack of diffraction peaks ascribable to this phase in the corresponding XRD pattern (Figure 4.3) shows that for this sample the regions of coherent scattering of this phase are not still formed at this stage, while on the short range scale a local order starts to appear. All the Raman peaks seen in the spectrum of *20Nb-1273* (curve a) are related to the H- Nb_2O_5 phase [13, 112, 114].

The further stage of heat-treatment (1 h at 1473 K) forces the crystallization of the H- Nb_2O_5 phase in all samples except for the *2.5Nb-1473* (curve d) for which the crystallization of the sole T- Nb_2O_5 phase is still observed. In fact, the Raman spectra of the *10Nb-1473* (curve b) and *20Nb-1473* (curve a)

correspond to that of a H-Nb₂O₅ phase, confirming that the crystallization of this phase is the most important phenomenon at this stage for these samples. On the contrary, in the Raman spectrum of *5Nb-1473* (curve c) the band of the T-Nb₂O₅ phase (about 730 cm⁻¹) is still clearly visible with the strongest ones of the H-Nb₂O₅ phase (623, 671 and 990 cm⁻¹) that appear slightly shifted with respect to the expected values, indicating that the transition from T-Nb₂O₅ to H-Nb₂O₅ phase starts to occur.

4.3 Fourier Transform Infrared spectroscopy

FTIR spectra of dried gels and heat-treated samples are shown in Figure 4.5 where for the stages at 383 and 873 K the spectra of pure SiO₂ are also reported. As expected [110, 111], the analysis of these data will give detailed information about the siloxane backbone structure and the hydroxyl groups distribution, as well.

The spectrum of SiO₂ dried gel (curve e) shows the main envelope in the 1000–1300 cm⁻¹ region, where some of the vibration modes of partially hydrolyzed TEOS molecules (1168 and 1082 cm⁻¹) [116] overlap with the ones typical of a siloxane network (1080 and 1250 cm⁻¹) [117, 118]. Absorption bands at about 450 cm⁻¹ ($\delta_{\text{Si-O-Si}}$) [116], 795 cm⁻¹ ($\nu_{\text{s Si-O-Si}}$) [116], and 1640 cm⁻¹ (deformation modes of O–H bonds and of molecularly adsorbed water, $\delta_{\text{O-H}}$) [16, 119] are also seen. Moreover, this spectrum shows a broad absorption band in the 2800–3800 cm⁻¹ range with a maximum at about 3450 cm⁻¹ and two shoulders at about 3240 and

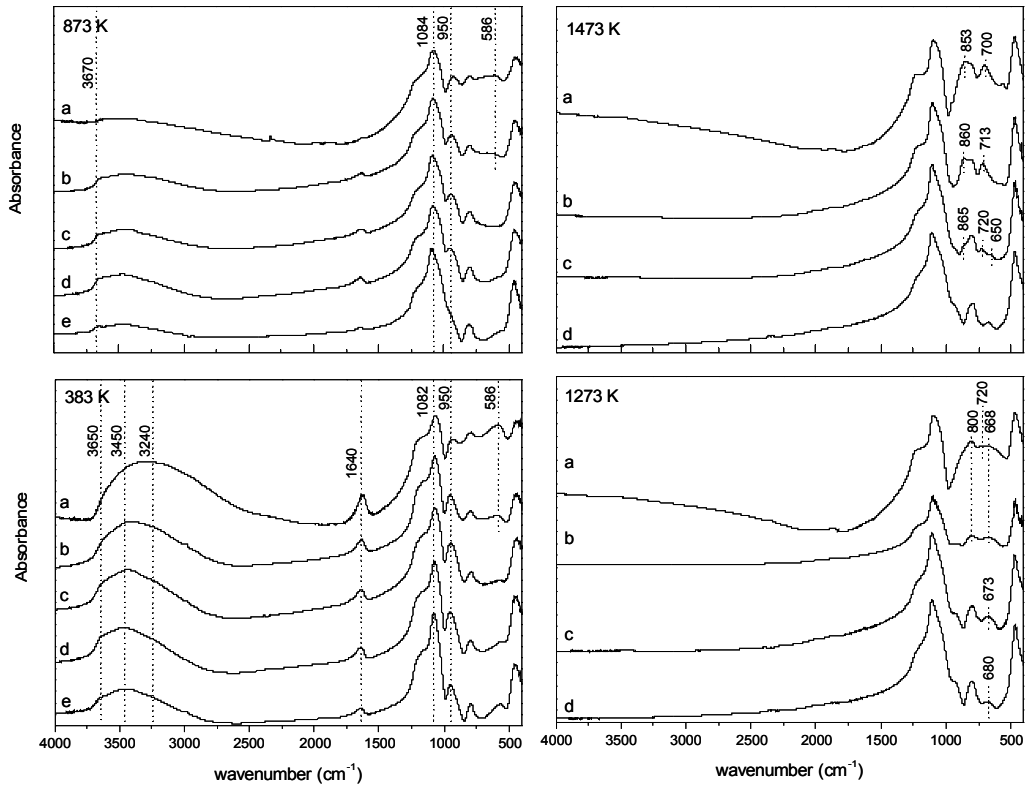


Fig. 4.5 FTIR spectra of the studied gels heated at different temperature. (a): $(\text{Nb}_2\text{O}_5)_{20}(\text{SiO}_2)_{80}$ (*20Nb*); (b): $(\text{Nb}_2\text{O}_5)_{10}(\text{SiO}_2)_{90}$ (*10Nb*); (c): $(\text{Nb}_2\text{O}_5)_5(\text{SiO}_2)_{95}$ (*5Nb*); (d): $(\text{Nb}_2\text{O}_5)_{2.5}(\text{SiO}_2)_{97.5}$ (*2.5Nb*); (e): SiO_2 .

3650 cm^{-1} . This broad band arises from O–H stretches ($\nu_{\text{O-H}}$) involved in hydrogen bonding, while the shoulders at 3650 and 3200 cm^{-1} are related to free and strongly H-bonded OH groups, respectively [16, 116, 119]. In fact, the hydrogen bonding causes low-frequency shifts, whose magnitude is related to the strength of hydrogen bonds in which the OH groups are involved [16, 119, 120]. Finally, the feature at 2990 cm^{-1} can be assigned to the stretching mode of C–H bond in an aldehydic group [16]. In the *SiO₂-383* FTIR spectrum two additional absorption bands at 950 and 570 cm^{-1} are seen as well (curve e). These bands are related to stretching and bending modes of the same bond, Si–OH, $\nu_{\text{Si-OH}}$ and $\delta_{\text{Si-OH}}$ respectively. It is worthy to note that the assignment of the band at 950 cm^{-1} is a

controversial point because it was related to Si–OH and/or Si–O[−] stretching vibrations [12, 13, 16, 43, 102, 116, 120–122]. The formation of Si–O[−] groups appears to us reasonable only in materials containing modifier and/or intermediate glass network oxides; in gel-derived materials containing only glass forming oxides this contribution must be considered not possible.

The FTIR spectra of the niobium containing dried gels exhibit some differences with respect to the *SiO₂-383* one depending on the niobium amount. The highest absorption band gradually shifts toward lower frequencies going from 1082 cm^{−1} (*SiO₂-383*) to 1066 cm^{−1} (*20Nb-383*) suggesting that the $\nu_{as\ Si-O-Si}$ is progressively influenced by the presence of niobium [43]. For the OH related bands, ν_{O-H} , δ_{O-H} and ν_{Si-OH} , similar trends are seen, even if the extent of these shifts are small going from *2.5Nb-383* (curve d) to *5Nb-383* (curve c), while they become larger going from *10Nb-383* (curve b) to *20Nb-383* (curve a), reaching the values of about 150 cm^{−1}, 16 cm^{−1} and 13 cm^{−1}, respectively (Figure 4.5). The last shift, relative to the band at 950 cm^{−1}, shows that the Si–O[−](–Nb) bonds give a predominant contribution to this band in the *20Nb-383* confirming the existence of the silica-niobia interface. On the other hand, differently from what occurs for the other dried gels, in the *20Nb-383* FTIR spectrum the ν_{O-H} band does not show any shoulder, suggesting the presence of one kind of OH group, probably a silanol involved in very strong H bonding. This can be due either to the proximity of silanols in a similar environment or to the existence of a stronger interaction, such as it should occur between silanols and Nb=O groups. In both cases the existence of niobia- and silica-rich nanodomains is required. This description of the *20Nb-383* microstructure is also strengthened by the absorption band at 586 cm^{−1} that is

related to the bridging Nb–O–Nb stretches [113, 123]. In fact, the presence of this band, that at this stage is the only one exclusively related to Nb–O vibrations, can be considered as indicative of the existence of niobia nanodomains. Such a band is still well evident in the *10Nb-383* spectrum but it does not appear in the spectra of the other dried gels, that in this wavenumbers region exhibit bands at 575 cm^{-1} (*5Nb-383*) and 570 cm^{-1} (*2.5Nb-383*) due to $\delta_{\text{Si-OH}}$ and/or $\delta_{\text{Si-O}^-}$. In summary, in accordance with Raman analysis, the above data confirm that niobium is uniformly distributed into the siloxane framework of the *2.5Nb-383* and *5Nb-383* while it appears insulated in nanodomains for the *10Nb-383* and *20Nb-383*.

The most important changes produced by the heat-treatment to the *SiO₂-873* FTIR spectrum concern the almost complete disappearance of the bands at 950 cm^{-1} ($\nu_{\text{Si-OH}}$) and 570 cm^{-1} ($\delta_{\text{Si-OH}}$), besides the relative intensities of absorption bands at about 3450 and 3670 cm^{-1} appears strongly altered with respect to the *SiO₂-383* spectrum. In accordance with Raman analysis, these results can be considered as a consequence of the polycondensation of silanol groups occurring at this stage of the heat-treatment. As the dehydroxylation takes place preferentially between silanols that interact most strongly with neighbours by H-bond [103], the fraction of free OH results enhanced in the residual OH groups.

For the Nb-containing samples the gel network densification seems to be the most important phenomenon occurring at this stage (873 K) as well. Actually, in these FTIR spectra the highest band ($\nu_{\text{as Si-O-Si}}$) occurs at the same wavenumber (1084 cm^{-1}). Therefore for each sample it results shifted toward higher wavenumbers with respect to the corresponding dried gel indicating that the siloxane frameworks of heat-treated samples are more highly crosslinked [43].

This phenomenon is a consequence of the de-hydroxylation that resulted more extended in the samples containing OH groups involved in stronger H-bonds. In fact, the relative intensity of the $\nu_{\text{O-H}}$ band appear strongly reduced in the *20Nb-873* spectrum (curve a) as well as its position is shifted towards higher energy (about 3500 cm^{-1}) with respect to the corresponding dried gel.

In accordance with Raman analysis, the dehydroxylation involves the formation of three-membered SiO_4 rings whose vibrations are IR active in the $550\text{--}750\text{ cm}^{-1}$ range [13, 124]. In this range a broad and asymmetric band is seen in the *20Nb-873* and *10Nb-873* FTIR spectra (curves a and b), even if in the latter with a lower relative intensity, indicating that the $\nu_{\text{Nb-O-Nb}}$ modes are overlapped with the SiO_4 rings ones. On the contrary, in the *5Nb-873* and *2.5Nb-873* spectra (curves c and d) no additional features are detected in the above range and, simultaneously, the contribution of the $\text{Si-O}^-(\text{-Nb})$ bonds to the band at about 950 cm^{-1} appears still low because it occurs at 945 cm^{-1} (curve c) and at 954 cm^{-1} (curve d), respectively. Therefore, in these samples the siloxane network densification does not change substantially the niobium dispersion that results still high at this stage.

The FTIR spectra of gel-derived samples heated at 1273 K point out the definitive transformation of the siloxane network into a silica-like one because in each spectrum the highest absorption band ($\nu_{\text{as Si-O-Si}}$) as well as its shoulder in the high wavenumber side ($\text{LO}\nu_{\text{as Si-O-Si}}$) occur at 1100 and 1250 cm^{-1} , respectively. Moreover, no absorption bands are seen in the $2000\text{--}4000\text{ cm}^{-1}$ range, indicating that the de-hydroxylation is at this point completed. As it was shown by the XRD analysis, at this stage the crystallization of different Nb_2O_5 polymorphs begin to

occur. Consequently, in the wavenumber range where the Nb–O vibration modes are active new bands appear, according to the niobium content and, simultaneously, the contribution of the Si–O⁻(–Nb) bonds to the band at about 950 cm⁻¹ becomes prevailing also in the *2.5Nb-1273* and *5Nb-1273* spectra where it appears as shoulder at 930 cm⁻¹ (curves c and d). For the T-Nb₂O₅ phase three different stretching modes should be expected: the collinear Nb–O–Nb (800–850 cm⁻¹), the Nb₃O (400–500 cm⁻¹) and the bridging Nb–O–Nb (580–750 cm⁻¹) [113]. Since the former two are overlapped with the ν_s Si–O–Si and $\delta_{\text{Si–O–Si}}$, respectively, only the latter can be well observed. Consequently, bands at 680 cm⁻¹ (*2.5Nb-1273*), 673 cm⁻¹ (*5Nb-1273*) and 668 cm⁻¹ (*10Nb-1273* and *20Nb-1273*) are seen in Figure 4.5. This trend can be related to the different crystallization extent occurring in the samples. An additional feature at 720 cm⁻¹ with the change of the band shape at about 800 cm⁻¹, related to the early crystallization of the H-Nb₂O₅ phase, is seen only in the *20Nb-1273* spectrum. The analysis of the FTIR spectra of gel-derived samples heated for 1 h at 1473 K confirms that the T-Nb₂O₅ phase is the only one crystallising in the *2.5Nb-1473*. On the contrary, the crystallization extent of the H-Nb₂O₅ phase seems to become the most important phenomenon increasing the niobium content. In fact, in the *5Nb-1473* FTIR spectrum the sole feature related to the T-Nb₂O₅ phase appears as a low intensity shoulder at about 650 cm⁻¹, while a new band at 720 cm⁻¹ with a shoulder at about 865 cm⁻¹ starts to appear, both of which can be related to the H-Nb₂O₅ phase. In the *10Nb-1473* and *20Nb-1473* FTIR spectra the above shoulder becomes a band occurring at 860 and 853 cm⁻¹, respectively. At the same time, the relative intensity of the band at about 720 cm⁻¹ strongly increases giving rise well resolved

bands at 713 cm^{-1} (curve b) and 700 cm^{-1} (curve a).

5 Textural and surface acid characterization of catalysts

XRD patterns show that all dried gels keep their amorphous nature up to 873 K , while at higher temperature crystallization of T- and H-Nb₂O₅ polymorphs occurs depending on the niobium content, in agreement with previous results. On the basis of these and previous TG/DTA data the catalysts were obtained by treating the dried gels at 673 K for 3 h, since this treatment allows to obtain the complete elimination of organic residues and stable gel-derived samples regardless of the niobium content.

5.1 N₂ adsorption

The N₂ adsorption-desorption isotherms of the catalysts and of the reference SiO₂ sample are reported in Figure. 4.6. For the sample Nb₂O₅, due to very low amounts of N₂ adsorbed, a complete isotherm is not determined, and BET surface area is estimated from few adsorption values. The silica sample gives a type I isotherm, that characterizes microporous adsorbents, according to the IUPAC classification [125]. The isotherm of 2.5Nb, similarly as that of SiO₂, shows a high amount of N₂ adsorbed at low pressure and a plateau for $P/P^\circ > 0.4$, corresponding to a volume of adsorbed N₂ higher than that of silica. The other samples show markedly lower amounts of adsorbed N₂ with different shapes of isotherms, without any plateau of N₂ volume.

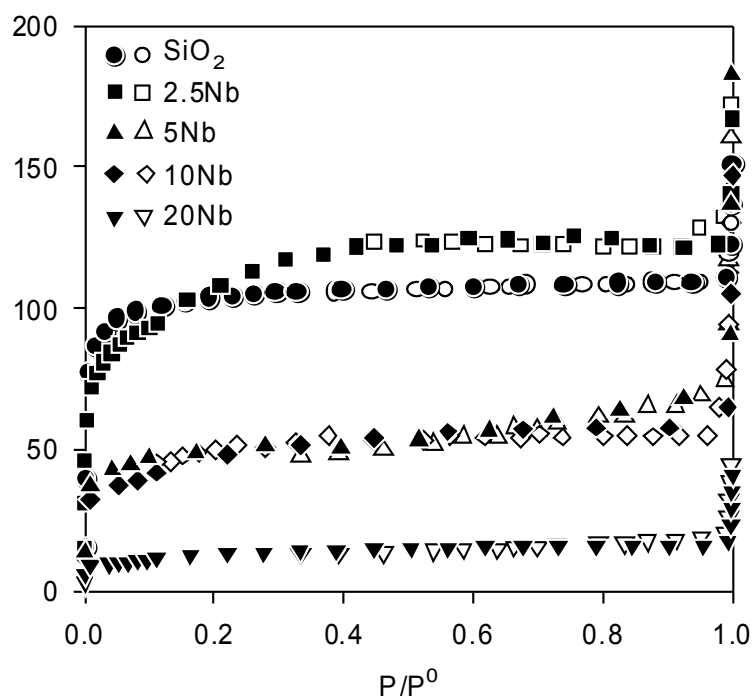


Fig. 4.6 N₂ adsorption-desorption isotherms of SiO₂ and of the investigated catalysts. Full symbols: adsorption; empty symbols: desorption.

In order to obtain deeper information on the texture of the catalysts, the data are elaborated, besides by BET, also by the α -plot method that is advisable for microporous materials [126]. The results are reported in Table 4.2. The α -plot method is not applied for 20Nb and pure Nb₂O₅ due to the low values of N₂ adsorbed. The α -plots reported in Figure 4.7 are typical of micro-mesoporous materials [16]. The plots give positive intercepts from which micropore volumes are calculated (Table 4.2). Surface areas due to contribution of meso and macropores are calculated from initial slopes of α -plots. As expected, the α -plot area is always lower than the BET one, since the former excludes the contribution of micropores, while the latter includes contributions of all pores. It can be noted that the surface area has a maximum for 2.5Nb while it reduces to less than half

for *5Nb* and *10Nb* and drops to a very low value for *20Nb*: a similar variation is shown by total pore volume. On the other hand the micropore volume is maximum for pure silica and decreases with increasing Nb content.

Table 4.2 Surface area and pore volume of Nb₂O₅·SiO₂ catalysts.

	Surface area		Pore volume	Micropore volume
	m ² g ⁻¹			
	BET	α -plot ^a	cm ³ g ⁻¹	cm ³ g ⁻¹
<i>SiO</i> ₂	313	183	0.170	0.090
<i>2.5Nb</i>	369	238	0.190	0.056
<i>5Nb</i>	159	137	0.107	0.023
<i>10Nb</i>	164	155	0.091	0.007
<i>20Nb</i>	46	-	0.030	-
<i>Nb</i> ₂ <i>O</i> ₅	6	-	-	-

^aIt excludes contribution of micropores.

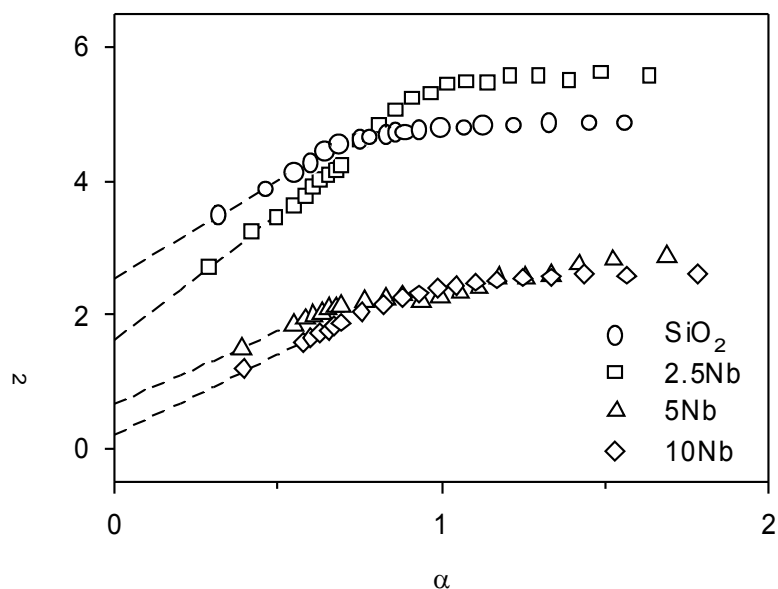


Fig. 4.7 α -plot of SiO₂ and of investigated catalysts.

A maximum of surface area for Nb₂O₅·SiO₂ systems at very low Nb content is also reported by other authors [19]. Such behaviour is explained by a very high Nb dispersion at low Nb/Si ratio, leading to formation of Nb–O–Si linkages [19,127]. Nb oxide species dispersed into SiO₂ probably cause elimination of SiOH groups and thus hinder the condensation between silica particles: this could give rise to a more open structure that could explain the higher values of surface area and pore volume of the sample *2.5Nb* compared with pure silica. On the other hand, increasing Nb content, surface area and total and micropore volume decrease probably due to formation of less dispersed species, that is niobia nanodomains or nanoparticles of Nb oxide, as observed for similar systems [127].

The pore size distribution of the catalysts, obtained by the BJH method, is reported in Figure 4.8.

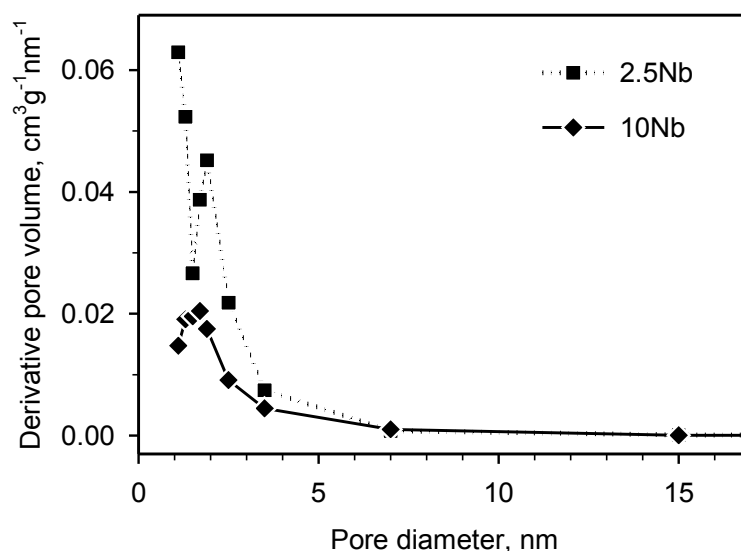


Fig. 4.8 Pore size distribution of the investigated catalysts.

The distribution curve of *5Nb* is very close to that of *10Nb* and is not reported, while for *20Nb* the low amount of N_2 adsorption does not allow to obtain reliable data. It is observed that the samples show a unimodal distribution of pore size with maximum at about 2.0–2.5 nm, indicating pore volumes decreasing with Nb content, in agreement with data of Table 4.2.

5.2 Ammonia Temperature Programmed Desorption and Fourier Transform Infrared spectroscopy with probe molecules

The results of NH_3 TPD measurements on the catalysts and the reference SiO_2 and Nb_2O_5 samples are shown in Figure 4.9. The amounts of adsorbed NH_3 calculated by integration of the TPD peaks are reported in Table 4.3.

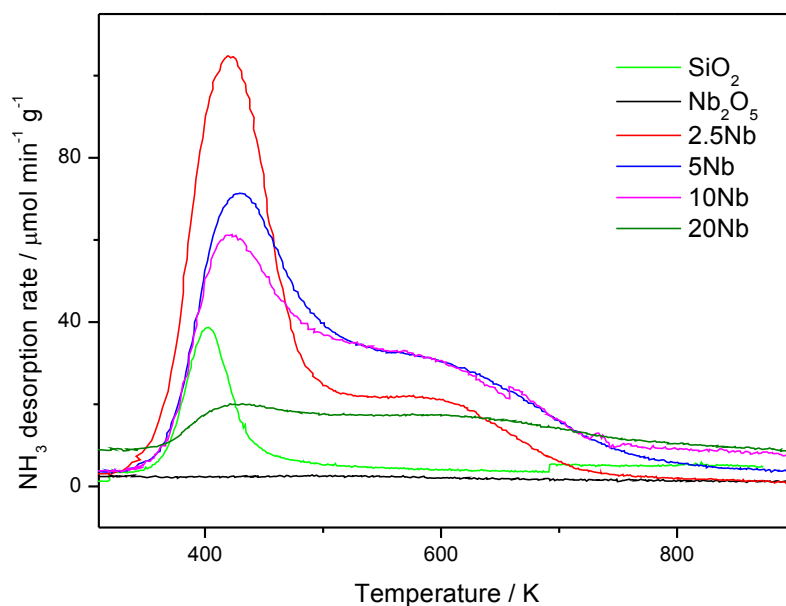


Fig. 4.9 NH_3 TPD spectra of SiO_2 , Nb_2O_5 and of the investigated catalysts.

Table 4.3 Temperature peaks, adsorbed NH₃ amounts and acid site concentration from TPD measurements.

	Temperature peaks		NH ₃ adsorbed		Acid site concentration sites·nm ⁻²
	K		mmol g ⁻¹	mol _{NH₃} mol _{Nb} ⁻¹	
<i>SiO₂</i>	403	-	0.17	-	0.33
<i>2.5Nb</i>	420	603	1.19	1.55	1.94
<i>5Nb</i>	429	628	1.20	0.85	4.54
<i>10Nb</i>	422	613	1.05	0.42	3.85
<i>20Nb</i>	429	628	0.31	0.078	4.05
<i>Nb₂O₅</i>	523	-	0.011	0.0014	~1

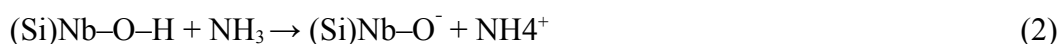
The profile of pure SiO₂ shows a symmetric peak at low temperature, that can be attributed to silanol groups acting as weak acid sites, as already observed for pure SiO₂ [16, 37, 38]. The Nb₂O₅ sample gives a broad signal with maximum at about 523 K, indicating medium strength acid sites, in agreement with literature data [128, 129]. The very low intensity of the TPD signal is related to the very low surface area of this material. The spectra of the catalysts appear different from both SiO₂ and Nb₂O₅, since two signals can be clearly distinguished in all spectra at 423–433 K and at 603–628 K, respectively. The former signal reaches the highest intensity for *2.5Nb* and decreases with Nb content, while the latter is maximum for *5Nb* and *10Nb*. These results suggest that at least two types of acid sites are present in the catalysts, and these are probably different from those existing in pure Si or Nb oxides. Moreover the relative concentrations of these sites depend on the composition of the materials. It is expected that the acid sites located on NbO_x species bonded to silica may be different from those existing on the surface of pure Nb₂O₅ crystals and that their properties depend on the nature of

Nb species formed.

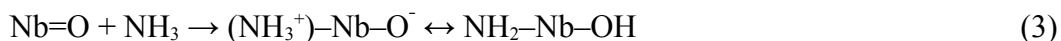
By the previous structural characterization of the samples, it was shown that in the amorphous materials different NbO_x species are present: NbO₄ tetrahedra, NbO₆ octahedra with a different distortion degree and niobia clusters. The relative amounts of these species depends on the Nb content: NbO₄ or NbO₆ isolated species prevail at low Nb content (*2.5Nb* and *5Nb*) while clustering of NbO₆ octahedra with the disappearance of NbO₄ tetrahedra occur at higher Nb content (*10Nb* and *20Nb*).

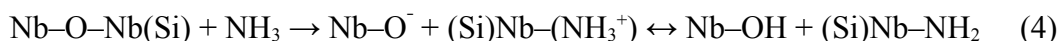
The presence of different NbO_x surface species interacting with the siloxane matrix can give rise to different acid sites [14, 23, 127, 130, 131]. Brønsted acid sites with moderate acid strength consist of OH groups bonded to silicon or to niobium polyhedra [14, 23, 130]. Lewis acid sites are related to both Nb=O, mainly as mono-oxo moiety, and Nb–O–Nb bonds within the molecular structure of NbO_x surface species [130].

On the basis of the above discussion the two different signals shown in Figure 4.9 can be related to Brønsted and Lewis acid sites, respectively. Actually, (Si)Nb–OH groups can act as Brønsted sites according to the following equation:



On the other hand, Nb=O, Nb–O–Nb and/or Nb–O–Si groups can act as Lewis acid sites:





Eqs. (3) and (4) show that a Lewis acid site, after reaction with NH_3 , can give rise to a new Brønsted acid site. The trend of the relative intensities of TPD peaks with the niobium content seen in Figure 4.9 agrees with the above hypothesis on the nature of Brønsted and Lewis acid sites. In fact, the decrease of the relative amount of weak acidity with Nb content can be related to the change of the polymerization degree of niobium polyhedra in the siloxane matrix. Increasing Nb content leads to the progressive polymerization of NbO_x species, with consequent condensation of Nb-OH groups producing self-condensation (Nb-O-Nb bridges) and/or cross-condensation (Nb-O-Si bridges). This causes a decrease of the amount of weak (Brønsted) acid sites. On the other hand, as regards strong (Lewis) acid sites, it can be noted that the samples *5Nb* and *10Nb* show the highest concentrations, while *2.5Nb* and *20Nb* exhibit lower concentrations. This trend is explained considering that two contrasting effects take place increasing Nb content: the decrease of Nb=O groups, mainly connected with decrease of NbO_4 tetrahedra, and the increase of Nb-O-Nb and Nb-O-Si bridges. The data reported in Table 4.3 show that all catalysts with exception of *20Nb* adsorb similar amounts of NH_3 per gram, with the consequence that the NH_3/Nb ratio decreases strongly with Nb content. This confirms that the effective availability of acid sites is mainly affected by Nb dispersion that strongly decreases with Nb content. Moreover the effect of the surface areas of catalysts, that decreases with Nb content, should be also taken into account

Likewise to previous works [132, 133], acetonitrile has been used as the

basic probe molecule for further characterization of the acid sites. In fact, this molecule is more sensitive to detect Lewis acid sites over the surface of silica-based materials in comparison with ammonia, as its sensitive bands do not fall near the cut-off spectral region. Moreover, acetonitrile has been used also as a probe for basic and nucleophilic sites, because it tends to form the $[\text{CH}_2\text{-CN}]^-$ anion upon attack of surface basic sites or to undergo hydrolysis due to attack of the nucleophilic sites on the electrophilic nitrile carbon atom [134–136].

The FTIR spectra of the catalysts, after activation, contact with acetonitrile and successive outgassing at different temperatures, are reported in Figures 4.10–4.12.

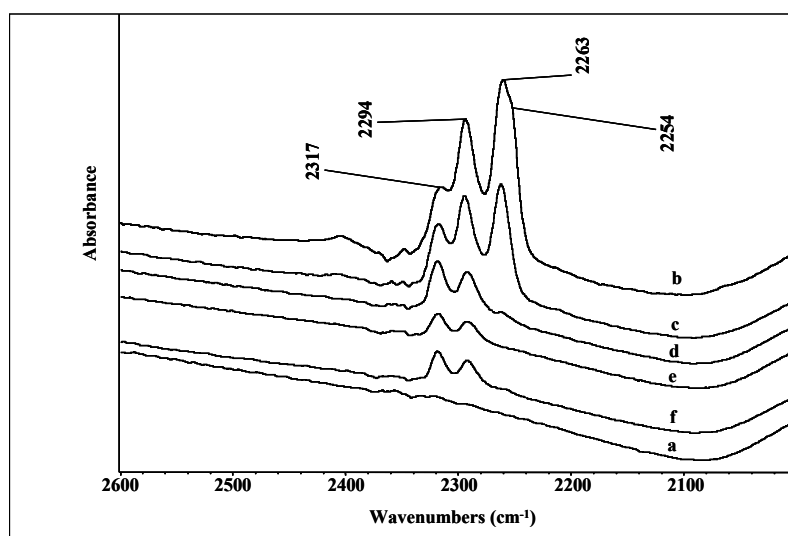


Fig. 4.10 FTIR spectra of pure *2.5Nb* pressed disk after outgassing at 773 K (a) and following contact with acetonitrile vapours 5 Torr (b) and successive outgassing at room temperature (c), 373 K (d), 473 K (e) and 573 K (f) for 10 min. The gas-phase spectra have been subtracted.

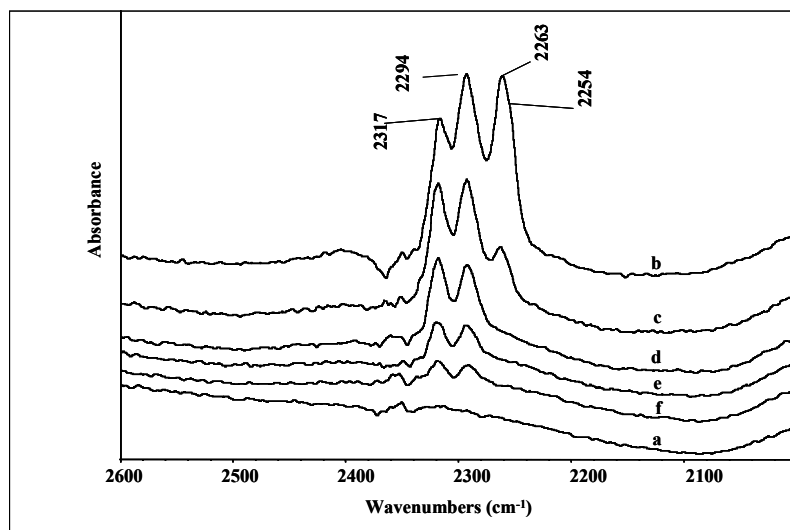


Fig. 4.11 FTIR spectra of pure *5Nb* pressed disk after outgassing at 773 K (a) and following contact with acetonitrile vapours 5 Torr (b) and successive outgassing at room temperature (c), 373 K (d), 473 K (e) and 573 K (f) for 10 min. The gas-phase spectra have been subtracted.

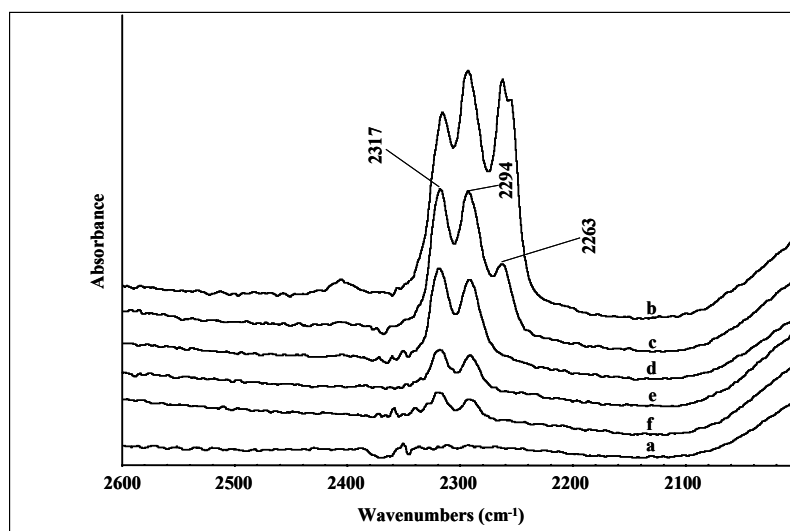


Fig. 4.12 FTIR spectra of pure *10Nb* pressed disk after outgassing at 773 K (a) and following contact with acetonitrile vapours 5 Torr (b) and successive outgassing at room temperature (c), 373 K (d), 473 K (e) and 573 K (f) for 10 min. The gas-phase spectra have been subtracted.

The spectra are registered in the wavenumbers range where the stretching modes of the C≡N bonds are active. In this region, liquid acetonitrile shows a strong doublet at 2293(w), 2254(s) cm⁻¹, the intensity of the latter band being definitely stronger. This doublet is due to the Fermi resonance between the C≡N triple bond stretching and the δ(CH₃) + ν(C–C) combination [137–140]. When an interaction between –CN groups of acetonitrile and electron-withdrawing centres occurs, a typical shift up of the doublet components in comparison with the value of the liquid molecule is observed, at the same time, a change of their relative intensity in favour of the higher frequency band is seen [139, 140]. Three bands are found in all investigated catalysts. These triplets result from the superimposition of two doublets. The doublet related to the more weakly adsorbed species, is characterized by a band which represents the triplet component located at the lowest frequency 2263 cm⁻¹, and the other one contributing to the triplet intermediate band at 2294 cm⁻¹. In fact, by degassing the sample already at 373 K, the triplet substantially evolves into a doublet, due to the disappearing of the two contributions of the more weakly adsorbed species. Consequently, in these cases the lower frequency is almost the same as that of the band of liquid acetonitrile or the band of acetonitrile adsorbed on silica [141].

Armaroli et al. [142] reported data of acetonitrile adsorption over niobic acid, niobium phosphate and phosphoric acid-treated niobic acid. By comparison, the present FTIR data indicate that hydrogen bonding of acetonitrile with surface hydroxyl groups is significantly stronger than that with silica, phosphoric acid-treated niobic acid and niobic acid.

In all samples, by outgassing at 373 K or even at higher temperatures, the

spectra evolve into a doublet arising from a resisting species. The components of the doublet, having now similar intensity, are observed at 2317 and 2294 cm^{-1} (Figures 4.10–4.12). These features are typical of acetonitrile molecules adsorbed on Lewis acid sites with medium, medium-strong strength [143]. In all samples there are sites of similar strength as indicated by the position of the bands, although the comparison of their relative intensity suggests that in *2.5Nb* there is a slightly higher amount of weaker acid sites than stronger ones, also in agreement with ammonia TPD results. In any case, the Lewis strength of these sites is still not very high in comparison to very acidic surfaces such as those of alumina [144] or vanadium pentoxide [132] and vanadyl pyrophosphate [145] and is comparable to medium acid niobium phosphates [30]. The absence of bands in the region 2200–2100 cm^{-1} , distinctive of the $\text{C}\equiv\text{N}$ stretching of coordinated $[\text{CH}_2\text{-CN}]^-$ anion (near 2050 cm^{-1} for “free” $[\text{CH}_2\text{-CN}]^-$ ions in solution), indicates that there are no basic sites on the surface of the studied catalysts which are able to abstract a proton from the methyl group of acetonitrile. The absence of bands due to amide, carboxylate and similar species in the region 1800–1000 cm^{-1} indicates that the hydrolysis of the $\text{C}\equiv\text{N}$ bonds does not occur.

Due to the very low surface area of *20Nb*, its spectra, exhibiting very weak bands of adsorbed acetonitrile, are not reported.

In order to gain a deeper insight into the interaction of acetonitrile with surface OH groups, the strength of the resulting hydrogen bonds has been investigated. The FTIR spectra of the samples after outgassing at 773 K and following contact with acetonitrile vapours, recorded in the wavenumbers range

where the stretching modes of the O–H bond are active, are reported in Figure 4.13.

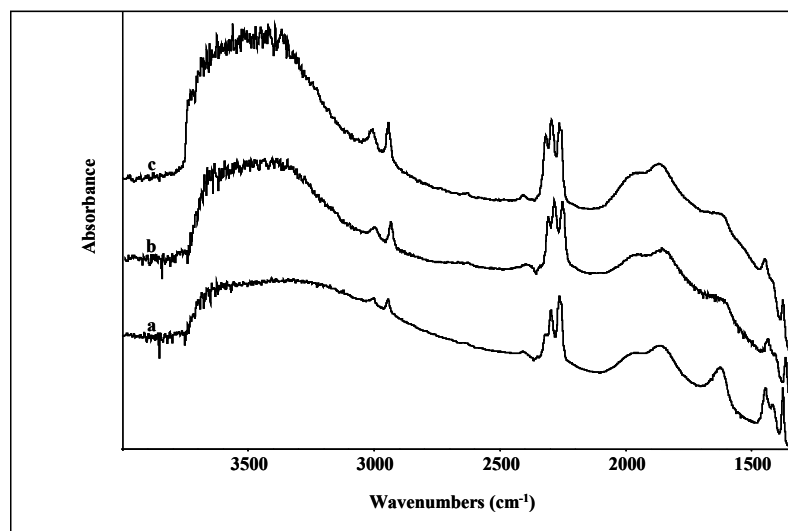


Fig. 4.13 FTIR spectra of pure $2.5Nb$ (a), $5Nb$ (b), $10Nb$ (c) pressed disks after outgassing at 773 K and following contact with acetonitrile vapours (5 Torr). The gas-phase spectra have been subtracted.

In the region near 3700 cm^{-1} the absorption due to the O–H stretching of free surface OH groups disappears upon adsorption of acetonitrile. At lower frequency, the stretching absorptions of hydroxy groups interacting with acetonitrile by H-bonding are observed as a broad band, the frequency of which depends on the strength of Brønsted acid sites. In fact, the extent of the shift of the absorption band is typically used to measure the strength of H-bond [143]. The broad band centred near 3250 cm^{-1} , in the case of $2.5Nb$, corresponds to the frequency observed after adsorption of acetonitrile over niobic acid [142], while in pure silica the maximum is detected near 3415 cm^{-1} [141], thus providing evidence for the stronger Brønsted acidity with respect to Si–OH groups. By increasing Nb amount the spectra are not very different, however it seems that the

relative amount of weaker Brønsted acid sites, with an acidity similar to those observed over pure silica, increases.

6 Catalytic tests

6.1 Catalytic activity and reaction mechanism

The results of catalytic activity tests on *2.5Nb*, *5Nb* and *10Nb* samples are reported in Figure 4.14 as conversion of cyclooctene to epoxycyclooctane at increasing times.

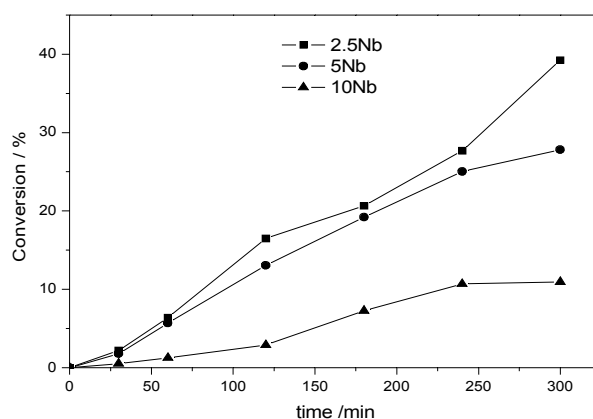


Fig. 4.14 Conversion versus time plots of epoxidation of cyclooctene with hydrogen peroxide catalyzed by differently loaded $\text{Nb}_2\text{O}_5\cdot\text{SiO}_2$ catalysts.

According to Somma et al. [21, 37, 38] methanol was used as solvent because it is completely miscible with hydrogen peroxide thereby ensuring a good homogeneity to the reagent mixture. Cyclooctene epoxidation was chosen as reaction test because this reaction does not give byproducts due to the high stability of the corresponding epoxide. In fact, cyclooctene epoxide was the only

product detected in the liquid (organic) phase. A summary of the reagent conversions and the selectivity of hydrogen peroxide to epoxide – calculated as moles of epoxide formed/moles of hydrogen peroxide reacted – at the end of the runs is given in Table 4.4.

Table 4.4 Oxidation of cyclooctene with hydrogen peroxide catalyzed by different niobium containing catalysts^a

Catalyst	Conversion (%)		H ₂ O ₂ selectivity ^(b) (%)
	Cyclooctene	H ₂ O ₂	
<i>2.5Nb</i>	39	82	48
<i>5Nb</i>	28	77	36
<i>10Nb</i>	12	30	40

^a Experimental conditions: catalyst, 600 mg; cyclooctene, 40 mmol; H₂O₂, 40 mmol; MeOH, 30 ml; T = 343 K; reaction time = 300 min. Under nitrogen atmosphere.

^b H₂O₂ selectivity is calculated as a ((mol cyclooctene reacted)/(mol H₂O₂ reacted)) × 100.

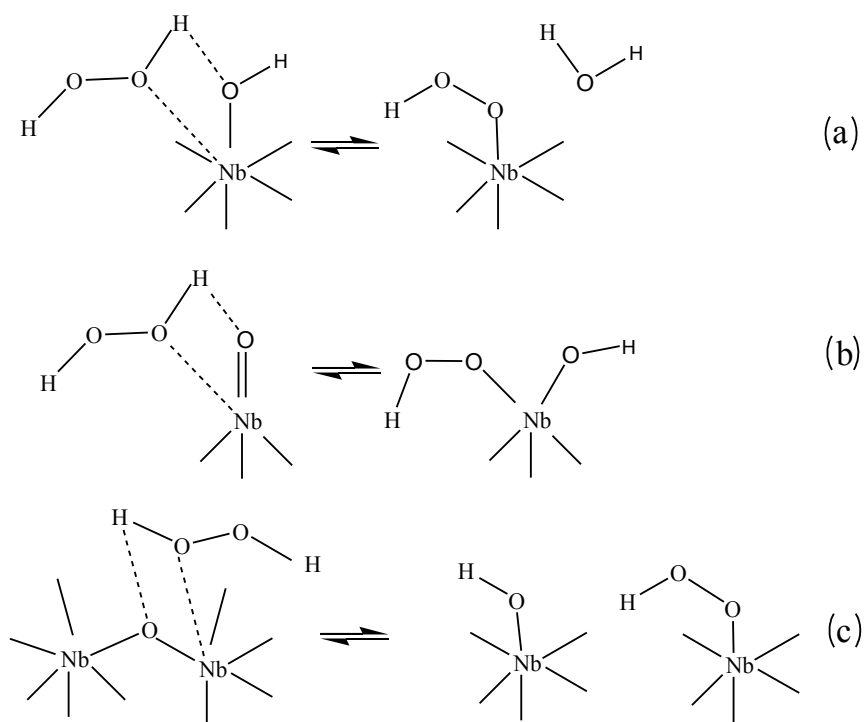
The leaching of the active species into the liquid phase under operating conditions has been verified removing the catalyst from the reaction mixture by filtration after 150 min from the start of the reaction, when the cyclooctene conversion is lower than 20% (*2.5Nb*), 15% (*5Nb*) and 5% (*10Nb*) (Figure 4.14), and then recording the residual conversion for additional 150 min. For each catalyst (*2.5Nb*, *5Nb* and *10Nb*) almost no detectable subsequent conversion in the filtrate after removing the catalyst was observed, giving a very strong evidence that these materials act as real heterogeneous catalysts. Moreover, this result shows that the adopted synthesis procedure allows to obtain materials characterised by a very high dispersion degree of niobium also at high niobium

content and presenting NbO_x species strongly held in the matrix.

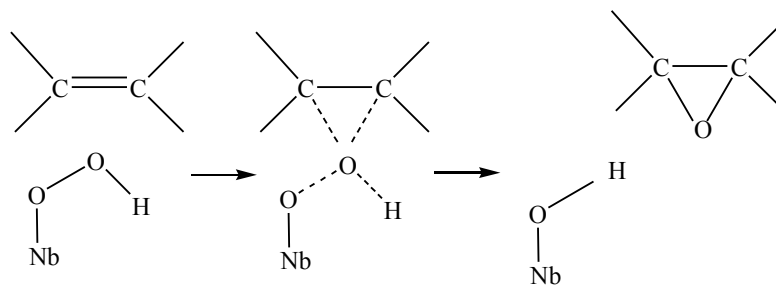
Data in Table 4.4 show that the catalytic activity is strongly affected by Nb content: the *2.5Nb* catalyst exhibits the highest cyclooctene conversion at each stage of the reaction and the highest selectivity of H₂O₂ to epoxide at the end of the runs. The catalyst *5Nb* shows a similar behaviour, while *10Nb* exhibits a markedly lower activity since the cyclooctene conversion reaches only 10% after 5 h reaction time with H₂O₂ selectivity of 40%. With the sample *20Nb*, no epoxide formation is observed. These results can be compared with those obtained under similar conditions on Nb₂O₅·SiO₂ aerogel catalysts by Somma et al. [21, 37, 38]. It can be noted that the values of cyclooctene conversion as a function of reaction time for the catalysts *2.5Nb* and *5Nb* are similar to the corresponding values obtained with the Nb₂O₅·SiO₂ aerogel ones; the values of H₂O₂ conversion are lower, but this can be due to the higher H₂O₂/cyclooctene feed ratio used in the present work. Therefore, the present data are comparable to those previously reported, although the catalysts have lower surface areas.

It is appropriate to relate catalytic activity data with physical and chemical properties of the catalysts. From Table 4.2, it can be noted that the most active catalyst, *2.5Nb*, has the highest surface area and pore volume, and the sample *20Nb*, with negligible activity, also shows the lowest values of these properties: however, such correlation is not always valid, since, for example, samples *5Nb* and *10Nb*, that show similar values of surface area and pore volume, have largely different activity. This behaviour points to a variation of the nature of the catalyst surface with Nb content and can be explained by the presence of different Nb species depending on the catalyst composition. It is generally believed that acid

sites of moderate strength are involved in the mechanism of epoxidation of alkenes with H_2O_2 [21, 23, 27, 146–148], while strong acidity activates the decomposition of H_2O_2 [148]. The likely mechanism involves the reaction of an olefin molecule with a Nb–O–O–H group. This group is formed by reaction of H_2O_2 with the acid sites of the catalysts according to the Scheme 4.1. The reaction involves Brønsted (Scheme 4.1a) or Lewis type sites (Scheme 4.1b and 4.1c). The epoxide formation occurs through electrophilic transfer of oxygen favoured by the high polarizing effect of Nb^{5+} , according to the Scheme 4.2.



Scheme 4.1



Scheme 4.2

The equilibria shown in the Scheme 4.1 are shifted more or less to right, determining the nature and concentration of the reactive intermediate, and so the velocity of epoxidation. It should be noted that in every pathway shown in the Scheme 4.1, the formation of a Nb–O–O–H group involves the increase of niobium coordination. Consequently, fourfold niobium gives rise to hydroperoxide groups more easily than the sixfold one.

The decrease of catalytic activity with Nb content agrees with the decrease of the concentration of acid sites of moderate strength: however, the activity trend cannot be explained considering only the concentration of acid sites, because this is almost the same for the *5Nb* and *10Nb* catalysts. Therefore, other factors must be taken into account, among them the Nb coordination. The previous Raman investigation [has](#) showed that the coordination of Nb depends on its content, that is NbO₄ tetrahedra are present (together with NbO₆ species) in *2.5Nb* and *5Nb* samples, but disappear in *10Nb* and *20Nb*, where only NbO₆ groups are present. Since the epoxidation reaction involves coordination on a NbO_x species (Scheme 4.1), it is clear that the reaction is favoured on *2.5Nb* and *5Nb*, where the coordination of Nb is lower. This could explain the large decrease of activity

observed with the catalyst *10Nb* in comparison with *5Nb*. The presence of strong acid sites able to activate H₂O₂ decomposition can explain the low H₂O₂ selectivity values for all catalysts (Table 4.4): the higher selectivity of *2.5Nb* can be related to a lower concentration of strong acid sites, as can be observed in Figure 4.9.

6.2 Catalyst stability

To test the stability of the catalysts, repeated runs with a *2.5Nb* sample were performed. The catalyst after each run was separated by filtration and directly reused for a new run. The obtained results are reported in Table 4.5.

Table 4.5 Effect of recycling in the epoxidation of cyclooctene with hydrogen peroxide catalyzed by Nb₂O₅·SiO₂ catalysts^a.

Catalyst	Cycle	Conversion(%)
<i>2.5Nb</i>	1st	39.5
	2nd	36.3
	3rd	37.5
	4th	34.9

^a Experimental conditions: catalyst, 600 mg; cyclooctene, 40 mmol; H₂O₂, 40 mmol; MeOH, 30 ml; T = 343 K; reaction time = 300 min. Under nitrogen atmosphere.

Only a slight loss of catalyst activity can be observed, indicating that the catalyst is quite stable also after four stages.

CHAPTER 5

The $\text{Li}_2\text{O}\cdot\text{Nb}_2\text{O}_5\cdot\text{SiO}_2$ Ternary System:

Results and Discussion

Nanocomposite transparent thin films formed by LiNbO_3 nanocrystals uniformly dispersed in amorphous silica matrix have been obtained by a new sol-gel route. In the $\text{Li}_2\text{O}\cdot\text{Nb}_2\text{O}_5\cdot\text{SiO}_2$ ternary system a wide composition range was deeply explored to find the suitable process parameters for the film preparation. Particularly, at the first stage bulk gels were synthesized then, as intermediate step to approach the film preparation, a synthesis procedure was set to obtain transparent flakes with thickness lower than 0.5 mm. Finally, the suitable sol-gel route was set to obtain transparent thin films.

1 Bulk and flakes

Bulk gels were obtained by a suitable modification of the sol-gel route previously described to synthesize gels in the $\text{Nb}_2\text{O}_5\cdot\text{SiO}_2$ binary system.

LiNO_3 was used as lithium precursor because it is an easily-handled and cheap precursor in spite of organic lithium precursors that are expensive, reactive and need to operate in controlled conditions. The Li/Nb ratio was kept equal to one in all gel compositions according to the stoichiometric Li/Nb ratio in LiNbO_3 .

Firstly, $5\text{Li}_2\text{O}\cdot 5\text{Nb}_2\text{O}_5\cdot 90\text{SiO}_2$ (*B-5LN*) and $10\text{Li}_2\text{O}\cdot 10\text{Nb}_2\text{O}_5\cdot 80\text{SiO}_2$ (*B-10LN*) bulk gels were prepared.

Figure 5.1 displays the TG/DTA curves recorded on bulk dried gel samples.

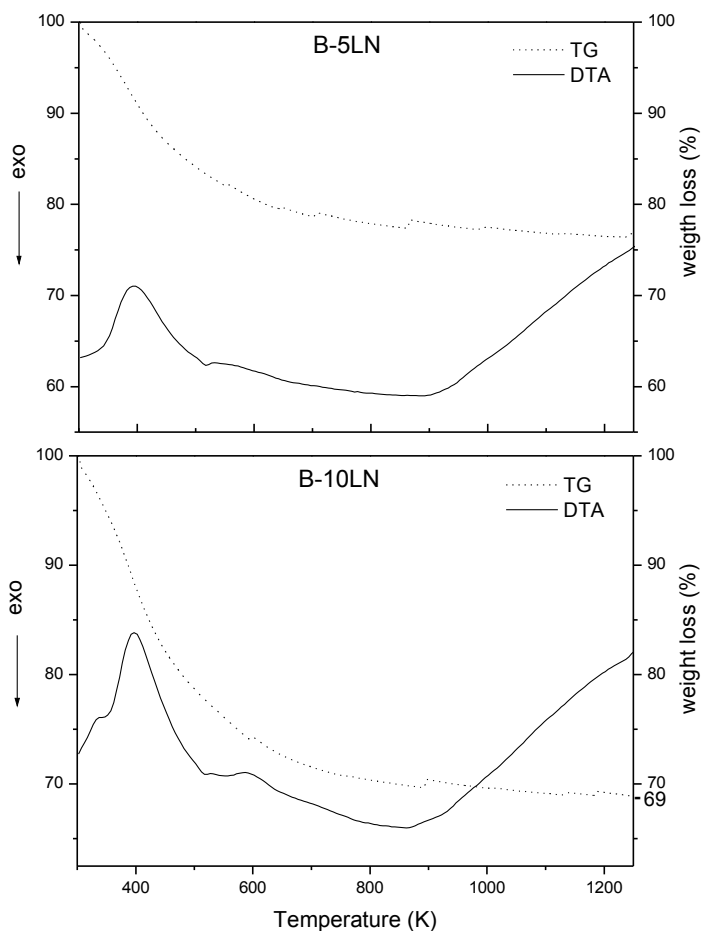


Fig. 5.1 DTA (solid line)-TG (dotted line) curves of bulk gels recorded in air at 10 K min^{-1} .

The overall weight losses obtained by the TG curves were: 23 wt % (*B-5LN*) and 31 wt % (*B-10LN*). In each case, the majority of the weight loss takes place between room temperature and about 523 K. In this range, on the DTA curves of both the samples, a broad endothermic peak is seen with a maximum at about 393

K, that can be related to the evaporation from open pores of water and alcohol molecules physically trapped in the gels. No other evident transformations are seen at higher temperatures on the DTA curves and the weight loss can be considered complete at about 773 K. On this basis, 4 h heat-treatment at 673 K was performed to stabilize gels in their amorphous state.

To force the crystallization, isothermal heat-treatments were performed at 923, 973, 1023 and 1073 K on the stabilized samples. Each sample was slowly heated (5 K min^{-1}) up to selected temperature and held 4 hours. The corresponding XRD spectra are shown in Figure 5.2. Hereafter the heat-treated samples will be indicated by their labels followed by the temperature of the heat-treatment (*B-5LN-923*, etc).

The coherent scattering regions start to appear from the amorphous background at $2\Theta = 22.4^\circ$, in the *B-5LN-923* spectrum. This value corresponds to the most intense peak of the T-Nb₂O₅ phase (JCPDS card 27-1312). The width of this peak suggests that the precipitation in the amorphous matrix of crystals on nanometric scale takes place. On the contrary, peaks related to LiNbO₃ (JCPDS card n. 85-2456), start to appear in the spectrum of the *B-10LN-923* besides to that of the T-Nb₂O₅ phase. In the subsequent heating stage (973 K) no significant differences are seen in the XRD profiles of both samples. At higher temperatures, for the *B-5LN* the crystallization of a few new phases, among them LiNbO₃, begins even if the T-Nb₂O₅ is the predominant phase at each stage of heat treatments. But for the *B-10LN* sample, the intensity of LiNbO₃ peaks increases with the heat-treatment temperature; for this composition lithium niobate is the predominant phase at each temperature, even if small amounts of T-Nb₂O₅ and LiNb₃O₈ (JCPDS card 26-

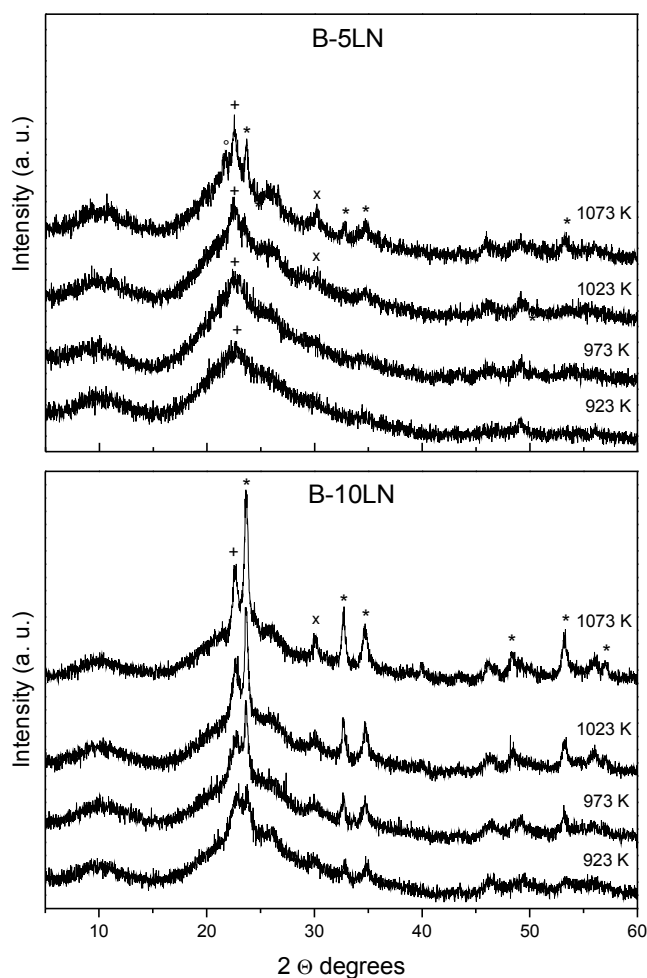


Fig 5.2 XRD patterns of the bulk gels heat 4 h at different temperatures. * LiNbO_3 , + $\text{T-Nb}_2\text{O}_5$, \times LiNb_3O_8 , $^\circ$ cristobalite.

1176) are present. The XRD data indicate that LiNbO_3 amount increases with Li and Nb content. Therefore, because this work is aimed to obtain transparent films containing LiNbO_3 nanocrystals as the main phase, the *5LN* composition was rejected since it gave a low amount of LiNbO_3 and a new gel, with a composition $15\text{Li}_2\text{O}\cdot 15\text{Nb}_2\text{O}_5\cdot 70\text{SiO}_2$ (*15LN*), has been synthesized. At this intermediate step toward the films preparation, gels were obtained as transparent flakes with

composition *F-10LN* and *F-15LN*. In fact, the flakes were obtained by a slow evaporation of water and/or solvent molecules from the sol producing gelation. This mechanism is quite similar to that of film formation in which evaporation and gelation simultaneously occur.

The TG/DTA curves of the dried flakes did not show substantial differences with the ones of the bulk gels. Therefore, the same stabilization heat-treatment (4 h at 673 K) was used.

To check the LiNbO_3 crystallization, even the flakes were heated for 4 hours at different temperatures (823, 873 and 923 K). These values, lower than those of the bulk samples, have been used in order to see the very beginning of the crystallization, since in *B-10LN* sample it already starts at 923 K. The knowledge of the lowest temperature value at which LiNbO_3 crystals grow is important to control crystals size.

The XRD spectra of the *F-10LN* and *F-15LN* samples heated 4 h at different temperatures are reported in Figure 5.3. The *F-10LN-823* is still amorphous, while the *F-10LN-873* XRD spectrum shows a crystallization early stage with few low intensity peaks, corresponding to the most intense ones of LiNbO_3 . In the subsequent heating stage, the crystallization of LiNbO_3 is enhanced even if the peaks broadening as well as the transparency of the crystallized sample point out to nanocrystallization; the average crystal size, roughly estimated by the Scherrer formula (already reported in section 4.1), was about 8 nm. It is worth to note that, contrary to the *B-10LN* where several crystalline phases were formed, in the *F-10LN* LiNbO_3 was the only crystallizing phase.

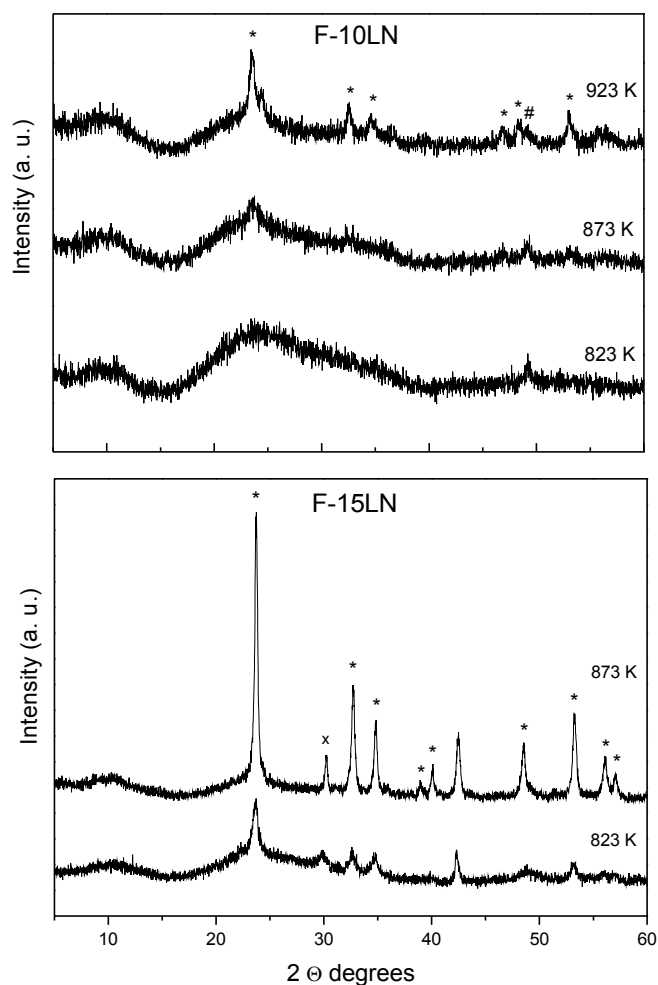


Fig. 5.3 XRD patterns of the flakes gels heat 4 h at different temperatures. * LiNbO_3 , \times LiNb_3O_8 , # sample holder.

In the case of the *F-15LN*, the XRD spectra reported in Figure 5.3 indicate that the crystallization of LiNbO_3 is enhanced and only a small amount of LiNb_3O_8 is formed both at 823 K and at 873 K. The LiNbO_3 average crystal size, increasing with the temperature, is about 24 nm at 873 K.

Gel-derived flakes, with a composition $(6\text{Li}_2\text{O}\cdot 6\text{Nb}_2\text{O}_5\cdot 88\text{SiO}_2)$ similar to

that of the *10LN*, have been recently synthesized by Graça et al. [75] starting from the same precursors used in this work. It was found that, flakes heated in the same temperature range, give rise to crystobalite, $\text{Li}_2\text{Si}_2\text{O}_5$ and Li_3NbO_4 besides LiNbO_3 . This attests the quality of our novel sol-gel route.

The results on the flakes indicate that with *10LN* composition the LiNbO_3 crystallization is slower but it is the only crystallizing phase, while at *15LN* it is enhanced but coupled with a certain amount of LiNb_3O_8 . Therefore, *10LN* appears to be the composition more suitable to prepare thin film of $\text{LiNbO}_3\cdot\text{SiO}_2$ nanocomposite with nanocrystals well dispersed in the silica matrix.

2 Thin films

Taking in account the above results, the $10\text{Li}_2\text{O}\cdot 10\text{Nb}_2\text{O}_5\cdot 80\text{SiO}_2$ composition was selected for the thin films preparation (*TF-10LN*) by dip-coating on Si-SiO_2 and Al_2O_3 substrates. The sol was diluted by EtOH to reduce its viscosity and to increase the gelation time, to obtain enough thin and reproducible films. The dried films, stabilized by 3 h heating at 673 K, were fully amorphous, transparent and crack-free.

To induce the crystallization of LiNbO_3 in the thin films, isothermal heat-treatments were performed on the stabilized films at 873 , 973 and 1073 K. Each sample reached the selected temperature by a heating rate of $10\text{ K}\cdot\text{min}^{-1}$ and then was held at this temperature for 2 h. Transparent, homogeneous and crack-free films were obtained after these heat-treatments. The heat-treated samples hereafter will be referred to as their already specified labels followed by the temperature of the heat-treatment stage (*TF-10LN-873*, etc).

For each sample, the thickness resulted in the range 350-400 nm, and the RMS roughness resulted in the range 0.5-3 nm, both measured with a TENCOR profilometer.

The control of the thickness is extremely important due to its strong influence on the grain size and the electric properties of LiNbO₃. In fact, by literature data [149], it is known that the grain size of LiNbO₃ increases with increasing thickness of the film layer, indicating that the amount of material deposited on the surface of substrate influences the microstructure. Moreover, it was observed that for thin films interfacial dead layer could appear at the interface between films and substrate. This layer degrades the performance of the device as regard the electrical properties. The detrimental effects of the dead layer, originate from oxygen interdiffusion, chemical reaction or structural defects at the interface with the substrate, could be suppressed by increasing the film thickness above 200 nm [149]. Thus, in this work films were obtained with thickness in the range 350-400 nm. Also the control of the surface roughness is fundamental since electric properties depend not only on a well-defined microstructure but also on the interactions between the electrode and the film interface. The roughness values obtained in this work are low enough to allow good interaction at the interface between the electrode and the film, thus good contact resistances.

2.1 Thin films on Si-SiO₂ substrates

2.1.1 X-Ray Diffraction

The *TF-10LN* films deposited on Si-SiO₂ substrates after post growth thermal treatment are amorphous up to 973 K as verified by XRD measurements

(not reported here), collected by Bragg-Brentano configuration. LiNbO_3 nanocrystals were obtained only by heating 2 h at temperature of 1073 K. The corresponding XRD spectrum is shown in Figure 5.4, where the peaks located at $2\theta = 23.7^\circ$, 32.7° and 34.8° correspond to the polycrystalline LiNbO_3 phase. The characteristic peaks for Si-SiO₂ substrate were observed at $2\theta = 26,7^\circ$ and 33° . It can be observed that only LiNbO_3 nanocrystals are formed into the amorphous silica matrix and with an average size of 27 nm.

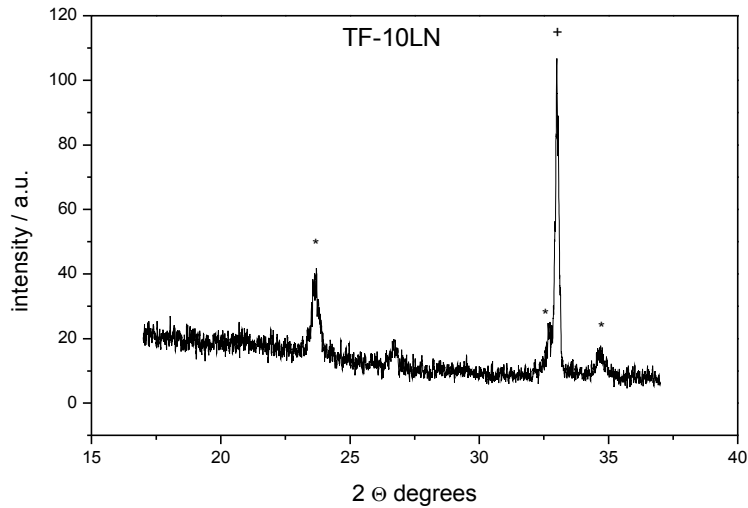


Fig. 5.4 XRD pattern of the heat-treated *TF-10LN* film deposited on Si-SiO₂ substrate. * LiNbO_3 , + substrate.

2.2 Thin films on Al₂O₃ substrates

2.2.1 Atomic Force Microscopy

The morphological features of the heat-treated films were studied using a AFM in non contact mode. Films annealed at 673 K show uniformity from the macro- to the nano-scale as displayed in Figure 5.5a, where a typical AFM image

is reported. The film microporosity can be seen at higher magnification (inset of Figure 5.5a).

AFM investigation reveals a clear modification of the film surface morphology at higher temperatures. The AFM images of the film annealed at 873 K are displayed in Figure 5.5b. The surface is characterized by a network of flat structures which are about 5 nm in height. These structures appear also on samples annealed at higher temperature slightly changing in shape and dimension but preserving the typical height 5 nm. At a higher magnification (see inset of Figure 5.5b) the surface is characterized by nano-particles whose mean size is about 20–30 nm.

The accurate evaluation of the nanoparticles size on rough surfaces is not an easy task [150]. In fact, since AFM images are the result of interactions between a sharp tip with a quasi-spherical apex and the surface of a sample, they are highly influenced by the tip geometry especially when the surface features are comparable in size with the probe (dilation). In fact, if the nanoparticles lie isolated on a flat surface, size determination may be easily achieved by evaluating its height. However, when the nanoparticles lie on rough surfaces or are placed one close to each other the actual particle height cannot be evaluated, thus the lateral information is needed for size determination. It has been shown that lateral dimension may be up to 40%-overvalued by the AFM image if a conventional 10 nm curvature radius tip is employed [151]. In this case the true size may be determined by a curvature-reconstruction method provided the nanoparticle shape can be approximated by a sphere.

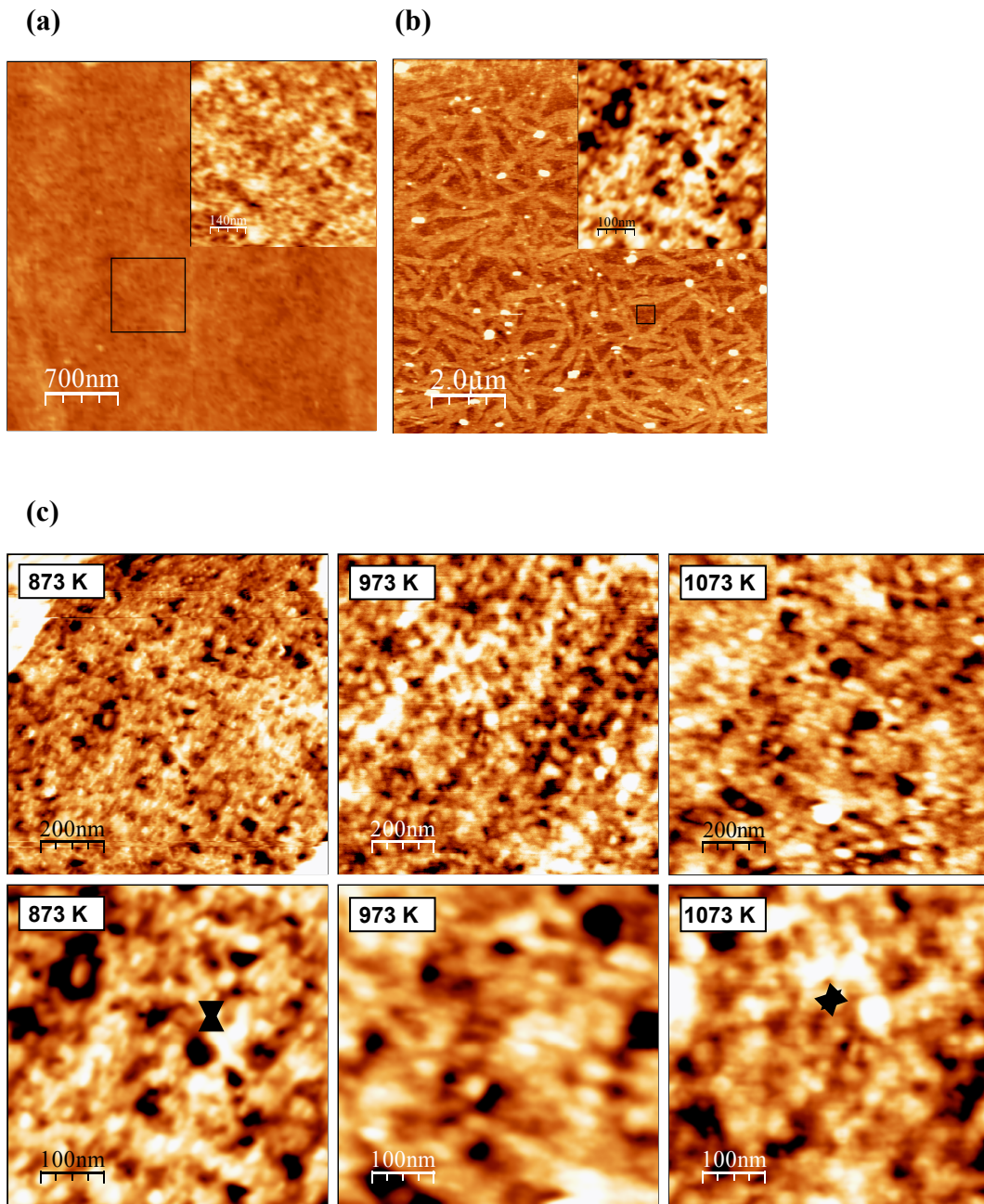


Fig. 5.5 AFM images of a $\text{LiNbO}_3\text{:SiO}_2$ films: **a** A film annealed at 673 K. In the inset is enlarged the marked area. Scanned area and z-scale are respectively $3.5 \times 3.5 \mu\text{m}^2$ and 10 nm for the main image while they are $700 \times 700 \text{ nm}^2$ and 4.0 nm for the inset. **b** A film annealed at 873 K. In the inset is enlarged the marked area. Scanned area and z-scale are respectively $10 \times 10 \mu\text{m}^2$ and 20 nm for the main image while they are $500 \times 500 \text{ nm}^2$ and 4.0 nm for the inset. **c** Films annealed at 873 K (left side), 973 K (middle) and 1073 K (right side). Scanned area and is $1 \times 1 \mu\text{m}^2$ in the top sequence, $500 \times 500 \text{ nm}$ in the bottom one. Z-scale is 4 nm.

Although precise size determination are not straightforward, because of the tip dimension, the sequence of AFM images in Figure 5.5c clearly show an increasing trend in the particle size with the increasing of annealing temperature, in particular films treated at 973 and 1073 K exhibit an average particle size which is approximately 50% higher than on films treated at 873 K.

2.2.2 X-Ray Diffraction

The crystallization process was routinely studied by XRD using a Rigaku D-Max B diffractometer, with the Bragg-Brentano configuration.

The crystal structure of the LiNbO_3 in the ferroelectric phase is rhombohedral (R3c space group) with lattice parameters $a=5.148\text{\AA}$ and $c=13.863\text{\AA}$.

The XRD spectra of the heat-treated films are shown in Figure 5.6.

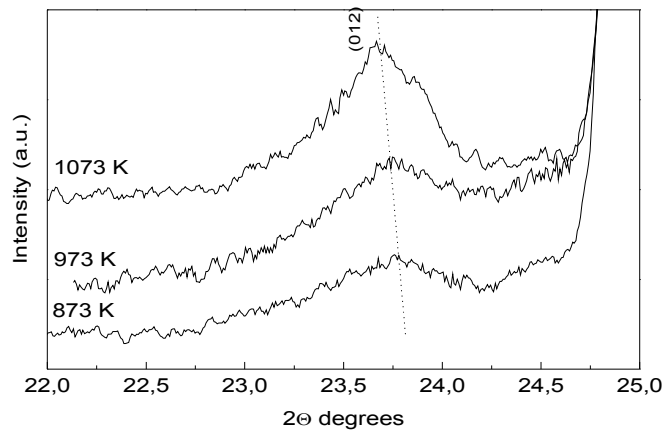


Fig. 5.6 XRD spectra of the heat-treated *TF-10LN* sample deposited on Al_2O_3 substrate. The straight line is a guide for eyes.

The *TF-10LN-673* is amorphous (the spectrum not is reported here), while the *TF-10LN-873* XRD spectrum shows an early crystallization stage with a weak peak, the intensity increases in the *TF-10LN-973* and *TF-10LN-1073* samples. This crystallization peak correspond to the (012) reflection of LiNbO₃ phase (the most intense reflection), occurring at $2\theta=23.7^\circ$. In Figure 5.6 can also be observed that the (012) reflection of the films emerges from the tail of the (012) reflection of the Al₂O₃ substrate located at $2\theta=25.57^\circ$. Thought the very strong diffraction signal of the substrate prevents the careful fit of the (012) peak profile of the film, it was roughly estimated the average grains size with the Scherrer equation. The corresponding grains size values are reported in Table 5.1 together with the structural parameters obtained by the XRD measurements.

Table 5.1 The structural parameters extracted from XRD spectra.

Sample	Annealing temperature (K)	Grains size (nm)	d_{012} (Å)
<i>TF-10LN-873</i>	873	7±3	3.73±0.01
<i>TF-10LN-973</i>	973	16.0±3	3.73±0.01
<i>TF-10LN-1073</i>	1073	18.0±2	3.750±0.005

The data show that the selected heat-treatments favor the nanometric grains formation and that the grains size enhance with the annealing temperature, ranging from about 7 to 18 nm. Correspondingly, the shift of the (012) peak positions toward lower angles in the XRD spectra, evidences an increasing of the lattice spacing towards the bulk value ($d_{012}=3.749\text{Å}$). The extracted lattice spacings are reported in Table 5.1.

This effect is in agreement with the strain relaxation in the nanocrystals, which occurs when the grains dimension enhances thanks to the higher annealing temperature. Films obtained at 600 K from the stabilization process without any post-annealing treatment, have not evidenced the formation of the nanocrystals, confirming the fundamental role of the annealing temperature chosen in the formation of the nanocrystals.

To obtain higher sensitivity to the films structure, XRD were also performed by a Bruker D8 Advance diffractometer (Cu $K\alpha$) using the glancing incidence configuration (GIXRD). The increased intensity of the diffraction beam from the film layer on the thick substrate possibly allowed to better detect also the less intense Bragg reflections. All data obtained by GIXRD confirm the results obtained by the more conventional Bragg-Brentano XRD and gave more insight into the structural properties of the films.

Films annealed at 673 K are amorphous by GIXRD spectra (not reported here), as already ascertained by the above XRD analysis in Bragg-Brentano configuration.

Figure 5.7 reports GIXRD measurements collected at incidence angle of 1.0° on samples annealed at 873, 973 and 1073 K. The asterisks indicate the Ag reflections due to electrical contacts. All the other peaks have been indexed with the JCPDS card n. 85-2456 of the LiNbO_3 phase.

All the allowed reflections are observed in the spectra of the better crystallized film heated at 1073 K, thus indicating that no preferential orientation is obtained in the LiNbO_3 grains. In the films heated at lower temperature the peaks are weaker and wider.

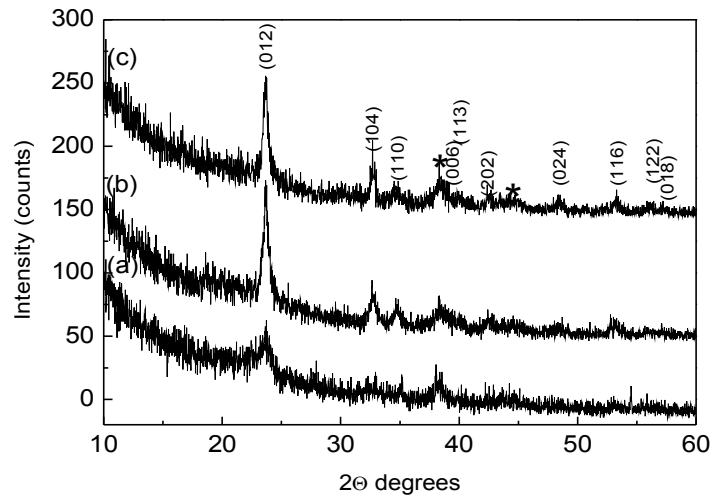


Fig. 5.7 GIXRD spectra of $\text{LiNbO}_3\cdot\text{SiO}_2$ films annealed at 873 K (a), 973 K (b) and 1073 K (c) at an incidence angle of 1.0° . The asterisks indicate the Ag reflections due to electrical contacts.

The average grains size estimated by the Scherrer equation results comparable with the values previously obtained, such as about 10 nm for the LiNbO_3 nanocrystals grown at 873 K and about 20 nm for the LiNbO_3 nanocrystals grown at 973 and 1073 K. It should be noted that in the 873–1073 K range LiNbO_3 is the only crystallizing phase in the films on the nano-scale. On the contrary, Bescher et al. [72] have obtained $\text{LiNbO}_3\cdot\text{SiO}_2$ thin films by sol-gel where the LiNbO_3 crystallization by XRD does not develop clearly until 973 K. The prepared thin films have a composition more rich in LiNbO_3 ($\text{LiNbO}_3/\text{SiO}_2=1$, molar ratio) than the present work, and were synthesized using the double alkoxide of lithium and niobium as molecular precursor of the LiNbO_3 phase. It was known that the double alkoxide, thanks to the Li–O–Nb chemical bonds already present in the precursor, would facilitate the growth of LiNbO_3 crystals when the amorphous gel is heated. In the present case, it is interesting to

underline that the use of cheap and inorganic precursors instead of the double alkoxides, give to the formation of LiNbO_3 nanocrystals at lower temperature respect to one reported by Bescher et al.[72].

2.2.3 dc current-voltage measurements

The electrical properties of thin films were investigated by current-voltage (I-V) measurements, employing a standard two probe technique, with a planar configuration. Measurements performed with different couples of electrical contacts, then on different part of the films, gave similar results, which indicates the homogeneity of the films from the electrical point of view. Measurements were also reproducible and stable in time, also when repeated after about six months.

In Figure 5.8 is reported the J – E (current density versus electric field) curve of the films heated at 673 K.

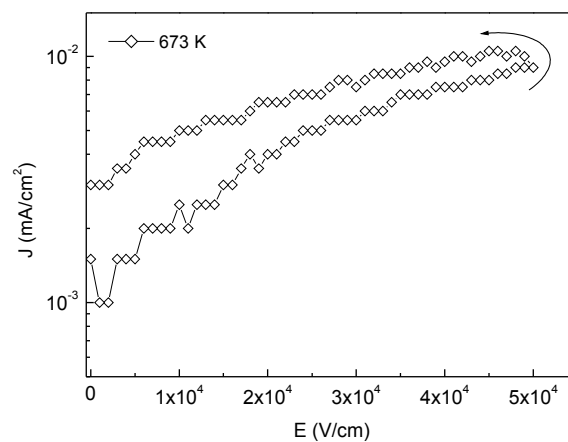


Fig. 5.8 J - E measurements of films annealed at 673 K during a voltage sweep from 0 to +500 V and +500 to 0 V. Arrows indicate the direction of the voltage sweep.

These films are insulating whatever the applied voltage showing a resistivity higher than $10^{12} \Omega \text{ cm}$, limited by the resolution of the experimental set up employed.

On the contrary, a different electrical behavior has been observed on films annealed at higher temperature. The J – E curves are reported in Figure 5.9.

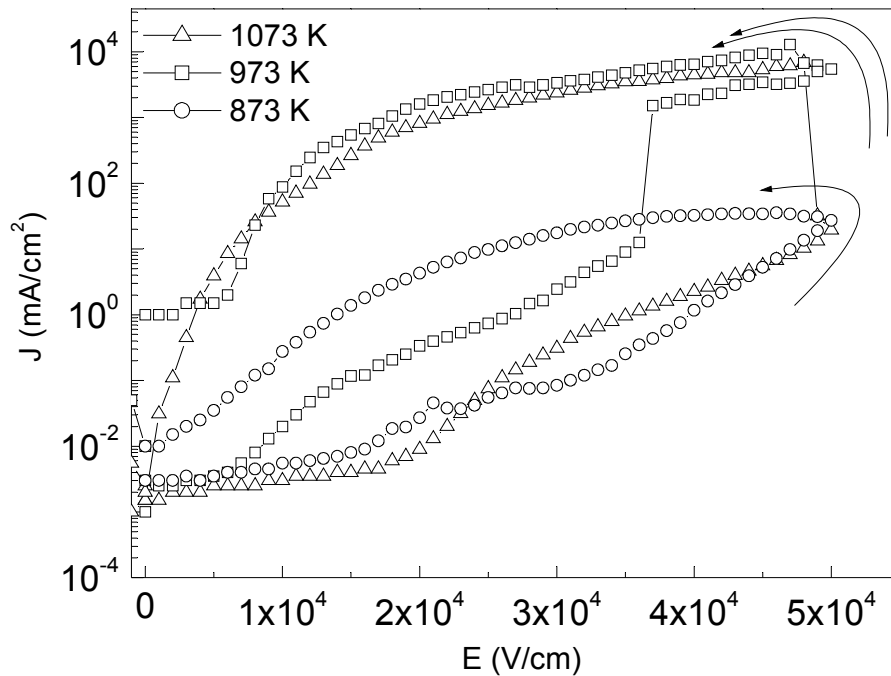


Fig. 5.9 J - E measurements of $\text{LiNbO}_3 \cdot \text{SiO}_2$ films annealed at 873 K (circles), 973 K (squares) and 1073 K (triangles) during a voltage sweep from 0 to +500 V and +500 to 0 V. Arrows indicate the direction of the voltage sweep.

From the electrical point of view, the presence of nanocrystals makes the films conducting, with an hysteretic behavior if subjected to a voltage sweep from 0 to +500 V and +500 to 0 V (Figure 5.9). Films annealed at 973 and 1073 K (LN

nanocrystals ~ 20 nm) present a similar and more pronounced behavior with respect to the film annealed at 873 K (LN nanocrystals ~ 10 nm), displaying a clear electrical bistability.

Linear type scale of the J – E measurement on a film annealed at 1073 K makes the bistability behavior more clear (Figure 5.10).

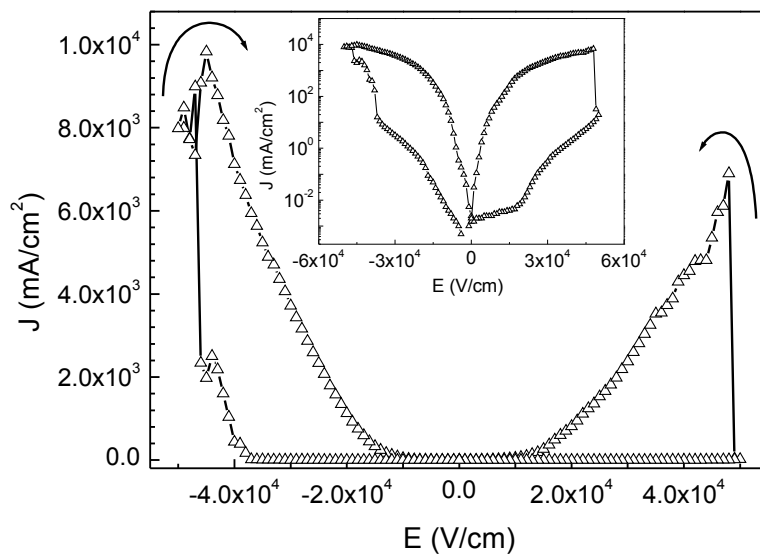


Fig. 5.10 J - E measurements of $\text{LiNbO}_3\text{:SiO}_2$ films annealed at 1073 K during a voltage sweep from 0 to +500 V and from +500 to -500 V and from -500 to 0 V. Arrows indicate the direction of the voltage sweep. In the inset the same data in semi-log plot are reported.

It can be observed that the ON state voltages (SET1) are in the range 400–500 V, and the bistability curves resulted roughly symmetrical with respect to the application of positive and negative voltages. The mean resistivity of the device in the so called ON state is about $10^4 \Omega \text{ cm}$ while, in the OFF state, an exponential voltage dependence is observed with a maximum resistivity value about $10^{10} \Omega$

cm. The current ratio between the ON and OFF states is at least 10^3 for both heat-treatment stages, and in any case higher than a reading process in a digital memory cell [58].

The bistability in these devices is reversible in nature and can be reversibly switched for many cycles. Since a planar configuration is used for the electrical measurements the role of the interface on the nature of the bistability can be ruled out. The time stability was also checked by probing the device at low- and high-conducting states for several hours.

The origin of the switching can be related to the increase of the average grains size of LiNbO_3 nanocrystals according to the AFM images and the diffraction spectra (Figures 5.5 – 5.7). Therefore, in the samples annealed at higher temperatures, the charge confinement in the nanoparticles can explain the electrical bistability. Under a suitable positive voltage, the LiNbO_3 nanoparticles with larger surface charge density form percolative networks. Such networks finally produce channels across the device resulting in a high conducting state. This interpretation is well supported by a recent paper of Pal and coworkers [56]. Actually, these authors have found that an electrostatic assembly of CdSe quantum dots exhibits a size-dependent electrical bistability by means of a mechanism of charge confinement in the nanoparticles.

In addition, the abrupt enhancement of the bistability range for $\text{LiNbO}_3\cdot\text{SiO}_2$ films annealed at 973 and 1073 K, indicates that the main contribution to the electrical bistability is that of the LiNbO_3 nanoparticles. Because the LiNbO_3 single crystal presents, at room temperature, a high dielectric constant [152], the charge accumulation on the grains surface is thus favored

above a critical grain size of nanometers tens. Indeed, it has been reported that in sol-gel glass-ceramics with LiNbO_3 crystallites, the number of dipoles associated with LiNbO_3 ferroelectric particles are hard to depolarize [153]. The overall picture of the electrical bistability suggests that these nanostructured films can be used for non-volatile memory.

CONCLUSIONS

This PhD thesis has highlighted that the sol-gel is a very useful tool to prepare functional nanocomposites based on $\text{Nb}_2\text{O}_5\cdot\text{SiO}_2$ and $\text{Li}_2\text{O}\cdot\text{Nb}_2\text{O}_5\cdot\text{SiO}_2$ systems. Innovative synthesis procedures were set, based on the control of the chemistry of Nb^{5+} ion in aqueous environment, that have allowed to obtain homogeneous chemical gels in both systems.

For the first time, a sol-gel route performed almost entirely in air at room temperature starting from one metal alkoxide ($\text{Si}(\text{OC}_2\text{H}_5)_4$) has allowed to obtain transparent $\text{LiNbO}_3\cdot\text{SiO}_2$ nanocomposite films.

Gel-derived materials, achieved by proper heat-treatments, have shown a very high dispersion of the active phase (Nb_2O_5 and LiNbO_3) in the matrix up to the molecular scale.

In the binary system, the Nb_2O_5 dispersion was strongly affected by its content: it was on the atomic scale up to 5 mol % whereas for higher concentration phase separated niobia-silica nanodomains were found. These structural differences mirror on the textural and surface acidic properties. Actually, materials with low Nb_2O_5 loading exhibited high surface area values, both Brønsted and Lewis acid sites of different strength, unlike those existing in pure oxides. Their catalytic activity were tested in the epoxidation of cyclooctene with hydrogen peroxide showing that both the acidic sites of moderate strength and the coordination of NbO_x species play key roles in the reaction mechanism. Thus, these

nanocomposites appear very interesting and promising heterogeneous catalysts, showing, for cyclooctene epoxidation, a comparable activity to that of similar literature systems but with the advantages of being prepared under much milder, inexpensive conditions and exhibiting a higher stability against leaching.

In the ternary system, high quality transparent thin films (about 400 nm thick) on Al_2O_3 substrates were obtained by dipping for the $20\text{LiNbO}_3\cdot 80\text{SiO}_2$ composition. Film annealed at different temperatures in the 873–1073 K range exhibited LiNbO_3 nanocrystals with the average size ranging from about 10 to 20 nm.

The presence of nanocrystals makes the films conducting. Actually, dc current-voltage measurements performed on planar devices based on the above films revealed a hysteretic behaviour and a clear electrical bistability, more evident when the size of nanocrystals reached the value of 20 nm. In addition, the ON/OFF current ratio in these devices was higher than a reading process in a digital memory cell and the bistability was reversible in nature and can be reversibly switched for many cycles.

Finally, understanding the transport mechanism granular systems with bistable properties is a hot topic at the forefront of the fundamental research. The present thesis clearly demonstrates that our approach can be extended to the study of nanocomposites in other systems, both for fundamental study and applications in microelectronics. Therefore, to additionally understand the role of the matrix and the grain size in such kind of samples, further measurements are desirable.

In conclusion, the new synthesis procedures by sol-gel we have optimized can be considered a very promising and versatile technique to obtain reproducible

nanocomposite thin films with very interesting bistability properties opening new perspectives in the field of memory systems.

BIBLIOGRAPHY

- [1] A. Rudiger, T. Schneller, A. Roelofs, S. Tiedke, T. Schmitz, R. Waser, *Appl. Phys. A* **2005**, 80, 1247.
- [2] C. Noguez, *Opt. Mater.* **2005**, 27, 1204.
- [3] M. Dofrenik, D. Lisjak, D. Makovec, *Mater. Sci. Forum* **2005**, 494, 129.
- [4] J.D. Lockwood, *Nanostructure Science and Technology, Surface Effects in Magnetic Nanoparticles*; Springer: New York, **2005**.
- [5] L.Q. Nguyen, C. Salim, H. Hinode, *Appl. Cat. A: Gen.* **2008**, 347, 94.
- [6] R. Thakar, Y. Chen, P.T. Snee, *Nano Lett.* **2007**, 7, 3429.
- [7] B. Mukherjee, S.K. Batabyal, A.J. Pal, *Adv. Mater.* **2007**, 19, 717.
- [8] C.J. Brinker, S.W. Scherer, *Sol–Gel science: the physics and chemistry of sol–gel processing*. Academic Press, New York, **1990**.
- [9] L.L. Hench, J.K. West, *Chem. Rev.* **1990**, 90, 33.
- [10] A. Fidalgo, M.E. Rosa, L.M. Ilharco, *Chem. Mater.* **2003**, 15, 2186.
- [11] K.O. Drake, D. Carta, L.J. Skipper, F.E. Sowrey, R.J. Newport, M.E. Smith, *Solid State NMR* **2005**, 27, 28.
- [12] B. Julia'n, C. Gervais, E. Cordoncillo, P. Escribano, F. Babonneau, C. Sanchez, *Chem. Mater.* **2003**, 15, 3026.
- [13] M.S.P. Francisco, Y. Gushikem, *J. Mater. Chem.* **2002**, 12, 2552.

- [14] M.S.P. Francisco, R. Landers, Y. Gushikem **2004**, J. Solid. State Chem. 177, 2432.
- [15] S.S. Rosatto, P.T. Sotomayor, L.T. Kubota, Y. Gushikem, Electrochim. Acta **2002**, 47, 4451.
- [16] A. Aronne, M. Turco, G. Bagnasco, P. Pernice, M. Di Serio, N.J. Clayden, E. Marenga, E. Fanelli, Chem. Mater. **2005**, 17, 2081.
- [17] C. J. Brinker, A. J. Hurd et al., "Sol-Gel Thin Film Formation", Chem. Proc., Adva. Mater., **1992**.
- [18] M.V. Landau, L. Vradman, A. Wolfson, P. Rao, M. Herskowitz, C. R. Chimie **2005**, 8, 679.
- [19] L. Dragone, P. Moggi, G. Predieri, R. Zanoni, Appl. Surf. Sci. **2002**, 187, 82.
- [20] M.S.P. Francisco, R. Landers, Y. Gushikem, J. Solid. State Chem. **2004**, 177, 2432.
- [21] F. Somma, P. Canton, G. Strukul, J. Catal. **2005**, 229, 490.
- [22] K. Tanabe, Catal. Today **2003**, 78, 65.
- [23] M. Ziolek, Catal. Today **2003**, 78, 47.
- [24] H. Shi, Z. Zhang, Y. Wang, J. Mol. Catal. A: Chem. **2005**, 238, 13.
- [25] D.V. Deubel, G. Frenking, P. Gisdakis, W.A. Herrmann, N. Roesch, J. Sundermeyer, Acc. Chem. Res. **2004**, 37, 645.
- [26] G. Strukul (Ed.), Catalytic Oxidations with Hydrogen Peroxide as Oxidant. Kluwer Academic, Dordrecht, The Netherlands, **1992**.
- [27] D.A. Ruddy, T. Don Tilley, Chem. Commun. **2007**, 3350.
- [28] N.A. Stephenson, A.T. Bell, J. Mol. Catal. A: Chem. **2007**, 275, 54.

- [29] M.G. Clerici, Appl. Catal. **1991**, 68, 249.
- [30] M. Jia, A. Seifert, W.R. Thiel, J. Catal. **2004**, 221, 319.
- [31] I. Nowak, B. Kilos, M. Ziolek, A. Lewandowska, Catal. Today **2003**, 78, 487.
- [32] I. Nowak, M. Ziolek, Microporous Mesoporous Mater. **2005**, 78, 281.
- [33] J.M.R. Gallo, I.S. Paulino, U. Schuchardt, Appl. Catal. A: Gen. **2004**, 266, 223.
- [34] J.M.R. Gallo, H.O. Pastore, U. Schuchardt, J. Catal. **2006**, 243, 57.
- [35] J.M.R. Gallo, H.O. Pastore, U. Schuchardt, J. Non-Cryst. Solids **2008**, 354, 1648.
- [36] J.E. Wachs, J.M. Jehng, G. Deo, H. Hu, N. Arora, Catal. Today **1996**, 28, 199.
- [37] F. Somma, G. Strukul, Catal. Lett. **2006**, 107, 73.
- [38] F. Somma, A. Puppinato, G. Strukul, Appl. Catal. A: Gen. **2006**, 309, 115.
- [39] D.C.M. Dutoit, M. Schneider, P. Fabrizioli, A. Baiker, Chem. Mater. **1996**, 8, 734.
- [40] V. Torma, H. Peterlik, U. Bauer, W. Rupp, N. Hu^osing, S. Bernstorff, M. Steinhart, G. Goerigk, U. Schubert, Chem. Mater. **2005**, 17, 3146.
- [41] C.A. Garcı'a-Franco, S. Srivatsan, D.J. Lohse, P. Brant, Macromolecules **2001**, 34, 3115.
- [42] E. Bonanomi, P. Sandku^hler, J. Sefcik, M. Morari, M. Morbidelli, Ind. Eng. Chem. Res. **2004**, 43, 4740.
- [43] B.J. Clapsaddle, D.W. Sprehn, A.E. Gash, J.H. Satcher Jr, R.L. Simpson, J. Non-Cryst. Solids **2004**, 350, 173.

- [44] E.R. Camargo, M. Kakihana, Chem. Mater. **2001**, 13, 1905.
- [45] F. Lenzmann, V. Shklover, K. Brooks, M. Graetzel, J. Sol–Gel Sci. Technol. **2000**, 19, 175.
- [46] T. Ouisse, O. Stephan, Org. Electron. **2004**, 5, 251.
- [47] H.S. Majumdar, A. Bolognesi, A.J. Pal, Synth. Met. **2006**, 156, 828.
- [48] S.L. Lim, Q. Ling, E.Y.H. Teo, C.X. Zhu, D.S.H. Chan, E.T. Kang, K.G. Neoh, Chem. Mater. **2007**, 19, 5148.
- [49] T. Oyamada, H. Tanaka, K. Matsushige, H. Sasabe, C. Adachi, Appl. Phys. Lett. **2003**, 83, 1252.
- [50] C.K. Kim, W.J. Joo, E.S. Song, H.J. Kim, J. Kim, C. Park, H.L. Lee, C. Kim, Synth. Met. **2007**, 157, 640.
- [51] S.K. Majee, A. Bandyopadhyay, A.J. Pal, Chem. Phys. Lett. **2004**, 399, 284.
- [52] J. Hu, Y. Li, Z. Ji, G. Jiang, L. Yang, W. Hu, H. Gao, L. Jiang, Y. Wen, Y. Song, D. Zhu J. Mater. Chem. **2007**, 17, 3530.
- [53] K. Szot, W. Speier, G. Bihlmayer, R. Waser, Nat. Mater. **2006**, 5, 312.
- [54] J. Ouyang, C.W. Chu, C.R. Szmanda, L. Ma, Y. Yang, Nat. Mater. **2004**, 3, 918.
- [55] S. Sahu, S.K. Majee, A.J. Pal, Appl. Phys. Lett. **2007**, 91, 143108/1.
- [56] B.C. Das, S.K. Batabyal, A.J. Pal, Adv. Mater. **2007**, 19, 4172.
- [57] B. Pradhan, S.K. Majee, S.K. Batabyal, A.J. Pal, J. Nanosci. Nanotechnol. **2007**, 7, 4534.
- [58] F. Li, T.W. Kim, W. Dong, Y.H. Kim, Appl. Phys. Lett. **2008**, 92(1), 011906.
- [59] C.W. Chu, J. Ouyang, J.H. Tseng, Y. Yang, Adv. Mater. **2005**, 17, 1440.

- [60] L.E. Hueso, I. Bergenti, A. Riminucci, Y. Zhan, V. Dediu, *Adv. Mater.* **2007**, 19, 2639.
- [61] Lerner, P.; Legras, C.; Dumas, J. P. *J. Cryst. Growth* **1968**, 3-4, 231.
- [62] R. Fernández-Ruiz and V. Bermúdez *Chem. Mater.* **2004**, 16, 3593
- [63] J.K. Krebs, U. Happek, *Appl. Phys. Lett.* **2005**, 87, 251910
- [64] Y. Kondo, T. Fukuda, Y. Yamashita, K. Yokoyama, K. Arita, M. Watanabe, Y. Furukawa, K. Kitamura, H. Nakajima, *Jpn. J. Appl. Phys., Part 1*, **2000**, 39, 1477.
- [65] S. Hirano, K. Kato, *J. Non-Cryst. Solids* **1988**, 100, 538.
- [66] S. Hirano, T. Yogo, W. Sakamoto, Y. Takeichi, S. Ono *J. Eur. Ceram. Soc.* **2004**, 24, 435 and references therein.
- [67] Z. Cheng, K. Ozawa, A. Miyazaki, H. Kimura *J. Am. Ceram. Soc.* **2005**, 88, 1023.
- [68] H.C. Zeng and S.K. Tung *Chem. Mater.* **1996**, 8, 2667.
- [69] Liu, M.; Xue, D.; Li, K. *J. All. Comp.* **2008**, 449, 28.
- [70] A.V. Chadwick, M.J. Pooley, S.L.P. Savin, *Phys. Stat. Sol. C* **2005**, 2, 302.
- [71] A.V. Chadwick, S.L.P. Savin, L.A. O'Dell, M.E. Smith, *J. Phys: Condens. Matter* **2006**, 18, L163.
- [72] E. Bescher, Y. Xu, J.D. Mackenzie, *J. Appl. Phys.* **2001**, 89, 6341.
- [73] M.P.F. Graça, M.G. Ferreira da Silva, M.A. Valente, *J. Non-Cryst. Solids* **2005**, 351, 2951.
- [74] M.P.F. Graça, M.G. Ferreira da Silva, A.S.B. Sombra, M.A. Valente, *J. Non Cryst. Solids* **2006**, 352, 1501.
- [75] M.P.F. Graça, M.G. Ferreira da Silva, M.A. Valente, *J. Sol-GelSci. Technol*

2007, 42, 1.

[76] C.J. Brinker, B.C. Bunker et al., Structure of Sol-Gel Derived Inorganic Polymers: Silicates and Borates, Am. Chem. Soc., part II **1988**.

[77] R.W. Jones, Fundamental Principles of Sol-Gel Technology **1989**.

[78] L.C. Klein, G.J. Garvey, Effect of Water on Acid- and Base-Catalyzed Hydrolysis of Tetraethylorthosilicate (TEOS), Mater. Res. Soc. Sym. Proc. **1984**, 32.

[79] K.D. Keefer, The Effect of Hydrolysis Conditions on the Structure and Growth of Silicate Polymers, Mater. Res. Soc. Sym. Proc., **1984**, 32.

[80] C.B. Hurd, Chem. Rev. **1938**, 22, 403.

[81] L.D. Landau, B.G. Levich, Acta Physiochim., U.R.S.S. **1942**, 17, 42.

[82] I. Strawbridge, P.F. Iames, J. Non-Cryst. Solids **1986**, 82, 366.

[83] C.J. Brinker, A.J. Hurd, K.J. Ward, Ultrastructure Processing of Advanced Ceramics, eds. J.D. Mackenzie and D.R. Ulrich, Wiley, New York **1988**, 233.

[84] O. Stern Z. Elektrochem. **1954**, 508.

[85] H. Schroder, Physics of Thin Films, Academic Press, New York – London, **1969**, 5, 87.

[86] H. Dislich, Angew. Chem. Int. Ed. **1971**, 63, 63.

[87] S. Kallmann, Niobium and Tantalum in Treatise on Analytical Chemistry, I.M. Kolthoff, P. J. Elving, Eds., part 2, Vol.6, John Wiley & Sons: Easton, **1964**.

[88] G. Telep, D.F. Boltz, Anal. Chem. **1951**, 24, 163.

[89] F.G. Palilla, N. Adler, C.F. Hiskey, Anal. Chem. **1953**, 25, 926.

[90] APHA AWWA WEF, Standard Methods for the Examination of Water and Wastewater, 21th ed.; Washington, **2005**.

- [91] F.J. Rouquerol, K. Sing, Adsorption by Powders and Porous Solids Principles, Methodology and Applications, Elsevier B.V. **1999**.
- [92] I. Horcas, R. Fernandez, J.M. Gomez-Rodriguez, J. Colchero, J. Gomez-Herrero, A.M. Baro, Rev. Sci. Instrum. **2007**, 78, 0137051.
- [93] J. Livage, M. Henry, C. Sanchez, Prog. Solid. State Chem. **1988**, 18, 259.
- [94] A. Zalkin, D.E. Sands, Acta Cryst. **1958**, 11, 615.
- [95] J.E.D. Davies, D.A. Long, J. Chem. Soc (A) **1968**, 2560.
- [96] D. Brown In: Blair JC, Emele'us HJ, Nyholm R, Trotman-Dickenson AF (eds) Comprehensive inorganic chemistry, vol. 3; Pergamon Press Ltd., Oxford, **1973**, 587.
- [97] B. Julia'n, C. Gervais, M.N. Rager, J. Maquet, E. Cordoncillo, P. Escribano, F. Babonneau, C. Sanchez, Chem. Mater. **2004**, 16, 521.
- [98] H. Hamadan, M.N.M. Muhid, S. Endud, E. Listiorini, Z. Ramli, J. Non-Cryst. Solids **1997**, 211, 126.
- [99] A. Le Blail, J. Non-Cryst. Solids **1995**, 183, 39.
- [100] A. Aronne, V.N. Sigaev, P. Pernice, E. Fanelli, L.Z. Usmanova, J. Non-Cryst. Solids **2004**, 337, 121.
- [101] I. Novak, M. Ziolek, Chem. Rev. **1999**, 99, 3603.
- [102] V.S. Braga, J.A. Dias, S.C.L. Dias, J.L. de Macedo, Chem. Mater. **2005**, 17, 690.
- [103] B. Humbert, A. Burneau, J.P. Gallas, J.C. Lavalley, J. Non-Cryst. Solids **1992**, 143, 75.
- [104] A.E. Geissberger, F.L. Galeener, Phys. Rev. B **1983**, 28, 3266.
- [105] C.J. Brinker, D.R. Tallant, E.P. Roth, C.S. Ashley, J. Non-Cryst. Solids

1986, 82, 117.

- [106] E.I. Kamistos, A.P. Patsis, G. Kordas, *Phys. Rev. B* **1993**, 48, 12499.
- [107] N. Chiodini, F. Meinardi, F. Morazzoni, A. Paleari, R. Scotti, G. Spinolo, *Sol. State Commun.* 1 **1999**, 09, 145.
- [108] P. McMillan, B. Piriou, *Bull. Mine´ral* **1983**, 106, 57.
- [109] C. Kinowski, M. Bouazaoui, R. Bechara, L.L. Hench, J.M. Nedelec, S. Turrell, *J. Non-Cryst. Solids* **2001**, 291, 143.
- [110] I.E. Wachs, *Catal. Today* **1996**, 27, 437.
- [111] A. Aronne, V.N. Sigaev, B. Champagnon, E. Fanelli, V. Califano, L.Z. Usmanova, P. Pernice, *J. Non-Cryst. Solids* **2005**, 351, 3610.
- [112] J.M. Jehng, I.E. Wachs, *Chem. Mater.* **1991**, 3, 100.
- [113] B. Orel, M. Macˇek, J. Grdadolnik, A. Meden, *J. Sol. State Electrochem.* **1998**, 2, 221.
- [114] A.A. McConnell, J.S. Anderson, C.N.R. Rao, *Spectrochim. Acta* **1976**, 32A, 1067.
- [115] L.A. Farrow, E.M. Vogel, *J. Non-Cryst. Solids* **1992**, 143, 59.
- [116] P. Innocenzi, *J. Non-Cryst. Solids* **2003**, 316, 309.
- [117] R.M. Almeida, T.A. Guiton, C.G. Pantano, *J. Non-Cryst. Solids* **1990**, 121, 193.
- [118] J. Gallardo, A. Dura´n, D. Di Martino, R.M. Almeida, *J. Non-Cryst. Solids* **2002**, 298, 219.
- [119] M. Cerruti, G. Magnacca, V. Bolis, C. Morterra, *J. Mater. Chem.* **2003**, 13, 1279.
- [120] N.J. Clayden, S. Esposito, P. Pernice, A. Aronne, *J. Mater. Chem.* **2002**, 12,

3746.

[121] I.N. Martyanov, S. Uma, S. Rodrigues, K.J. Klabunde, *Langmuir* **2005**, 21, 2273.

[122] E. El-Malki, D. Werst, P.E. Doan, W.M.H. Sachtler, *J. Phys. Chem. B* **2000**, 104, 5924.

[123] A. Fielicke, G. Meijer, G.V. Helden, *J. Am. Chem. Soc.* **2003**, 125, 3659.

[124] A. Aronne, S. Esposito, C. Ferone, M. Pansini, P. Pernice, *J. Mater. Chem.* **2002**, 12, 3039.

[125] IUPAC Recommendations, *Pure Appl. Chem.* **1985**, 57, 603.

[126] F.J. Rouquerol, K. Sing, *Adsorption by Powders and Porous Solids Principles, Methodology and Applications*, Elsevier B.V., **1999**.

[127] S. Damyanova, L. Dimitrov, L. Petrov, P. Grange, *Appl. Surf. Sci.* **2003**, 214, 68.

[128] K. Yamashita, M. Hirano, K. Okumura, M. Niwa, *Catal. Today* **2006**, 118, 385.

[129] K.V.R. Chary, C.P. Kumar, A. Murali, A. Tripathi, A. Clearfield, *J. Mol. Catal. A: Chem.* **2004**, 216, 139.

[130] X. Gao, I.E. Wachs, M.S. Wong, J.Y. Ying, *J. Catal.* **2001**, 203, 18.

[131] L.J. Burcham, J. Datka, I.E. Wachs, *J. Phys. Chem. B* **1999**, 103, 6015.

[132] G. Busca, G. Ramis, V. Lorenzelli, *J. Mol. Catal.* **1989**, 50, 231.

[133] G. Ramis, G. Busca, V. Lorenzelli, *J. Chem. Soc. Faraday Trans.* **1994**, 90, 1293.

[134] J.C. Lavalley, C. Gain, *Acad. Sci. Paris, Ser. C* **1979**, 288, 177.

[135] F. Koubowetz, J. Latzel, H. Noller, *J. Colloid Interf. Sci.* **1980**, 74, 322.

- [136] C. Binet, A. Jadi, J.C. Lavalley, *J. Chem. Phys.* **1992**, 89, 31.
- [137] P. Venakateswarlu, *J. Chem. Phys.* **1951**, 9, 293.
- [138] P. Venakateswarlu, *J. Chem. Phys.* **1952**, 20, 923.
- [139] J. Reedijk, A.P. Zuur, W.L. Groeneveld, *Recueil Trav. Chim.* **1967**, 86, 1127.
- [140] J.F. Bertran, B. La Serna, K. Doerffel, K. Dathe, G. Kabish, *J. Mol. Struct.* **1982**, 95, 1.
- [141] M. Trombetta, G. Busca, S. Rossigni, V. Piccoli, U. Corsaro, A. Guercio, R. Catani, R.J. Willey, *J. Catal.* **1998**, 179, 581.
- [142] T. Armaroli, G. Busca, C. Carlini, M. Giuttari, A.M. Raspolli Galletti, G. Sbrana, *J. Mol. Catal. A: Chem.* **2000**, 233, 151.
- [143] G. Busca, *Catal. Today* **1998**, 41, 191.
- [144] H. Knozinger, H.D. Muller, *J. Chem. Soc., Faraday Trans.* **1976**, 72, 2703.
- [145] G. Busca, G. Centi, F. Trifiro', *J. Am. Chem. Soc.* **1985**, 107, 7757.
- [146] M.C.A. van Vliet, D. Mandelli, I.W.C.E. Arends, U. Schuchardt, R.A. Sheldon, *Green Chem.* **2001**, 3, 243.
- [147] R. Rinaldi, F.Y. Fujiwara, U. Schuchardt, *J. Catal.* **2007**, 245, 456.
- [148] R. Rinaldi, F.Y. Fujiwara, W. Hoelderich, U. Schuchardt, *J. Catal.* **2006**, 244, 92.
- [149] A.Z. Simoes, A.H.M. Gonzales, A. Ries, M.A. Zaghete, B.D. Stojanovic, J.A. Varela, *Materials Characterization* **2003**, 50, 239.
- [150] K.L. Westra, A.W. Mitchell, D.J. Thomson, *J. Appl. Phys.* **1993**, 74, 3608.
- [151] K. Oikawa, H. Kim, N. Watanabe, M. Shigeno, Y. Shirakawabe, K. Yasuda, *Ultramicroscopy* **2007**, 107, 1061.

[152] M.M. Abouellell, F.J. Leonberger, J. Am. Ceram. Soc. **1989**, 72, 1311.

[153] M.P.F. Grac,a, M.A. Valente, M.G. Ferreira da Silva, J. Non-Cryst. Solids
2003, 325, 267.

List of Figures

- Figure 1.1** Sol-gel process 27
- Figure 1.2** Gel structure: **a** crosslinked linear chains; **b** branched clusters 32
- Figure 1.3** Stages of the dip coating process: a) dipping of the substrate into the coating solution; b) wet layer formation by withdrawing the substrate; c) gelation of the layer by solvent evaporation 34
- Figure 1.4** Gelation process during dip-coating process, obtained by evaporation of the solvent and subsequent destabilization of the sol 35
- Figure 2.1** Flow-chart of the gels synthesis procedure showing the molar ratios employed 39
- Figure 2.2** Sample $(\text{Nb}_2\text{O}_5)_{20} \cdot (\text{SiO}_2)_{80}$ (20Nb): **a** wet gel; **b** dried gels 40
- Figure 2.3** Dried SiO_2 gel 40
- Figure 2.4.** Calibration line absorbance versus niobium concentration 42
- Figure 2.5** Calibration line absorbance versus soluble silica concentration 43
- Figure 2.6** Carlo Erba-Fisher apparatus model for surface area determination 46
- Figure 2.7** TPD flow apparatus model 47
- Figure 3.1** Flow-chart of the bulk gels synthesis procedure showing the molar ratios employed 51
- Figure 3.2** Flow-chart of the flakes synthesis procedure showing the molar ratios employed 53
- Figure 3.3** Flow-chart of the films synthesis procedure showing the molar ratios employed 54

- Figure 3.4** Dip-coater for films deposition 55
- Figure 3.5** Electrical silver contacts 58
- Figure 3.6** Probe station 59
- Figure 4.1** Niobium absorbance spectrum 64
- Figure 4.2** DTA (solid line)-TG (dotted line) curves of the dried gels recorded at 10 K min⁻¹ 66
- Figure 4.3** XRD patterns of the heat-treated gel samples. T and H stand for T-Nb₂O₅ and H-Nb₂O₅ phases, respectively 68
- Figure 4.4** Raman spectra of the studied gels heated at different temperature. (a): (Nb₂O₅)₂₀·(SiO₂)₈₀ (*20Nb*); (b): (Nb₂O₅)₁₀·(SiO₂)₉₀ (*10Nb*); (c): (Nb₂O₅)₅·(SiO₂)₉₅ (*5Nb*); (d): (Nb₂O₅)_{2.5}·(SiO₂)_{97.5} (*2.5Nb*); (e): SiO₂ 72
- Figure 4.5** FTIR spectra of the studied gels heated at different temperature. (a): (Nb₂O₅)₂₀·(SiO₂)₈₀ (*20Nb*); (b): (Nb₂O₅)₁₀·(SiO₂)₉₀ (*10Nb*); (c): (Nb₂O₅)₅·(SiO₂)₉₅ (*5Nb*); (d): (Nb₂O₅)_{2.5}·(SiO₂)_{97.5} (*2.5Nb*); (e): SiO₂ 78
- Figure 4.6** N₂ adsorption-desorption isotherms of SiO₂ and of the investigated catalysts. Full symbols: adsorption; empty symbols: desorption 84
- Figure 4.7** α-plot of SiO₂ and of investigated catalysts 85
- Fig. 4.8** Pore size distribution of the investigated catalysts 86
- Figure 4.9.** NH₃ TPD spectra of SiO₂, Nb₂O₅ and of the investigated catalysts 87
- Figure 4.10** FTIR spectra of pure *2.5Nb* pressed disk after outgassing at 773 K (a) and following contact with acetonitrile vapours 5 Torr (b) and successive outgassing at room temperature (c), 373 K (d), 473 K (e) and 573 K (f) for 10 min. The gas-phase spectra have been subtracted 91
- Figure 4.11** FTIR spectra of pure *5Nb* pressed disk after outgassing at 773 K (a)

and following contact with acetonitrile vapours 5 Torr (b) and successive outgassing at room temperature (c), 373 K (d), 473 K (e) and 573 K (f) for 10 min. The gas-phase spectra have been subtracted 92

Figure 4.12 FTIR spectra of pure *10Nb* pressed disk after outgassing at 773 K (a) and following contact with acetonitrile vapours 5 Torr (b) and successive outgassing at room temperature (c), 373 K (d), 473 K (e) and 573 K (f) for 10 min. The gas-phase spectra have been subtracted 92

Figure 4.13 FTIR spectra of pure *2.5Nb* (a), *5Nb* (b), *10Nb* (c) pressed disks after outgassing at 773 K and following contact with acetonitrile vapours (5 Torr). The gas-phase spectra have been subtracted 95

Figure 4.14 Conversion versus time plots of epoxidation of cyclooctene with hydrogen peroxide catalyzed by differently loaded $\text{Nb}_2\text{O}_5\cdot\text{SiO}_2$ catalysts 96

Figure 5.1 DTA (solid line)-TG (dotted line) curves of bulk gels recorded in air at 10 K min^{-1} 104

Figure 5.2 XRD patterns of the bulk gels heat 4 hours at different temperatures.

* LiNbO_3 , + $\text{T-Nb}_2\text{O}_5$, × LiNb_3O_8 , ° crystobalite 106

Figure 5.3 XRD patterns of the flakes gels heat 4 hours at different temperatures.

* LiNbO_3 , × LiNb_3O_8 , # sample holder 108

Figure 5.4 XRD pattern of the heat-treated *TF-10LN* film deposited on Si-SiO_2 substrate. * LiNbO_3 , + substrate 111

Figure 5.5 AFM images of a $\text{LiNbO}_3\text{-SiO}_2$ films: **a** A film annealed at 600 K. In the inset is enlarged the marked area. Scanned area and z-scale are respectively $3.5 \times 3.5\ \mu\text{m}^2$ and 10 nm for the main image while they are $700 \times 700\ \text{nm}^2$ and 4.0 nm for the inset. **b** A film annealed at 873 K. In the inset is enlarged the marked

area. Scanned area and z-scale are respectively $10 \times 10 \mu\text{m}^2$ and 20 nm for the main image while they are $500 \times 500 \text{ nm}^2$ and 4.0 nm for the inset. **c** Films annealed at 873 K (left side), 973 K (middle) and 1073 K (right side). Scanned area and is $1 \times 1 \mu\text{m}^2$ in the top sequence, $500 \times 500 \text{ nm}$ in the bottom one. Z-scale is 4 nm 113

Figure 5.6 XRD spectra of the heat-treated *TF-10LN* sample deposited on Al_2O_3 substrate. The straight line is a guide for eyes 114

Figure 5.7 GIXRD spectra of $\text{LiNbO}_3\cdot\text{SiO}_2$ films annealed at 873 K (a), 973 K (b) and 1073 K (c) at an incidence angle of 1.0° . The asterisks indicate the Ag reflections due to electrical contacts 117

Figure 5.8 J - E measurements of films annealed at 673 K during a voltage sweep from 0 to +500 V and +500 to 0 V. Arrows indicate the direction of the voltage sweep 118

Figure 5.9 J - E measurements of $\text{LiNbO}_3\cdot\text{SiO}_2$ films annealed at 873 K (circles), 973 K (squares) and 1073 K (triangles) during a voltage sweep from 0 to +500 V and +500 to 0 V. Arrows indicate the direction of the voltage sweep. In the inset, the electrical contacts geometry is reported 119

Figure 5.10 J - E measurements of $\text{LiNbO}_3\cdot\text{SiO}_2$ films annealed at 1073 K during a voltage sweep from 0 to +500 V and from +500 to -500 V and from -500 to 0 V. Arrows indicate the direction of the voltage sweep. In the inset the same data in semi-log plot are reported 120

List of Tables

Table 3.1 Gels composition mol% 51

Table 4.1 Chemical analysis of niobium and silicon 65

Table 4.2 Surface area and pore volume of Nb₂O₅·SiO₂ catalysts 85

Table 4.3 Temperature peaks, adsorbed NH₃ amounts and acid site concentration from TPD measurements 88

Table 4.4 Oxidation of cyclooctene with hydrogen peroxide catalyzed by different niobium containing catalysts 97

Table 4.5 Effect of recycling in the epoxidation of cyclooctene with hydrogen peroxide catalyzed by Nb₂O₅·SiO₂ catalysts 101

Table 5.1 The structural parameters extracted from XRD spectra 115

List of Abbreviations

Abs Absorbance

AFM Atomic Force Microscopy

BET Brunauer-Emmett-Teller

BJH Barrett-Joiner-Halenda

B-5LN $5\text{Li}_2\text{O}\cdot 5\text{Nb}_2\text{O}_5\cdot 90\text{SiO}_2$ (mol%)

B-10LN Bulk- $10\text{Li}_2\text{O}\cdot 10\text{Nb}_2\text{O}_5\cdot 80\text{SiO}_2$ (mol%)

CCD Charge-Coupled Detector

DTA Differential Thermal Analysis

DTGS Deuterated Triglycine Sulphate

EtOH Ethanol

F-10LN Flake- $10\text{Li}_2\text{O}\cdot 10\text{Nb}_2\text{O}_5\cdot 80\text{SiO}_2$ (mol%)

F-15LN Flake- $15\text{Li}_2\text{O}\cdot 15\text{Nb}_2\text{O}_5\cdot 70\text{SiO}_2$ (mol%)

FID Flame Ionization Detector

FTIR Fourier Transform Infrared Spectroscopy

GIXRD Glancing Incidence X-Ray Diffraction

HRTEM High-Resolution Transmission Electron Microscopy

IR Infrared

IUPAC International Union of Pure and Applied Chemistry

I-V Current-Voltage

5LN $5\text{Li}_2\text{O}\cdot 5\text{Nb}_2\text{O}_5\cdot 90\text{SiO}_2$ (molar composition)

10LN $10\text{Li}_2\text{O}\cdot 10\text{Nb}_2\text{O}_5\cdot 80\text{SiO}_2$ (molar composition)

15LN $15\text{Li}_2\text{O}\cdot 15\text{Nb}_2\text{O}_5\cdot 70\text{SiO}_2$ (mol%)

MeOH Methanol

2.5Nb $2.5\text{Nb}_2\text{O}_5\cdot 97.5\text{SiO}_2$ (mol%)

5Nb $5\text{Nb}_2\text{O}_5\cdot 95\text{SiO}_2$ (mol%)

10Nb $10\text{Nb}_2\text{O}_5\cdot 90\text{SiO}_2$ (mol%)

20Nb $20\text{Nb}_2\text{O}_5\cdot 80\text{SiO}_2$ (mol%)

NMR Nuclear Magnetic Resonance

OR alkoxide group

r.t. room temperature

SLN Stoichiometric Lithium Niobate

TCD Thermal Conductivity Detector

TEOS Tetraethoxysilane

TF-10LN Thin Film- $10\text{Li}_2\text{O}\cdot 10\text{Nb}_2\text{O}_5\cdot 80\text{SiO}_2$ (mol%)

TGA Thermogravimetric Analysis

TPD Temperature Programmed Desorption

TS-1 Titanium Silicalite

XPS X-ray Photoelectron Spectroscopy

XRD X-Ray Diffraction

